ROYAL SOCIETY OF CHEMISTRY

Chem Soc Rev

REVIEW ARTICLE

View Article Online
View Journal

Check for updates

Cite this: DOI: 10.1039/d5cs00823a

The importance of nano–bio interfacial design in the sensing performance of nanoparticle-based affinity biosensors

Xueqian Chen,[a] Xuejie Li,[a] Richard D. Tilley[bc] and J. Justin Gooding *[b]

Biosensors with good sensing performances with regards to high sensitivity, specificity, shorter response time, the ability to be multiplexed, excellent stability and reproducibility, are always in high demand. As modern biosensors are often fabricated using bioreceptors immobilized on nanoparticles to achieve efficient signal transduction or easier handling, the nanoparticle–bioreceptor (nano–bio) interface has a significant impact on the final sensing metrics. However, the role of nano–bio interfaces in sensing performance could be better understood, to facilitate the rational design of high performing nano–bio based devices. Herein, we aim to provide some basic rules and considerations to optimize nano–bio interfaces to achieve better detection performance when fabricating biosensors. The impact of the nano–bio interfaces on sensing characteristics is discussed from the perspective of bioreceptor–analyte interaction. Four interfacial parameters are included in this review: (1) the conformation of bioreceptors, (2) the coverage of the bioreceptors, (3) composition of mixed ligands, such as bioreceptors and other functional molecules and (4) spatial distribution of bioreceptors on nanoparticle surfaces. Methods to tailor these four interfacial factors are systematically investigated. In parallel, how these tailored nano–bio factors improve the sensing performances is emphasized with corresponding biosensor examples. The analytical methods for characterization of nano–bio interfaces are summarized, particularly at the single particle level. Additionally, the integration of artificial intelligence (AI) with nano–bio interfaces is discussed, highlighting how AI can improve nano–bio interfacial design. Finally, future perspectives on the role of nano–bio interfacial design in enhancing sensing capabilities are presented. This review aims to elucidate the relationship between nano–bio interfacial factors and sensing performances, as well as strategies for achieving precisely controlled nano–bio interfaces, which facilitates the rational design of high-performance biosensors.

Received 4th March 2026

DOI: 10.1039/d5cs00823a

rsc.li/chem-soc-rev

---

[a] *Pingyuan Laboratory, College of Chemistry, Zhengzhou University, Zhengzhou 450000, China. E-mail: chenxq@zzu.edu.cn, lixuejie@gs.zzu.edu.cn*

[b] *School of Chemistry, Australian Centre for NanoMedicine, The University of New South Wales, Sydney, New South Wales 2052, Australia. E-mail: R.tilley@unsw.edu.au, Justin.gooding@unsw.edu.au*

[c] *Mark Wainwright Analytical Centre, The University of New South Wales, Sydney, New South Wales 2052, Australia*

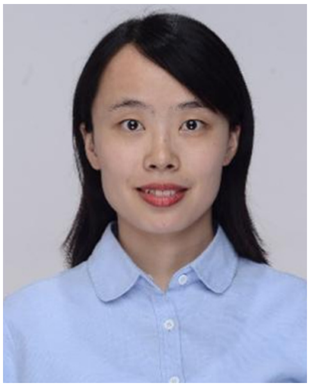

Xueqian Chen

Xueqian Chen received her PhD degree from the School of Chemistry, University of New South Wales. Currently, she is a lecturer at the Pingyuan Laboratory, College of Chemistry, Zhengzhou University. Her research interests include the synthesis of functional nanomaterials, investigation of their surface and interfacial properties, and the development of nanomaterial-based optical probes for biosensing and bioimaging.

Xuejie Li

Xuejie Li received her bachelor's degree from the College of Chemical and Materials Engineering, Fuyang Normal University. She is currently pursuing her master's degree at the College of Chemistry, Zhengzhou University. Her research focuses on the synthesis of nanomaterials and their applications in the degradation of microplastics.

1. Introduction

Nanoparticles have become ubiquitous in modern biosensors as nanoparticles can act as both a carrier for bioreporters and as a transducer to produce and enhance signals over the background and improve sensitivity of detection.[1,2] In addition, each nanoparticle can be thought of as an independent sensing unit, which contributes to the measurement of many events in parallel. Recording the information from many individual nanoparticles in parallel creates the potential for both multiplex and high-throughput detection.[3,4] Furthermore, magnetic nanoparticles (MNPs) can reduce response times due to magnetic forces facilitating mass transport.[5,6] In most nanoparticle-based biosensors, bioreceptors are immobilized on the surface of nanoparticles.[7] Consequently, a number of surface-related factors are involved during the process of fabricating biosensors, including the surface chemistry of nanoparticles, the self-assembled monolayer that the nanoparticle is modified with, the biofunctionalization of nanoparticles with bioreceptor molecules, and the display of the bioreceptors on nanoparticles.[8–11] These surface-related factors can significantly impact the bioreceptor–analyte interaction and thereby the sensing performances.

The nano–bio interface is the central component of a biosensor as it is directly involved in bioreceptor–analyte interaction, bridging the process of molecular biorecognition and signalization during biosensing (Fig. 1). The nano–bio interface determines the binding properties of nano–bio conjugates towards analytes and other biomolecules in the sample matrix. There are already some fabulous reviews about self-assembled monolayers of organic ligands on nanoparticles and biofunctionalization of nanoparticles.[12–15] However, despite the important role of nano–bio interfaces in bioreceptor–analyte interaction and downstream analytical performance, there are limited reviews related to how the nano–bio interfaces affect the sensing performance of biosensors. If the nano–bio interface can be tailored and controlled precisely, we can understand the effect of nano–bio interfaces on bioreceptor–analyte interaction and how the bioreceptor–analyte interaction correlates with detection performance. This knowledge is of significance for the rational design of biosensors. Therefore, in this review, we first emphasize the important role of nano–bio interfaces in nanoparticle-based biosensors. Then, we discuss how the nanoparticle surface influences the bioreceptor–analyte interaction with particular emphasis on surface-based DNA biosensors as a case study. More deeply, the mechanisms behind the effect of nano–bio interfaces on interaction between bioreceptors and analytes are explored. Four interfacial parameters, namely conformation, coverage, spatial distribution of bioreceptors, and compositions of mixed ligands on nanoparticles, are introduced separately. Approaches to tailor these interfacial parameters and how these interfacial parameters improve the sensing capabilities of biosensors are demonstrated with corresponding examples. The sensing performances encompass sensitivity, limit of detection (LOD), specificity, selectivity, response time, multiplex detection, stability, and reproducibility. Following this, analytical approaches for characterizing nano–bio interfaces are outlined, with an emphasis on single-particle measurement. Considering the rapid progress of artificial intelligence (AI)-assisted biosensors, the integration of AI with nano–bio interfaces is explored. Finally, we conclude with perspectives on remaining challenges and future trends in this field.

2. Importance of the nano–bio interfaces

2.1. Effect of nanoparticle surfaces on bioreceptor–analyte interaction

Bioreceptors, generally including enzymes, antibodies, DNA, aptamers, peptides and lectin, are normally immobilized on nanoparticles to give nanoparticles specificity for target analytes (Fig. 1).[16–18] The sizes of nanoparticles adopted are usually smaller than 100 nm, comparable with the size of

Richard D. Tilley

Professor Richard Tilley is the Director of the Electron Microscope Unit at UNSW. His research is focused on the solution synthesis of nanoparticles and quantum dots for applications ranging from catalysis to biomedical imaging. He did his PhD in the Department of Chemistry, University of Cambridge, UK, after which he was a Postdoctoral Fellow for two years at the Toshiba basic R&D Center, Japan. A native of the UK, he graduated with a Master of Chemistry from Oxford University, UK.

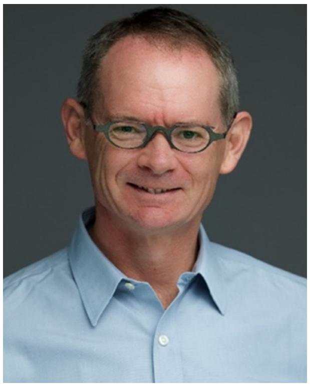

J. Justin Gooding

J. Justin Gooding graduated with a B.Sc. (Hons) degree from Melbourne University and completed a PhD degree at the University of Oxford and postdoctoral training at the Institute of Biotechnology in Cambridge University. After starting as a Research Fellow at the University of New South Wales, he gained Professorship in 2006. He is an Arc Industry Laureate Fellow leading a research team on surface modification and nanotechnology for biosensors, biomaterials and drug delivery.

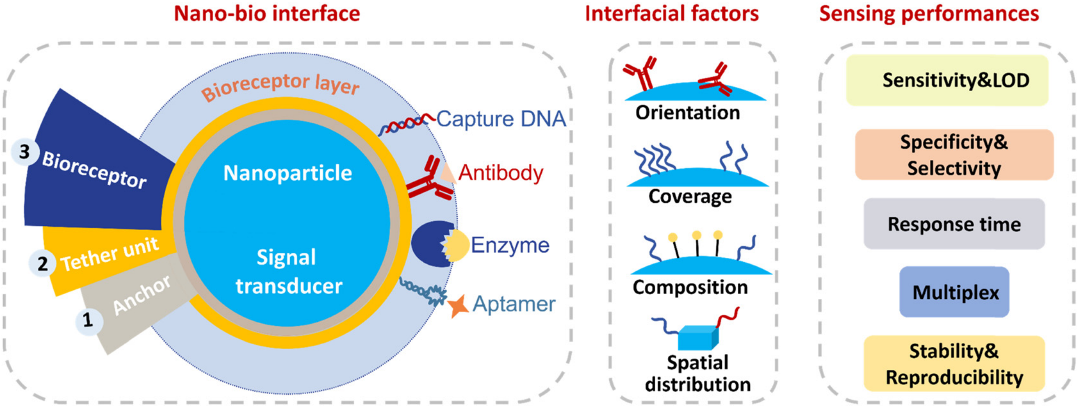

Fig. 1 Scheme of the nano–bio interface, the interfacial factors, and related sensing performances.

bioreceptors (2–15 nm). Consequently, when interactions between bioreceptors and analytes arise at the nanoscale surface with high curvature, interactions can be significantly different from that in solution or on a planar surface. Surface curvature, the accessibility of bioreceptor and heterogeneity of nanoparticle surfaces will all influence the bioreceptor–analyte interaction as well as the sensing performance.[19,20]

DNA-based biosensors are used as examples to clarify how nanoparticle surfaces affect the interaction between probe DNA and target DNA. DNA probes with known sequences are immobilized on nanoparticles to capture target DNA or target RNA through DNA–DNA or DNA–RNA hybridization. The binding efficiency of probe DNA can reach 100% if equal or excess amounts of target DNA are added in the solution-phase. When probe DNA is immobilized onto a planar surface, hybridization efficiency can be nearly 100% under an intermediate surface density of 1–2 × 10^{12} probes per cm^2. At higher or lower coverage, the efficiency of DNA hybridization can drop largely to only 20%.[21] In the case of nanoparticle surfaces with higher curvature, such as 5 nm gold nanoparticles (AuNPs) with a higher DNA density of 3.43 × 10^{12} probes per cm^2, the AuNPs–DNA conjugate diluted with 3-mercapto-1-propanol can also achieve 100% hybridization efficiency, whereas hybridization efficiency of nanoparticles without blocking is only 30–50%.[22] Therefore, whether the surface is planar or spherical, the efficiency of surface DNA hybridization is comparable to that in solution, provided that neither crowding among neighbouring strands nor undesired DNA–surface interactions occur.

The Mirkin group studied the thermodynamics of hybridization between AuNPs–probe DNA and fluorophore labelled target DNA.[23] Melting data of AuNPs–probe DNA (total 25 bases, including adenine $(A)_{10}$ and a 15-base recognition sequence) revealed that the binding constant of the nanoparticle-based probe was 2 orders of magnitude higher than that of the 15-base molecular quencher/fluorophore DNA pair in solution under identical conditions. This increasing binding strength was due to the high surface density of DNA on AuNPs rather than the absolute amount of DNA on the AuNPs. A further study conducted by the same group confirmed that the enhancement of DNA hybridization on the AuNPs compared with DNA hybridization in free solution was enthalpically controlled rather than entropically.[24] The introduction of nanoparticle surfaces mitigates against DNA from adopting enthalpically unfavorable conformations like those observed in solution.

Regarding the kinetics of DNA hybridization, the Levicky group found that hybridization rates on flat surfaces decreased by one to two orders of magnitude relative to those in solution, while dehybridization rates on flat surfaces exceeded those in solution by many orders of magnitude.[25] Similar trends have been observed on the surface of nanoparticles.[22] On 5 nm AuNPs, hybridization rates were slower than that in solution and dehybridization rates were accelerated on the AuNPs–target DNA conjugate, compared with target DNA in solution.[26] The hybridization rate for 20-base DNA can decrease from 4.2 × 10^4 to 2.0 × 10^4 M^{-1} s^{-1}, while the dehybridization rate can increase from 1.2 × 10^{-4} to 3.2 × 10^{-4} s^{-1}.

The hybridization of surface immobilized DNA was investigated at the single molecule level with the assistance of single molecule imaging technologies. Tao's group found that the hybridization rates for individual probe strands were dominated by the local spatial arrangement of the probe DNA layer, including probe density and the degree of clustering.[27,28] Recently, the Zijlstra group quantified the hybridization kinetics of AuNPs–DNA conjugates at the single particle level and investigated their dependence on DNA density. They discovered that lower DNA density could enhance hybridization kinetics by up to 15-fold, while dehybridization kinetics were almost unaffected by DNA density.[29] Overall, the surface of nanoparticles can affect the thermodynamics and kinetics of probe–target DNA interaction, either promoting or inhibiting, depending on specific surface conditions. Accordingly, the next section examines the detailed mechanisms behind the impact of nanoparticle surfaces on bioreceptor–analyte interaction.

2.2. Elucidating the mechanistic basis of nanoparticle surface-mediated interactions

The surface of nanoparticles affects the bioreceptor–analyte interaction and sensing performance in several ways.

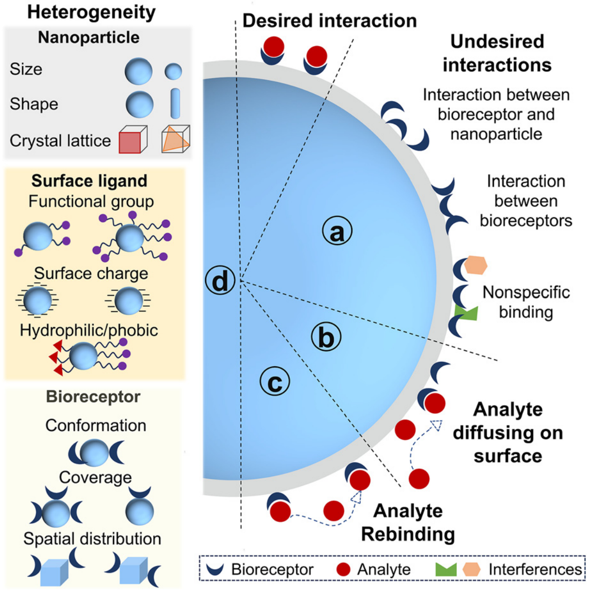

Fig. 2 Effects of nano–bio interfaces on bioreceptor–analyte interaction. Besides the desired bioreceptor–analyte interaction, the other interactions include undefined interaction between bioreceptors and nanoparticles, intermolecular interaction between bioreceptors and nonspecific binding of interferences (a); the adsorbed analyte can diffuse on the nanoparticle to bind the nearby bioreceptors (b); the analyte disassociating from the bound bioreceptor can be recaptured by the neighboring bioreceptor before diffusing away (c); the origins of heterogeneity of nano–bio interfaces (d).

Firstly, the existence of a surface brings additional interactions beyond the bioreceptor–analyte binding. These additional interactions are presented in Fig. 2a: (1) bioreceptors are likely to adsorb onto the nanoparticle surface. Such interactions may occur at ill-defined places on nanoparticles, potentially altering the conformation of bioreceptors or even causing denaturation.[30,31] (2) Bioreceptors may interact with neighboring bioreceptors due to high packing density of bioreceptors on the nanoparticle. Compared with flat surfaces however, high surface curvature allows more bioreceptors to be packed onto the surface of a particle before significant neighboring interactions arise.[32–34] Overly dense bioreceptor coverage causes steric hindrance for analyte binding, which reduces both efficiency and kinetics of bioreceptor–analyte interaction.[21] (3) Nonspecific adsorption of interfering proteins or molecules in biofluids can occur onto the nanoparticle surface, hindering the recognition between bioreceptors and analytes. These unspecific adsorptions can not only block specific signals but also exacerbate the selectivity of biosensors.[35,36]

Secondly, nonspecific but reversible adsorption of analytes onto nanoparticles can facilitate bioreceptor–analyte interaction. This adsorption proceeds *via* either three-dimensional (3D) diffusion of analytes in solution to bioreceptors on nanoparticle or two-dimensional diffusion of analytes along the particle surface after transient adsorption to regions lacking bioreceptors (Fig. 2b). The Schwartz group studied the hybridization dynamics of target DNA with immobilized probe DNA at a solution–solid interface at the single molecule level using total internal reflection fluorescence microscopy.[37] They found that 31% of target DNA bound to probe DNA on the fused silica and hybridized immediately, whereas 69% of target DNA adsorbed nonspecifically on the surface. Only 7% of this adsorbed population located the probe DNA *via* a two-dimensional surface search and successfully hybridized. The remainder desorbed and returned to solution, thereby repeating adsorption-search cycles. Meanwhile, the surface-bound DNA duplexes were more likely to melt into solution (77%) than to melt on the surface (23%). The DNA strands that melted onto the surface could either rehybridize after a brief lateral search or desorb back into solution.

Thirdly, analytes are more likely to rebind with the neighboring bioreceptors before diffusing away as the local concentration of bioreceptors confined on nanoparticles can be 10^5 fold higher than that in solution (Fig. 2c).[38] This diffusion-limited nanointerface can therefore result in a lower apparent dissociation rate constant for nano–bio conjugate/analyte binding.[38,39] The influence of bioreceptor density on rebinding at a planar surface had already been analyzed theoretically by Thompson and coworkers.[40] Under analyte-limited conditions, the likelihood of prompt rebinding increases with the higher association rates and receptor density, but decreases with increasing dissociation rates and the diffusion coefficients, following an approximate square root dependence. Rebinding tends to happen when the distance a molecule can diffuse in solution during its average surface bound time is less than a length scale set by the receptor surface density relative to analyte concentration. More recently, a single molecule study investigated the impact of DNA grafting density on surface-mediated DNA transport and hybridization.[41] The threshold value separating low and high grafting density regimes was $\sim 10^{12}$ probe per cm^2. Only 1–3% of target DNA was observed to associate with probes at dilute grafting density ($< 10^{12}$ probe per cm^2). Adsorbed target DNA frequently performed unproductive searches and flew to other distant locations *via* desorption-mediated diffusion, rendering rehybridization events rare. In contrast, approximately 20% of target DNA hybridized to the immobilized DNA with high density, typically in the vicinity of initial adsorption sites. Target DNA rehybridized following a dehybridization event at high density of probe DNA. As target-induced nanoparticle assembly is widely exploited in biosensing, dense bioreceptors also induce a cooperative effect to nanoparticle assembly.[42] Such multivalent cooperativity between nanoparticles enhances the equilibrium binding constant and accelerates agglomerate formation kinetics.[43,44] For instance, the Mirkin group found that the equilibrium binding constant for a 15 nm AuNPs–DNA conjugate (24 base strands with a 3 base pair recognition domain) is ~ 3 orders of magnitude higher than that of the corresponding system in the absence of nanoparticles.[45]

Lastly, another important aspect is the heterogeneity introduced by nano–bio interfaces (Fig. 2d). Heterogeneity originates from multiple sources. Primarily, nanoparticles themselves are heterogeneous in size, shape, charge, roughness, surface defects and crystallographic facets.[46–49] Furthermore, the immobilization of bioreceptors onto these surfaces generates additional heterogeneities.[50,51] The presence of multiple attachment sites on both nanoparticles and bioreceptors makes precise control over the conformation, orientation, and density of bioreceptors on individual particle exceptionally challenging. Consequently, the surface chemistry of the nanoparticles, the immobilization strategy and the structure of bioreceptors collectively contribute to the heterogeneities of nano–bio interfaces. Additionally, bioreceptor–analyte interactions occurring at a nanoscale surface are inherently heterogeneous processes. This heterogeneity at nano–bio interfaces has attracted significant attention as advancements in high-resolution single-molecule techniques now can unravel properties hidden behind ensemble measurement.[52,53] In the context of single molecule biosensing, where the detection operates at the level of individual entities, this heterogeneity becomes particularly pronounced. Any variability in the nano–bio interface can translate directly into signal fluctuation, and substantial variation will further complicate data interpretation and compromise measurement precision.[54] The Prins group comprehensively studied how reactivity variability of biofunctionalized nanoparticles was determined by various independent heterogeneities.[55] They classified the contributing factors into two categories: stochastic heterogeneity and non-stochastic heterogeneity. Stochastic heterogeneity arises from the discrete nature of bioreceptor immobilization, leading to a particle-to-particle variation in bioreceptor number following Poisson statistics. Non-stochastic heterogeneity refers to physical and chemical differences among nano–bio conjugates, such as the nanoparticle size, surface roughness, and the local chemical microenvironment. Their work demonstrated that reactivity variability could be stabilized by employing a large number of bioreceptors, which indicated the use of large amounts of nanoparticles, utilization of the available interaction area, suitable particle size and bioreceptor density. A key implication is that a large population of biofunctionalized nanoparticles needs to be measured to minimize variability in nanoparticle-based single molecule biosensors.

3. Interfacial parameters affecting sensing performances

There is no one-size-fits-all solution for the optimal interfacial design to enhance sensing performance, as specific applications, bioreceptors, transductions and materials employed all affect the interfacial design. Here, we focus on four critical interfacial parameters, including orientation of bioreceptors, coverage of bioreceptors, compositions of mixed ligands and spatial distribution of bioreceptors on nanoparticles. How each interfacial factor boosts the sensing performance is demonstrated with corresponding examples. Meanwhile, strategies to tailor and characterize these nano–bio interfacial parameters are summarized. To standardize the types of nanoparticles and bioreceptors across various biosensors, if applicable, AuNPs are preferentially selected as model nanoparticles and DNA serves as a model bioreceptor with priority. In many cases the same principles apply to other bioreceptors such as antibodies and peptides. Where significant differences or considerations from DNA based bioreceptors are required, these will be highlighted with an emphasis on antibodies as the representative example instead of DNA, particularly in the section on bioreceptor orientation.

3.1. Orientation of bioreceptors

3.1.1. Orientation of antibodies. The orientation of antibodies on nanoparticles is critical to accessibility of antigens, which directly determines all the sensing characteristics of biosensors.[56] Immunoglobulin G (IgG) is highlighted here as it is the predominant type of antibody in blood and extracellular fluids, as well as its wide application in biosensing and diagnostics. The molecular weight of IgG is approximately 150 kDa with dimensions of 14.5 × 8.5 × 4.0 nm.[57] A detailed depiction of IgG consisting of four polypeptide chains—two heavy chains (50 kDa, in blue) and two light chains (25 kDa, in green), joined together by disulfide bonds (in red)—is given in Fig. 3a. Fragment antigen-binding (Fab) is composed of both constant and variable domains from paired heavy and light chains. The 3D structure of IgG comprises fragment crystallizable (Fc) and Fab regions, shown in Fig. 3b.[58] The antigen-binding epitopes, complementarity-determining regions, are very small and localized at the end of the Fab region. In addition to conventional antibodies, nanobodies, also called single domain antibodies or variable heavy domains of heavy chains, are the small antigen binding fragments derived from heavy chains. With a molecular mass of ∼15 kDa and dimensions of 2.5 × 4 nm, nanobodies possess superior thermostability, broader pH tolerance, nano-/picomolar affinities and improved permeability across tissue and blood–brain barrier, rendering them highly attractive for advanced immunoassays and therapeutic applications.[59,60] Technically, the orientations of antibodies on nanoparticles are depicted to be head-on (both Fabs on the surface), tail-on (Fc on the surface), side-on (Fc and one Fab on the surface) or flat-on (all fragments on the surface), as demonstrated in Fig. 3c.[10] To achieve optimal antigen-binding activity, the most favorable orientation of antibodies on nanoparticles is tail-on as it provides full accessibility of antigen-binding sites.

The approaches of immobilizing antibody onto nanoparticles include direct physical adsorption, covalent/non-covalent immobilization and antibody-directed synthesis of nanoparticles.[61–63]

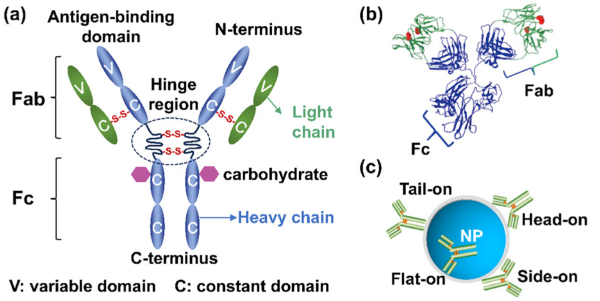

Fig. 3 (a) Schematic depiction of IgG. (b) 3D structure of IgG, consisting of the Fc region and the Fab region. Reprinted with permission,[58] Copyright 2018, Springer Nature. (c) Four typical orientations of an antibody on a nanoparticle.

Despite its ease of immobilization, direct physical adsorption based on electrostatic forces or hydrophilicity/hydrophobicity is relatively unstable and it is difficult to control the antibody orientation. The pH of the immobilization buffer has been leveraged to regulate the orientation of antibodies during adsorption as pH can influence both charge distribution and hydrophobicity of antibodies and surface charge of nanoparticles.[64–66]

Driskell's group has studied the impact of pH on the orientation of the anti-horseradish peroxidase (anti-HRP) antibody adsorbed on AuNPs.[67] As the specific sequence and structure of the anti-HRP antibody are unavailable, IgG1 serves as a model protein due to its fully characterized structure in the Protein Data Bank (PDB). The calculated charge distributions of IgG1 at different pH values are presented in Fig. 4a. As the pH increases from 7.5 to 8.5, the

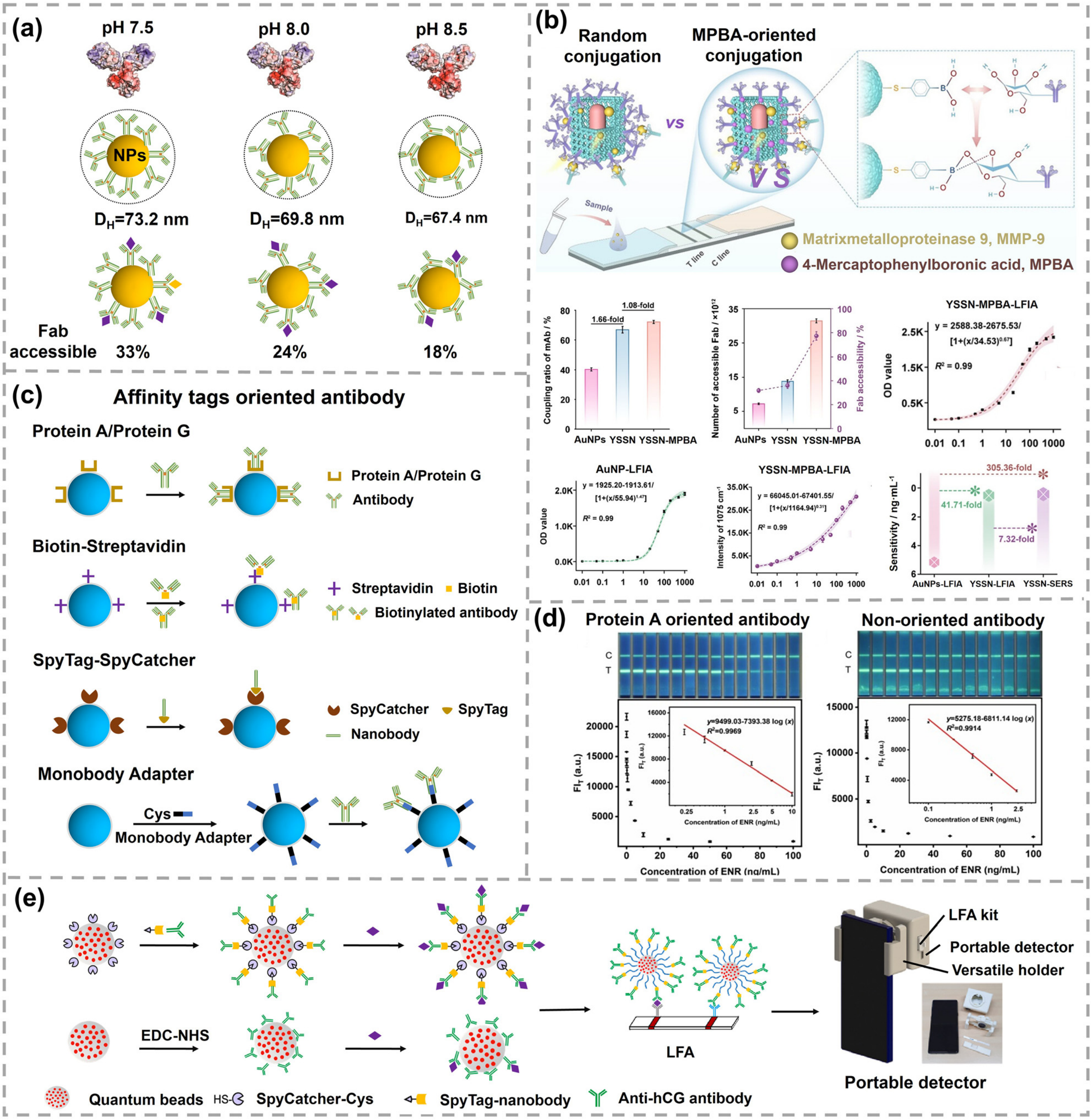

Fig. 4 (a) Charge distribution calculated for the IgG1 antibody and corresponding hydrodynamic diameters of AuNPs–antibody conjugates and Fab accessibility at different pH values. Reprinted with permission,[67] Copyright 2019, American Chemical Society. (b) Schematic illustration of MPBA-oriented antibody conjugation and sensing performance for MMP-9 detection. Reprinted with permission,[75] Copyright 2025, American Chemical Society. (c) Oriented immobilization of antibody on nanoparticles based on affinity tags, including protein A/protein G, biotin–streptavidin, SpyTag-SpyCatcher and Fc-targeting monobody. Reprinted with permission,[88] Copyright 2022, American Chemical Society. (d) Pictures of LFA strips and standard curves of protein A oriented and non-oriented probes. Reprinted with permission,[78] Copyright 2023, Elsevier. (e) Oriented antibody conjugates adopting SpyTag-SpyCatcher and their application in cellphone-based portable detection. Reprinted with permission,[87] Copyright 2022, Elsevier.

degree of protonated amino acids decreases and the number of localized positive regions of IgG1 decreases. As the electrostatic interaction between the positively charged region of the antibody and negatively charged AuNPs is the main driving force for adsorption, the surface charge distribution of the antibody can significantly affect its orientation on nanoparticles. Theoretically, the thickness of the antibody layer on 60 nm AuNPs is minimum of 9 nm for flat-on orientation or maximum of 28 nm for head-on or tail-on orientation. Correspondingly, the footprint of an antibody in tail-on/head-on orientation is 38 nm^2, while the footprint in flat-on orientation is 119 nm^2. Experimentally, the hydrodynamic sizes of AuNPs–anti-HRP antibody conjugates were 73.2 nm, 69.8 nm and 67.4 nm at pH 7.5, 8.0, and 8.5, respectively. The measured antibody loading increased from 171 to 240 antibodies per AuNP with increasing pH from 7.5 to 8.5. Both the decreasing hydrodynamic size and antibody loading indicated a higher proportion of antibodies oriented in tail-on or head-on orientation with decreasing pH. To further confirm the orientation of the anti-HRP antibody, its binding capacity toward HRP was tested. The antigen-binding capacities of anti-HRP antibody–AuNP conjugates prepared at pH 7.5, 8.0, and 8.5 were 33%, 23%, and 18%, respectively (Fig. 4a). Since the binding constant of the anti-HRP antibody remained unchanged across this pH range (dissociation constant (K_d) ~ 11 nM), the decreased binding capacity suggested that more anti-HRP antibodies were preferred in tail-on orientation at lower pH. The orientation of the anti-HRP antibody was further evaluated using aggregation-based assays with anti-IgG Fab-specific antibodies. Anti-HRP antibodies adsorbed onto AuNP at pH 7.5 exposed a larger number of accessible Fab sites, indicating their tail-on orientation. Similarly, Tonigold's work found the anti-CD63 (a cell surface antigen) antibody preferably adsorbed on polymeric nanoparticles through the Fc region at pH 6.1.[58] The oriented anti-CD63 antibody exhibited better capture performance to target cells. As pH varies the immobilization microenvironment and largely affects the antibody orientation, it is reasonable to optimize and control the pH of immobilization buffer precisely when preparing antibody–nanoparticle conjugates.

Covalent immobilization based on the abundant functional moieties of antibodies, such as amino, carboxyl, and sulfhydryl groups, is relatively simple to achieve but typically results in random orientation. Detailed reviews on the covalent immobilization of antibody are covered elsewhere.[15,68,69] To achieve orientation-controlled covalent immobilization of antibodies, functional groups located specifically outside the Fab region are typically used, such as polysaccharide chains in the Fc region and disulfide bonds between two heavy chains (Fig. 3a).[70,71] For example, intact antibodies can be reduced into half antibodies to orientally immobilize on gold surfaces *via* their two native thiol groups, exhibiting 2-fold improved sensitivity without loss of selectivity.[72] Wu *et al.* further introduced half antibody fragments as bioreceptors in a microcantilever-based immunosensor for ginsenoside Re detection.[73,74] Compared with intact antibodies immobilized *via* thiolated secondary antibodies, immunosensors utilizing half antibodies as bioreceptors exhibited a 1500–4000-fold increase in sensitivity. Meanwhile, the LOD of immunosensors based on half-antibodies was 1 pg mL^{-1}, whereas the LOD of the immunosensor adopting an intact antibody was approximately 0.5 ng mL^{-1}. In addition to disulfide bonds, Sun and coworkers developed lateral flow immunoassay (LFIA) using plasmonic yolk–shell-satellite nanostructures (YSSNs) functionalized with 4-mercaptophenylboronic acid (MPBA).[75] The boronic acid group of MPBA forms stable cyclic esters with *cis*-diol groups on the carbohydrate moieties in the Fc region of antibodies, orienting the Fab region outward from the nanoparticle surface, maximizing their accessibility of Fab regions for the target antigen (Fig. 4b). The YSSN–MPBA conjugate achieved an antibody conjugation efficiency of 72%, which was 1.79-fold and 1.06-fold higher than those of YSSNs (67%) and AuNPs (40%), respectively. Additionally, the antibody orientation efficiency of the YSSN-MPBA conjugate reached 77%, significantly exceeding 36% observed for randomly conjugated antibodies on YSSNs, directly resulting in a higher number of accessible Fab sites. Furthermore, the test results of YSSN-MPBA-LFIA and AuNP-LFIA were obtained using a handheld optical densitometer. Based on the optical density (OD) values of the test line, the LODs were 0.041 ng mL^{-1} for YSSN-MPBA-LFIA and 1.71 ng mL^{-1} for AuNP-LFIA, respectively. Owing to the strong Raman scattering signal generated by the MPBA–YSSN structure, this platform was also suited for SERS sensing. The SERS-based LFIA achieved a 305-fold improvement in LOD (0.0056 ng mL^{-1}) compared to the conventional AuNP-LFIA (1.71 ng mL^{-1}). Meanwhile, this platform demonstrated robustness against the matrix effect under Raman detection mode, maintaining high sensitivity and accuracy in serum and tear, with excellent recovery rates ranging from 86.4 to 98.2%.

As for non-covalent immobilization, affinity tags are adopted to modulate the orientation of antibodies.[76] Protein A and protein G are frequently employed to regulate antibody orientation through specifically binding the Fc region of IgG (Fig. 4c).[77] Hu and coworkers conjugated the anti-enrofloxacin antibody onto carboxyl-functionalized microspheres in an oriented manner utilizing cysteine-tagged recombinant protein A (Fig. 4d).[78] The carboxyl on microspheres was activated by EDC (1-ethyl-3-(3-dimethylaminopropyl) carbodiimide) and 2-chloroacetohydrazide. Next, the recombinant protein A was conjugated onto the activated microspheres by a substitution reaction between chloroacetamide and sulfhydryl. The anti-enrofloxacin antibody was then bound to recombinant protein A on microspheres, resulting in the formation of oriented antibodies. The proportion of tail-on orientation was significantly higher for the oriented antibody-microspheres (89.1%) than that for the non-oriented counterparts (62.1%), indicating more accessible antigen-binding sites. Consequently, the LODs for enrofloxacin were 0.035 ng mL^{-1} for the oriented probe and 0.079 ng mL^{-1} for the non-oriented probe. Moreover, the linear range for the oriented probe was 0.25–10 ng mL^{-1}, which was wider than that of the non-oriented probe (0.1–2.5 ng mL^{-1}). However, protein A and protein G themselves are typically immobilized on nanoparticles *via* EDC-NHS (*N*-hydroxysuccinimide) crosslinking in a random orientation, which inevitably leads to partially random orientation of the capture antibodies. Biotin–streptavidin is another affinity tag to orientally immobilize antibodies, requiring site-specific biotin modification of antibodies (Fig. 4c). Sulfhydryl groups located at the hinge region of antibodies are commonly harnessed for site-selective biotinylation.[79] A site-selectively biotinylated Fab fragment of an antibody demonstrated 20-fold higher recognition capacity than random biotinylation.[80]

Except for natural antibodies, engineered antibodies have been utilized to achieve oriented immobilization. Specific amino acids can be recombinantly introduced at particular positions within an antibody, thereby offering distinct anchoring sites for tethering antibodies onto nanoparticles.[81] In parallel, genetic fusion of proteins with binding modules can also provide active-site accessibility for immobilization.[82,83] SpyTag and SpyCatcher are a pair of peptide partners that can form irreversible isopeptides within minutes.[84] A nanobody-SpyTag fusion protein can selectively couple to SpyCatcher functionalized surfaces with controlled orientation.[85] Compared with a random-oriented nanobody dimer, the signal/background ratio of detecting Dengue virus nonstructural protein 1 (DENV NS1) increased by at least a factor of 5 using the oriented nanobody dimer built on SpyTag-SpyCatcher.[86] In a recent study, Jongnam Park orientally conjugated an antibody onto polystyrene-*co*-poly(acrylic acid)-coated quantum beads utilizing SpyCatcher and a SpyTag-fused Fc-specific nanobody (Fig. 4e).[87] This oriented conjugate resulted in an ∼91% accessibility of the Fab region, a significant increase compared to randomly conjugated antibodies using EDC-NHS chemistry (∼23.4% accessibility). The number of accessible antigen-binding sites per bead increased dramatically from 389 to 1978. The LFA utilizing oriented conjugates demonstrated an LOD of 5.1 pg mL^{-1} for human chorionic gonadotropin, an ∼6-fold improvement in sensitivity compared to that of the LFA using randomly oriented antibodies. While effective, antibody engineering is of high-cost and labor-intensive, requiring screening and engineering distinct antibodies according to specific antigens. To overcome the above limitations, a more adaptable approach was creatively developed.[88] An engineered Fc-binding monobody, including a cysteine to enable thiol-based coupling onto poly(lactic acid)–poly(ethylene glycol) (PLA–PEG) nanoparticles, acts as an adapter between nanoparticles and antibodies (Fig. 4c). The conjugation efficiency of antibodies with a monobody adapter was substantially higher than that coupled by EDC-NHS (47 *vs.* 23 mg of Ab per mg of NPs). This novel immobilization strategy resulted in a significant improvement in binding efficiency (>1000-fold) relative to the standard EDC-NHS coupling. In addition to the above adapters, DNA, aptamers and peptides have also been harnessed as affinity tags to mediate the orientation of antibodies.[89–92]

Besides conjugating antibodies on the pre-synthesized nanoparticles, antibody-directed synthesis of nanoparticles has emerged as a novel approach to regulate antibody orientation. Metal–organic frameworks (MOFs) have emerged as a suitable scaffold for antibody and enzyme immobilization because of their well-defined pore structure, excellent chemico-thermal stability and high surface area. One-step synthesis of an oriented antibody-decorated MOF was presented by Falcaro's group.[93] A Zn-based zeolitic imidazolate framework (ZIF), ($Zn_2(mIM)_2(CO_3)$), produced from Zn^{2+} and 2-methylimidazole (mIM), was triggered by the Fc region of the antibody (Fig. 5a). As the negatively charged carboxyl and histidine groups were mostly located in the Fc region of the antibody, Zn^{2+} accumulated in the Fc region and triggered the formation of ZIFs. The Fc region of antibodies was partially inserted within ZIFs while the Fab region protruded from ZIFs, yielding oriented antibody-ZIF conjugates. Quantum dots (QDs) were then encapsulated in the antibody–ZIF conjugates to generate a fluorescence signal for diagnostic applications. This ordered configuration preserved target binding capacity compared to the antibodies randomly conjugated on QDs. Similarly, Zhang *et al.* coated various nanoparticles including gold nanorods (AuNRs), layered double hydroxide, superparamagnetic iron oxide nanoparticles, and ultrasmall superparamagnetic iron oxide using an orientated antibody-ZIF-8 composite *via* a generalizable film-coating approach (Fig. 5b).[94] The antibodies selectively bound to ZIF-8 through histidine-rich Fc regions, thereby exposing the functional Fab regions to targets. The generated ZIF8-antibody@NPs exhibited high antibody loading and targeting efficiencies. Notably, the MOF-orientated antibodies in both studies exhibited the enhanced capture efficiency in targeting cancer cells. Recently Tian *et al.* applied the oriented antibody–MOF to wearable, label-free and persistent sweat cortisol detection (Fig. 5c).[95] This full integrated system exhibited satisfactory on-body biosensing performance with a good linear detection range from 1 pg mL^{-1} to 1 μg mL^{-1} and a LOD of 0.26 pg mL^{-1}. Meanwhile, this wearable sensor demonstrated good persistence in detecting cortisol, with only 4.1% decay after 9 days of storage.

In addition to MOFs, Chen's group prepared IgG-encapsulated gold nanoclusters (IgG-AuNCs) with high photoluminescence quantum yield and satisfactory bioactivity *via* a facile biomineralization process.[96] By contrast, IgG/AuNC conjugates produced by coupling IgG to pre-synthesized AuNCs *via* EDC-NHS chemistry exhibited poor stability, leading to the pronounced nonspecific adsorption and elevated background signals. Consequently, under identical concentration of anti-human IgG, the signal change obtained in IgG/AuNC conjugate-based assay was markedly lower than that achieved with IgG-AuNCs in dot-blot immunoassay (Fig. 5d). Later, IgG-AuNCs were adopted as a "two in one" probe in electrochemiluminescence immunoassay, offering facile preparation, rapid detection, and good analytical performance in spike-and-recovery tests using 0.1% diluted serum.[97] More recently, his group developed human epidermal growth factor receptor 2 (HER2)-specific monoclonal antibody (herceptin)-functionalized AuNCs for the quantitative detection of HER2 expression levels in breast cancer patients using electrochemiluminescence immunoassay (Fig. 5e). This assay showed high consistency with the standard and commercial ELISA kit with the Pearson correlation coefficient of 0.993. Serum HER2 extracellular domain levels were positively correlated with tissue HER2 expression determined by immunohistochemistry and fluorescence *in situ* hybridization, with particularly pronounced differences among the immunohistochemistry 3+, 2+, 1+, and 0 groups ($p < 0.001$).[98]

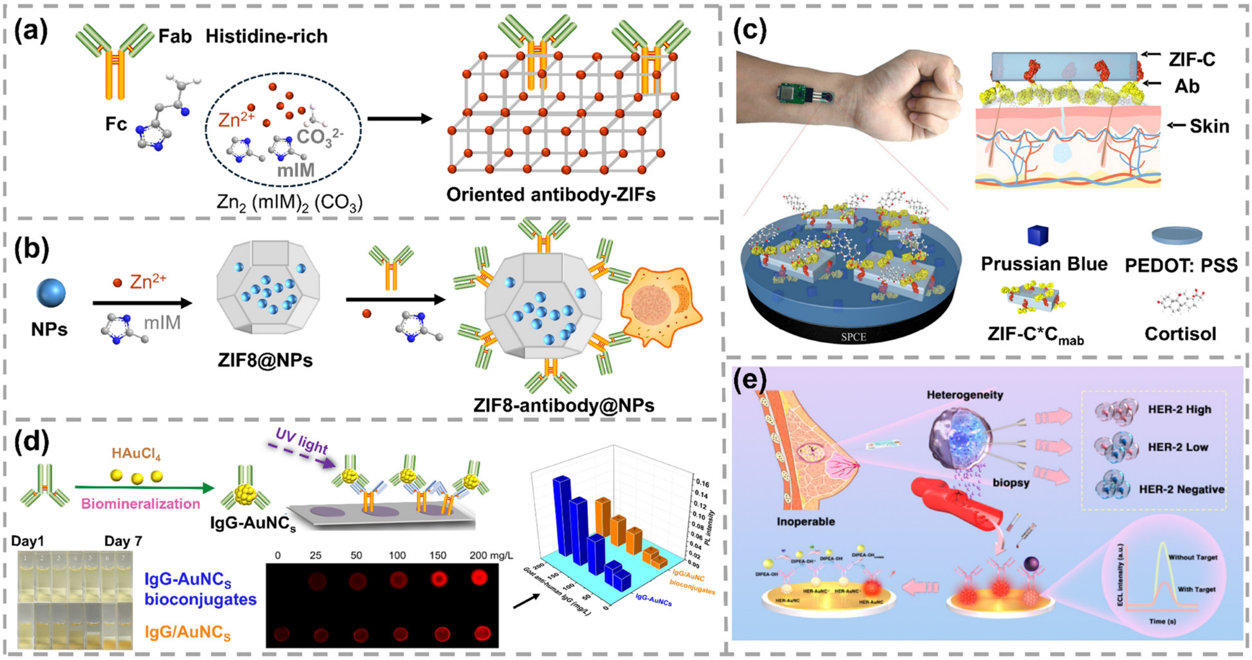

Fig. 5 (a) The nucleation of ZIFs was triggered by the Fc region of the antibody. Reprinted with permission, Copyright 2022, Wiley-VCH.[93] (b) Illustration of the site-specific antibody coating on nanoparticles based on the interaction between the histidine-rich Fc region of antibodies and ZIF-8. Reprinted with permission, Copyright 2023, Wiley-VCH.[94] (c) Scheme of the working electrode for cortisol sensing. The ZIF-8@antibody was drop-coated after the electrodeposition of Prussian blue. PEDOT:PSS stands for poly(3,4-ethylenedioxythiophene):polystyrene sulfonate. Reprinted with permission, Copyright 2023, American Chemical Society.[95] (d) Illustration of the dot-blot immunoassay using IgG-AuNC conjugates. Reprinted with permission, Copyright 2019, American Chemical Society.[96] (e) ECL platform for detecting HER2 in breast cancer patients using herceptin-functionalized AuNCs. Reprinted with permission, Copyright 2025, American Chemical Society.[98]

3.1.2. Orientation of DNA.

Single-stranded DNA (ssDNA) is more conformationally flexible compared with antibodies. The persistence length of ssDNA is 1–3 nm, equating to 3–10 bases, whilst the persistence length of double-stranded DNA (dsDNA) is approximately 40–50 nm. Therefore, surface bound probe DNA is prone to lying on or forming a coil on nanoparticles, which restricts hybridization between target DNA and probe DNA. The ideal conformation of probe DNA to achieve efficient hybridization is in an upright and extended conformation with sufficient flexibility. Meanwhile, the spacing between neighboring DNA strands on nanoparticles should be large enough to minimize interstrand physical contact or electrostatic interactions.[99] DNA can directly adsorb on various nanomaterials *via* coordination between the phosphate backbone and metal atoms (*e.g.* Au and Ag), electrostatic attraction, or π–π stacking (for carbon-based materials).[100] For more details on how DNA interacts with various nanoparticles, refer to other reviews.[101,102] As the chemically synthesized DNA is easily functionalized with thiol, amine, biotin or other functional groups, DNA can be conjugated onto nanoparticles through these ligands. Among them, the strong affinity of gold–thiol (Au–S) bonds allows thiolated DNA to form a self-assembled monolayer on AuNPs. In addition, AuNPs possess well-developed synthesised methods and unique optical/electrochemical properties. Therefore, AuNPs–DNA conjugates are adopted as model systems in this section due to their wide range of applications and well-established interfacial knowledge.[103,104]

Strategies for achieving an upright and extended conformation of probe DNA on AuNPs include adding spacers, backfilling after bioconjugation, freezing-directed stretching, and utilizing DNA frameworks. Spacers, including alkyl, short DNA sequences or polyethylene glycol (PEG) units, are inserted in the end of probe DNA to avoid undesired interaction between the recognition region of DNA and nanoparticle surface (Fig. 6a).[105] As the recognition region of the probe DNA is spatially isolated from the AuNPs, the probe DNA maintains a higher binding capacity for the target. The affinity of nucleobases toward gold ranks as: thymine (T) < cytosine (C) < guanine (G) < adenine (A).[106] The Fan group creatively adopted a polyadenine (polyA) tail as an effective anchoring block and systematically investigated its effect on DNA hybridization (Fig. 6b). The hybridization efficiency of AuNPs–thiolated DNA conjugates without polyA as a spacer was only 5–10% at a loading density of 50 strands per AuNP.[107] In contrast, once introducing polyA as an anchoring block instead of thiol, the hybridization efficiency increased with the length of polyA, from 42% for polyA$_5$ to 90% for polyA$_{30}$, even though the number of DNA per AuNP decreased from 70 to 10. Furthermore, how the polyA feature affected the hybridization kinetics and response time was investigated using a plasmonic sensor. The working principle is that target DNA would bring two AuNPs–probe DNA conjugates together, resulting in red shift in the plasmonic resonance peak. This plasmonic sensor exhibited a visualizable color change within 10 min for AuNPs–DNA conjugated with polyA. However, it took more than 12 h to

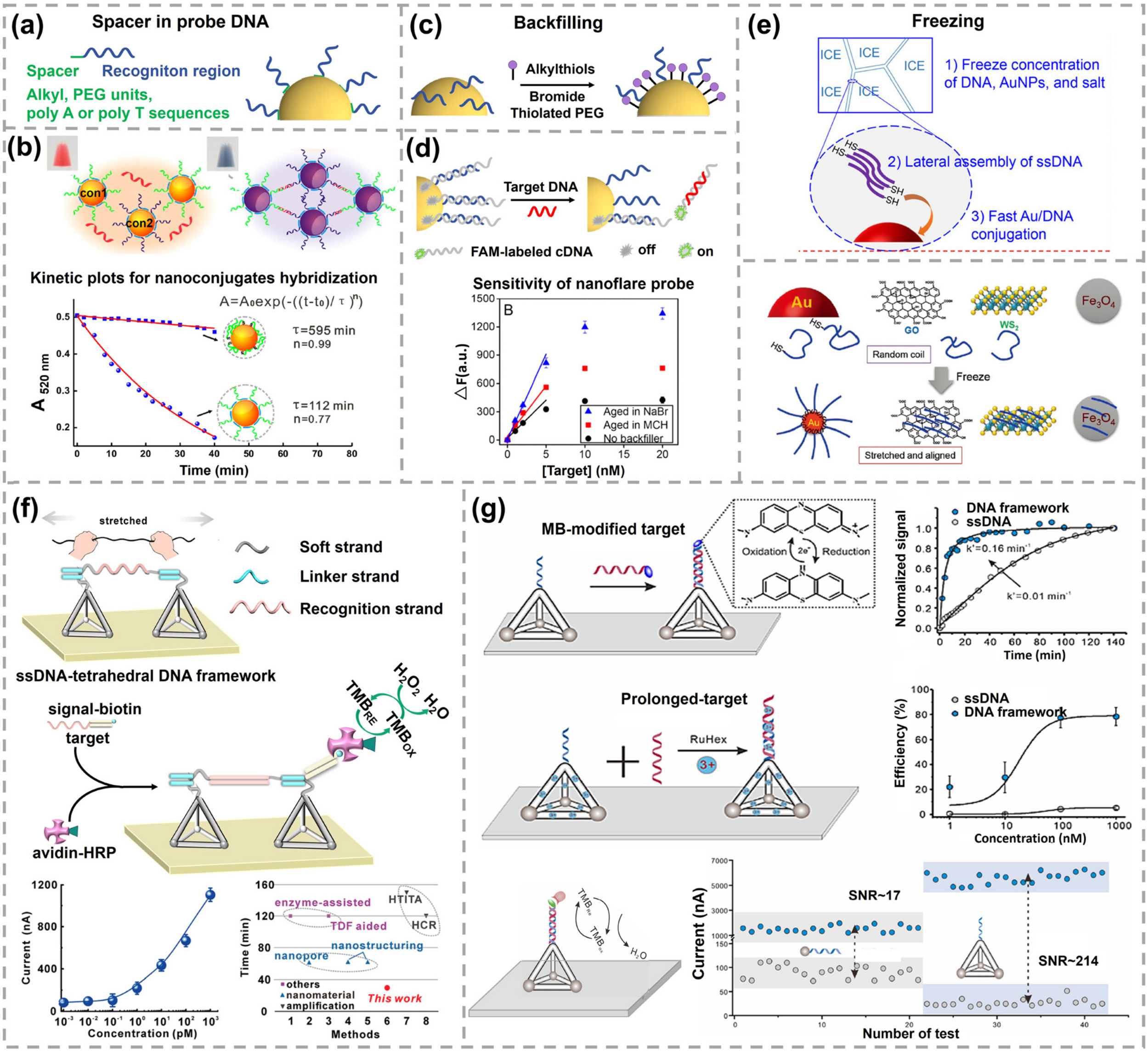

Fig. 6 (a) Different spacers for probe DNA. (b) Detection principle of plasmonic biosensors and kinetic plots of AuNPs–DNA nanoconjugates. Reprinted with permission,[107] Copyright 2013, American Chemical Society. (c) Regulate the conformation of DNA through backfilling. (d) Schematic illustration of nanoflare probes and their response curves. Reprinted with permission,[114] Copyright 2018, American Chemical Society. (e) Freezing-directed conjugation of DNA onto AuNPs and other nanomaterials. Reprinted with permission,[116,117] Copyright 2019, American Chemical Society and Copyright 2019, Wiley-VCH. (f) Schematic representation of the signal transduction mechanism of an ssDNA-tetrahedral DNA framework complex and its sensing performances. Reprinted with permission,[121] Copyright 2020, American Chemical Society. (g) Sensing characterization of recognition interfaces assembled by a tetrahedral DNA framework. Reprinted with permission,[122] Copyright 2025, American Chemical Society.

display a color change for AuNPs–DNA conjugates without polyA. Quantitative analysis of kinetics was performed by fitting response curves using the Avrami law (inset of Fig. 6b). In the equation, t_0 is the reaction onset time, τ is the characteristic time that depends on the reaction rate and aggregation geometry, and n is the Avrami exponent related to the physical mechanism of aggregate growth. The τ and n for AuNPs–DNA conjugates with polyA were 112 min and 0.77, while τ and n for AuNPs–DNA conjugates without polyA were 595 min and 0.99, respectively. Later on, the Fan group further quantitatively studied the hybridization thermodynamics and kinetics of AuNPs–DNA conjugates with polyA.[108] Regarding the thermodynamics of DNA hybridization, the free energy of the DNA duplex in solution (-31.96 kcal mol^{-1}) is higher than that of the DNA duplex on AuNPs immobilized *via* the Au–S bond (-22.09 kcal mol^{-1}). The free energy cost between the DNA duplex in solution and the DNA duplex on AuNPs is 9.87 kcal mol^{-1}, indicating that DNA duplexes are less stable on AuNPs. When the length of polyA increases from 5 to 40 nucleotides, the free energy cost decreases from 11.02 to 4.5 kcal mol^{-1}, suggesting the improved DNA duplex stability on AuNPs. Consistent with this trend, the apparent binding constant enhances over 4 orders of magnitude with the increasing length of polyA, from 2.3×10^{15} to 1.4×10^{20} M^{-1} cm^{-1}. Meanwhile, the rate constants of hybridization increase from 0.003 to 0.021 s^{-1} when the polyA tail is extended from 5 to 40 nucleotides.

Backfilling using alkanethiols and thiolated PEG also contributed to the upright orientation of DNA (Fig. 6c).[109–111] The alkanethiol 6-mercaptohexanol (MCH) is commonly used to backfill the prepared AuNPs–DNA conjugates. The hybridization efficiency can reach 100% for a mixed layer of ssDNA and MCH on planar gold.[112] Nevertheless, the suitable concentration range for MCH backfilling is narrow (around 100 mM). If the added MCH concentration is too high, AuNPs would undergo aggregation as less DNA strands to maintain stability of AuNPs.[113] Bromide was reported as an alternative backfiller with higher tolerable concentration to 300 mM by the Liu group.[114] The hybridization efficiencies of AuNPs–DNA conjugates without backfilling and backfilling with MCH or Br^- were investigated. Fluorescein (FAM)-labeled complementary DNA was added to hybridize with probe DNA on AuNPs. Each AuNP hybridized with only ∼7 cDNA strands without backfilling. The number of hybridized complementary DNA per AuNP increased to 22 and 20 after backfilling with Br^- (200 mM) and MCH (100 μM), respectively. A nanoflare probe was constructed based on AuNPs–DNA conjugates and FAM–complementary DNA for preliminary biosensing applications. Nanoflares are spherical nucleic acids (SNA) assembled on AuNPs that release a fluorescent reporter upon target binding.[115] The fluorescence of the FAM fluorophore on complementary DNA was quenched by AuNPs in the absence of target DNA. Upon target DNA binding and displacing the FAM-complementary DNA from AuNPs, the fluorescence intensity significantly increased (Fig. 6d). The saturated signal of the nanoflare backfilled with Br^- was 50% higher than that with MCH. Also, the sensitivity of nanoflares was 70% higher for Br^- backfilling than that for MCH, indicating superior sensing performance of Br^- in this DNA biosensor. Additionally, the Liu group also found that freezing can stretch and align the probe DNA based on lateral DNA–DNA interactions (Fig. 6e). DNA oligonucleotides can be readily adsorbed onto a range of nanomaterials, including AuNPs, graphene oxide (GO), iron oxide, and WS_2 with a stretched conformation upon freezing.[116,117] The freezing-directed assembly of DNA on gold electrodes was used to enable robust electrochemical sensing in whole blood.[118]

Similarly, DNA frameworks, regarded as organic nanoparticles, are also utilized to tailor the conformation of probe DNA on selective sites.[119] The Song group employed a tetrahedral DNA framework to keep capture DNA extended from the surface of screen-printed carbon electrodes.[120] The rough surface of screen-printed carbon electrodes results in the disorder of capture DNA and the nonspecific adsorption of signaling probes, which sterically hinders the target binding. The capture DNA hanging on tetrahedral DNA frameworks possesses enhanced capturing efficiency, leading to hundred times increase in both the signal-to-noise ratio and sensitivity compared with the surface directedly decorated with a capture probe. This sensing platform can be extended to a variety of target molecules as the recognition DNA sequences on tetrahedral DNA frameworks can be tailored to match different targets. Three representative targets, including miRNA-141, thrombin, and ATP, have been successfully detected. Beyond single tetrahedral DNA frameworks, Fan and his coworkers creatively utilized two tetrahedral DNA frameworks to extend probe DNA, shown in Fig. 6f.[121] A tetrahedral DNA framework-based electrochemical biosensor was built to investigate the stretching effect on DNA hybridization. Probe DNA–tetrahedral DNA frameworks were immobilized on a gold electrode, one end of target DNA was hybridized to the tetrahedral DNA framework, and the other end of target DNA was hybridized with biotin labeled signaling DNA. Subsequently, avidin-HRP bound to a biotin labelled signaling strand and catalyzed the oxidization of tetramethylbenzidine, generating an electrochemical signal proportional to the concentration of target DNA. The LOD of this stretching DNA-enabled electrochemical biosensor can be as low as 1 fM. This response time was within 30 min, substantially faster than that of many previously reported biosensors. Both the hybridization kinetics and hybridization efficiency of the probe DNA were significantly improved by stretching DNA with two tetrahedral DNA frameworks. More recently, the same group further utilized tetrahedral DNA frameworks to engineer a biosensing interface with densely monodispersed DNA probes.[122] Tetrahedral DNA frameworks serve as rigid and programmable frameworks to precisely control the conformation and spatial organization of pendant ssDNA probes on the electrode (Fig. 6g). By effectively suppressing the nonspecific adsorption and inter-probe entanglement, the tetrahedral DNA framework-programmed interface exhibited superior performance: the hybridization kinetics of a tetrahedral DNA framework immobilized DNA probe exhibited a 16-fold higher rate constant due to the improved probe accessibility (0.16 min^{-1} for tetrahedral DNA framework immobilized ssDNA *vs.* 0.01 min^{-1} for ssDNA). The K_d of tetrahedral DNA framework immobilized ssDNA was 18.12 nM, 3-fold lower compared with that of ssDNA (55.11 nM). A dramatically higher signal-to-noise ratio of 214 (*vs.* 17 for ssDNA) was achieved by maximizing the specific signal while minimizing nonspecific background noise, enabling reliable detection of target DNA down to 200 fM. Collectively, all these works highlight tetrahedral DNA frameworks as a powerful tool for interfacial engineering. Tetrahedral DNA frameworks overcome the fundamental limitation of conventional probe immobilization by programming DNA conformation at the nanoscale, providing a general and effective framework for constructing biosensors with exceptional speed, specificity, and sensitivity.

Collectively, the orientation of bioreceptors on nanoparticles is critical to accessibility of analytes to bioreceptors, which directly determines the sensitivity, LOD, signal-to-noise ratio and response time of biosensors. A range of approaches have been illustrated to regulate the orientation of bioreceptors on nanoparticles for superior sensing performance, listed in Table 1. The approaches to modulate the orientation of antibody are classified into pH regulation, affinity tags, genetically engineered antibody and antibody-directed synthesis of nanomaterials. pH regulation is straightforward to perform; however, it may not be applicable for all antibodies as it depends on the protonation/deprotonation of amino acid residues. Meanwhile,

Table 1 Enhanced sensing performance of nanoparticle-based biosensors by tailoring orientation of bioreceptors

Surface-bioreceptor	Tailoring approach	Analyte	Signal strategy	Enhanced sensing performance	Ref.
AuNPs–antibody	pH	HRP	Abs.	2-fold increase in the percentage of active antibody	67
Gold–antibody	Thiol groups	GRe	Optical	1500–4000-fold improved sensitivity; LOD: decrease from 0.5 ng mL^{-1} to 1 pg mL^{-1}	71, 73 and 74
YSSNs–antibody	Carbohydrate moiety	MMP-9	OD	Linear range: 0.1–20 ng mL^{-1} (OD mode) and 0.01–1000 ng mL^{-1} (SERS mode) for YSSN-MPBA-LFIA; 5–200 ng mL^{-1} for AuNP-LFIA (OD mode)	75
			SERS	LOD: 0.041 ng mL^{-1} (OD mode) and 0.012 ng mL^{-1} (SERS mode) for YSSN-MPBA-LFIA; 1.71 ng mL^{-1} for AuNP-LFIA (OD mode)	
Microsphere-antibody	Protein A	Enrofloxacin	FL	Linear range: 0.25–10 ng mL^{-1} for an oriented probe; 0.1–2.5 ng mL^{-1} for a non-oriented probe LOD: 0.035 ng mL^{-1} for an oriented probe and 0.079 ng mL^{-1} for a non-oriented probe	78
Polystyrene surface-antibody	Avidin–biotin	cTnI	Abs.	20-fold higher detection capability; LOD: decrease from 2.65 ng mL^{-1} to 0.13 ng mL^{-1}	80
Polystyrene sphere-antibody	SpyTag-SpyCatcher	DENV NS1	FL	Signal-to-noise ratio: 5-fold increase; LOD: decrease from 0.32 ng mL^{-1} to 0.064 ng mL^{-1}	86
Quantum bead-nanobody	SpyTag-SpyCatcher	Human chorionic gonadotropin	FL	LOD: 5.1 pg mL^{-1} Sensitivity: 6-fold improvement compared to the randomly oriented antibodies	87
PLA–PEG NPs–antibody	Monobody adopter	Vascular endothelial cells	FL	>1000-fold improvement in binding efficiency	88
MOF-antibody containing QDs	Ab-directed synthesis	SKOV-3 cells	FL	Fully preserved targeting efficiency	93
ZIF-8–antibody	Ab-directed synthesis	Cortisol	Current	Linear range:1 pg mL^{-1} to 1 μg mL^{-1} LOD: 0.26 pg mL^{-1} and good storage stability	95
AuNCs–antibody	Ab-directed synthesis	Goat anti-human IgG	FL	Excellent sensitivity Good storage stability	96
AuNPs–DNA	Spacer	DNA	Abs.	Hybridization efficiency increased from 5% to 90%; 5-fold faster in aggregate time	107
AuNPs–DNA	Backfilling	DNA	FL	Sensitivity: 2-fold improvement	114
DNA framework-DNA	DNA framework	miRNA-141, thrombin, ATP	Current	Hundred times higher sensitivity and signal-to-noise ratio	120
DNA framework-DNA	DNA framework	DNA	Current	Higher hybridization efficiency and LOD:1 fM; response time: 2 times faster than other sensors	121
DNA framework-DNA	DNA framework	DNA	Current	Rate constant: 10.16 min^{-1} for tetrahedral DNA framework-ssDNA *vs.* 0.01 min^{-1} for ssDNA K_d: 18.12 nM for tetrahedral DNA framework-ssDNA *vs.* 55.11 nM for ssDNA Signal-to-noise ratio: 214 for tetrahedral DNA framework immobilized ssDNA *vs.* 17 for ssDNA	122

Notes: FL represents the fluorescence signal.

pH can affect both antibody activity and colloidal stability of nanoparticles.[123] Genetic modification of antibodies based on protein engineering requires detailed knowledge of protein structure, high cost and long preparation time.[124] The strategy of antibody-directed synthesis remains nascent with limited types of nanomaterials. Compared with antibodies, DNA is much easier to synthesize chemically with tailored functional groups. Strategies to orientate DNA in upright and extended conformation include incorporating spacers, backfilling, freezing or tetrahedral DNA framework-direct alignment. Except for approaches described above, applying electric field is also a promising approach to modulate the orientation of bioreceptors.[125] Kim's group applied an electric field to align the antibody orientation on planar surfaces.[126] The impedance change was maximized when antibodies were directionally aligned. The sensitivity enhancements from aligning the Fab and Fc regions were reported to be 1.31- and 1.60-fold in phosphate-buffered saline (PBS) and 1.41- and 2.18-fold in plasma, respectively. Similarly, Ye *et al.* found that the DNA conformation was sensitive to the applied electric field on planar gold. DNA tends to coil around the edge of large defects under positive potential, whereas it is lifted out of defects under negative potentials.[127] However, there is no study of tailoring orientation of antibodies or DNA on nanoparticle surfaces *via* electric field yet. Given its cost-effectiveness, scalability, and ease of integration with chemical and biological modification strategies, substantial opportunities remain for exploiting electric fields to control the orientation of bioreceptors on nanoparticles.

3.2. Coverage of bioreceptors

3.2.1. Optimal coverage of bioreceptors. The most prevalent question regarding coverage is what is the optimal coverage of a bioreceptor on nanoparticles for the best analytical performance? To optimize the coverage of bioreceptors, it is essential to control and quantify the amount of bioreceptors on nanoparticles. The typical approaches to tailor the coverage of bioreceptors include varying the ratio of bioreceptors and nanoparticles, adding other ligands to form a mixed layer or changing the ionic strength of the immobilization buffer.[128,129] Normally, the ratios of added bioreceptors to nanoparticles are many hundreds to ensure excess bioreceptors per nanoparticle in most affinity biosensors. The impact of antibody coverage on capturing activity and binding kinetics was investigated by Prins.[130] As shown in Fig. 7a, antibody1 functionalized MNPs firstly captured anti-cardiac troponin I (cTnI) and then moved towards an antibody2 immobilized surface under an applied magnetic field. Finally, the surface-bound MNPs were optically detected by scattering and absorption of an evanescent optical field. For MNPs with low antibody coverage, there are many randomly oriented antibodies with low affinity or without affinity to antigens. With the increase of antibody coverage, the number of oriented and unoriented antibodies both increases. The number of active antibodies initially increased and then saturated. As a result, MNPs with a higher number of antibodies possessed faster kinetics than MNPs with a smaller number of antibodies (Fig. 7b). The MNPs with 15 × 10^2 antibodies reached a steady state in about 50 min, whereas the MNPs with 236 × 10^2 antibodies took only 20 min. The immunoassay response scaled with the increasing number of antibodies. The sensitivity of MNPs with 236 × 10^2 antibodies was 5 times higher than that of MNPs with 15 × 10^2 antibodies. The optimal sensing performance in terms of sensitivity and kinetics is achieved with the highest coverage of antibodies. The Gooding group also studied the impact of aptamer coverage on AuNPs on the binding equilibrium and kinetics between the aptamer and the target protein.[131] It was found that the AuNPs–aptamer conjugate with the highest coverage of the aptamer is the most favorable in biosensors considering LOD, sensitivity and response time. In a more recent report, the Jiang group modulated the surface ligand of AuNPs from strongly ionized citrate to weakly ionized ascorbic acid to engineer nano–bio interfaces for ultrasensitive point-of-care sensors (Fig. 7c).[132] AuNPs stabilized by citrate (Cit-AuNPs) form a dense and highly negative electrostatic layer that strongly repels antibodies. In contrast, the weakly ionized ascorbic acid–AuNPs (AA-AuNPs) with a looser electrostatic interface minimize the charge repulsion and allow for efficient Ab conjugation at neutral pH. Consequently, approximately 2-fold more antibodies adsorb onto AA–AuNPs than that onto Cit-AuNPs. Molecular dynamics (MD) simulations further indicate that antibodies bind to AA-AuNPs primarily *via* their heavy chains (H-chains), thereby preserving the antigen-binding domains. By comparison, antibodies on Cit-AuNPs interact *via* both heavy and light chains, potentially compromising their activity (Fig. 7d). Due to the simultaneously enhanced antibody coverage and improved bioactivity, AA-AuNPs-based LFAs achieve detection limits in the pg mL^{-1} range for biomarkers such as α-fetoprotein (Fig. 7e), C-reactive protein, and procalcitonin, representing a 100-fold enhancement in sensitivity relative to Cit-AuNPs LFAs. The time-related stability tests exhibit a variable coefficient below 6%, indicating good stability of AA-AuNPs-based LFIA after 6 months of storage. This work highlights rational surface design of nanoparticles as a powerful and versatile tool to control

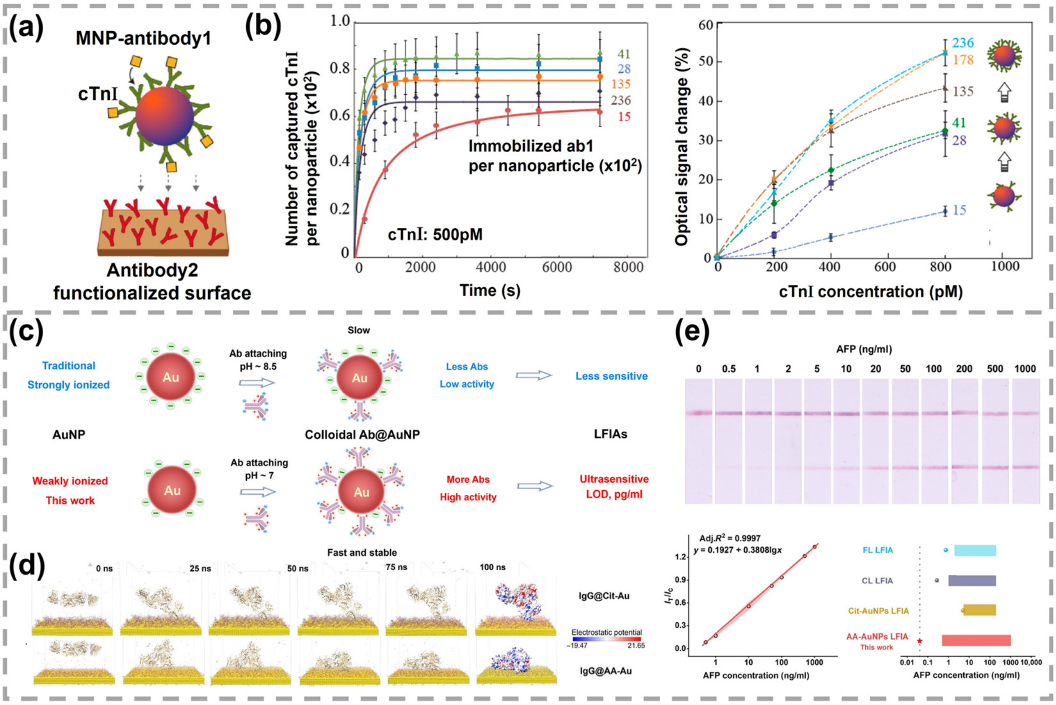

Fig. 7 (a) Detection principle of the optomagnetic immunoassay. (b) Response performances of MNPs with different antibody coverages. Reprinted with permission,[130] Copyright 2014, American Chemical Society. (c) Schematic illustration of the strong and weakly ionized AuNPs for ultrasensitive LFIAs. (d) The snapshots of IgG on Cit-Au and AA-Au surfaces at different simulation times. (e) Testing strips of AA-AuNPs LFIAs responding to α-fetoprotein with different concentrations and the correlated linear fitting curve. Reprinted with permission,[132] Copyright 2024, American Association for the Advancement of Science.

nano–bio interfaces, enabling the development of ultrasensitive, simple and cost-effective point-of-care sensors.

Regarding the optimal coverage of bioreceptors, other groups investigated the effect of bioreceptor coverage on the enhanced sensing performance and obtained the opposite conclusion. The Fan group studied how DNA coverage on AuNPs affected the sensing performance of a stochastic DNA walker and found that loosely packed SNA gave the lowest LOD.[133] In Fig. 8a, an exonuclease III (Exo III)-powered stochastic DNA walker autonomously move on a SNA-based 3D track. The driving force is derived from the unidirectional digestion of DNA tracks with Exo III. As DNA tracks on AuNPs were tagged with FAM, the digestion of DNA tracks led to FAM release and a corresponding increase in fluorescence intensity. The amount of DNA on AuNPs was regulated *via* ionic strengths of immobilization buffer.[33,134] The low, medium, and high densities of DNA on 15 nm AuNPs were 25, 56, and 100 DNA per AuNP, respectively. LODs were 10 fM, 1 pM, and 200 pM for AuNPs–DNA conjugates with coverages of 25, 56, and 100 DNA per particle. Similarly, Liang *et al.* investigated the impact of DNA coverage on an enzyme-assisted target recycling assay to detect DNA *via* colorimetric assay.[113] In the presence of target DNA, Exo III rapidly cleaved hybridized probes from AuNPs and induced the nanoparticle aggregation. The colour of AuNP solution changed from red into purple and even blue. AuNPs–DNA conjugates with low (30 strands per NP), medium (43 strands per NP), and high (54 strands per NP) coverage of DNA were prepared by adding different amounts of dithiothreitol. The LODs of low, medium, and high DNA covered AuNPs were 100 nM (red to purple), 250 nM (red to blue) and 50 nM (red to blue), respectively. Meanwhile, the decrease in DNA coverage also markedly shortened the response time. Specifically, AuNPs–DNA conjugates with 53 and 29 strands per NP changed into purple colour after 17 and 6 min, respectively. Overall, AuNPs with lower surface coverage imparted shorter response time and lower LOD in the above studies.

The Zako group performed a comprehensive investigation into the critical role of probe DNA density in the performance of AuNPs–DNA conjugate-based colorimetric biosensors. Consistent experimental condition was employed in their series of

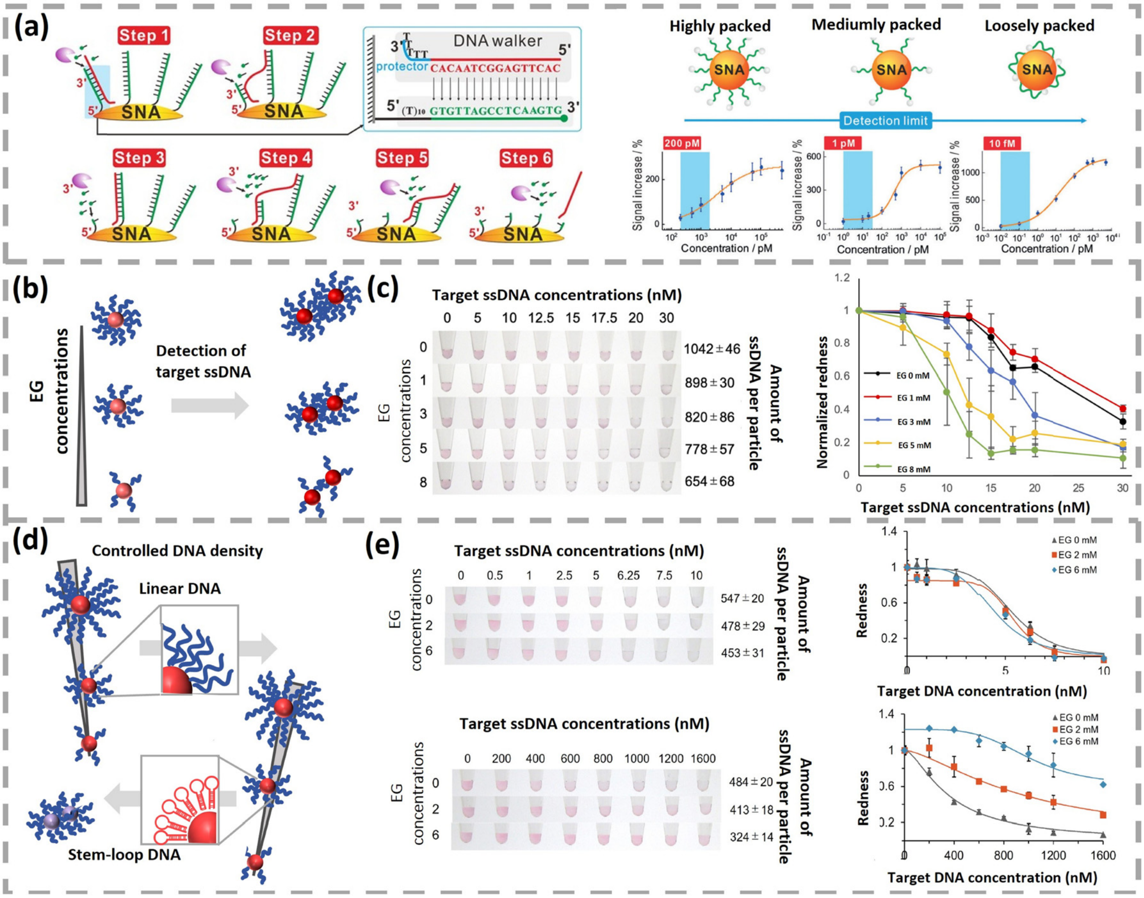

Fig. 8 (a) Schematics of Exo III-powered stochastic DNA walkers on SNA and response curves of AuNPs–DNA conjugates with different amounts of DNA. Reproduced with permission,[133] Copyright 2017 Wiley-VCH. (b) Schematic illustration of AuNPs–DNA conjugate based colorimetric biosensors with controlled amounts of ssDNA. (c) Images (middle) and normalized redness values (right) of AuNP solutions with different densities of DNA. Reproduced with permission,[135] Copyright 2023 The Royal Society of Chemistry. (d) Effect of probe DNA density on sensing performances for DNA with two different structures. (e) Representative images and redness values of AuNP solutions functionalized with different amounts of immobilized ssDNA, with linear DNA on top and stem-loop DNA on bottom. Reproduced with permission,[137] Copyright 2025 Springer Nature.

studies: 40 nm AuNPs–ssDNA conjugates were prepared *via* a freeze–thaw method, with various concentrations of ethylene glycol (EG) added to control the density of ssDNA. The colour of AuNP solution transited from red to blue/purple, quantified using redness value from digital image analysis and/or UV-vis spectroscopy (OD_{530}/OD_{630}). The effect of linear ssDNA probe density in salt-induced non-crosslinking aggregation was initially investigated (Fig. 8b).[135] As AuNPs–ssDNA conjugates possessed superior dispersion stability against salts compared to AuNPs–dsDNA conjugates, increasing the amount of target ssDNA caused the colour of AuNP–DNA solution to change from red to blue/transparent. When the amount of ssDNA per AuNP increased from 654 to 1042, the detection sensitivity significantly decreased, confirmed by the normalized redness value of solutions (Fig. 8c). The LODs of AuNPs–ssDNA conjugates with 654 and 1042 ssDNA per AuNP were 17.5 nM and 10 nM, respectively. Subsequently, this sensing strategy was extended to the crosslinking aggregation, in which target DNA hybridized with two different AuNPs–ssDNA conjugates and induced the aggregation of AuNPs.[136] Both the colour change and varying OD_{530}/OD_{630} ratios indicated that sensitivity increased as the density of immobilized ssDNA decreased. This trend was ascribed to the alleviated electrostatic repulsion and steric hindrance at low probe density, leading to the improved hybridization efficiency. They further extended the work to explore the interplay between density and the secondary structure of probe DNA in non-crosslinking aggregation assay (Fig. 8d).[137] Notably, the benefit of low probe density is structure-dependent: low probe density enhanced the sensitivity for linear probes, but decreased the sensitivity for stem-loop and G-quadruplex probes, as their stable secondary structures hindered the target hybridization (Fig. 8e). The above nanoparticle-based DNA biosensors highlight that both the sensing strategy and the configuration of probe DNA are key determinants when optimizing the coverage of DNA on nanoparticles.

3.2.2. Monovalent nanoparticles. Instead of nanoparticles modified with many bioreceptors, nanoparticles with a small and defined number of bioreceptors have gained significant attention.[138] Nanoparticles with a controlled number of bioreceptors (valence) can not only serve as building blocks for nanoparticle-assembly and complex nanoarchitecture but are also critical sensing units in biosensors.[139,140] Especially, monovalent nanoparticles ensure interaction between single bioreceptors and analytes, which provides valuable information at the single molecule level.[141] However, controlling the number of bioreceptors on a nanoparticle remains challenging, particularly preparing uniform monovalent nanoparticles. A common strategy involves functionalizing nanoparticles with a limited number of bioreceptors, resulting in a mixture of particles with varying valences. Then nanoparticles with mixed valences are fractionated into discrete conjugates with a certain number of bioreceptors using gel electrophoresis, high-performance liquid chromatography (HPLC), size exclusion chromatography and affinity chromatography (Fig. 9a).[142–145] Li *et al.* fabricated a reversible single aptamer-Au plasmon ruler for single molecule detection of secreted recombinant mouse matrix metalloproteinase 3 (MMP3).[146] The MMP3 aptamer was functionalized with a thiol group at one end and a biotin group at the other end (Fig. 9b). AuNPs modified with an MMP3 aptamer and mixed ligands (HS-PEG-OH and HS-PEG-COOH) were purified using HPLC to obtain monomeric aptamer–AuNPs. In parallel, avidin-AuNPs were prepared by reacting AuNPs with the mixed ligands

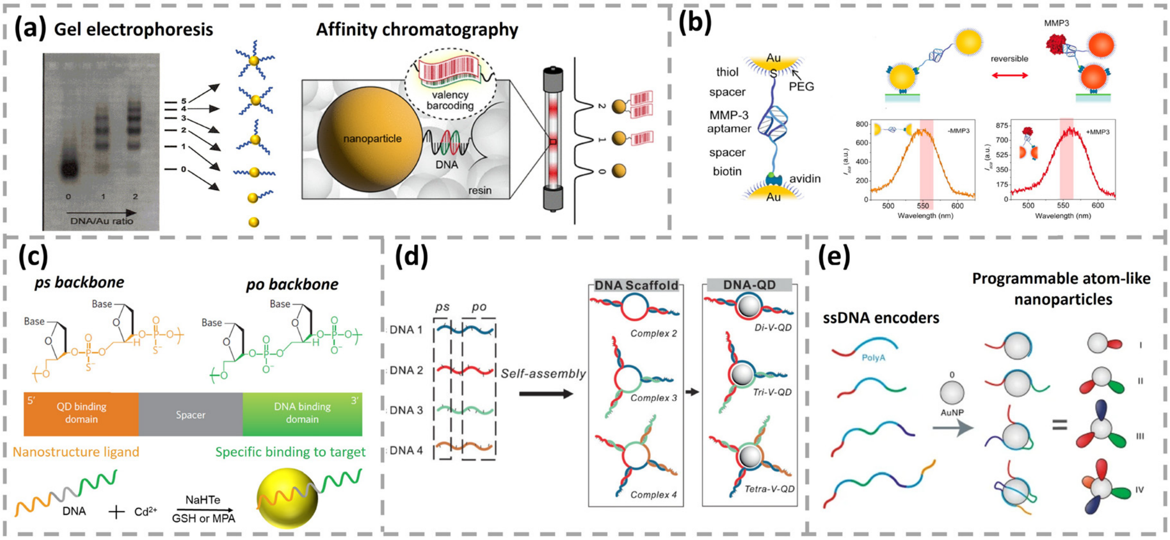

Fig. 9 (a) DNA valency sorting by gel electrophoresis and affinity chromatography. Reproduced with permission,[144,145] Copyright 2022 and 2001, American Chemical Society. (b) Structure of a plasmon ruler composed of two AuNPs linked by an MMP3 aptamer. The plasmonic resonance wavelength of an aptamer-Au plasmon ruler in the presence and absence of MMP3. Reproduced with permission,[146] Copyright 2015, American Chemical Society. (c) One-pot synthesis of chimeric DNA-functionalized QDs. Chimeric DNA includes a ligand domain (ps, in orange) and a recognition domain (po, in green). Reproduced with permission,[147] Copyright 2008, Springer Nature. (d) DNA scaffolds self-assembled from the different sets of chimeric DNAs for valence-engineered QDs. Reproduced with permission,[150] Copyright 2017, Wiley-VCH. (e) Programmable atom-like nanoparticles prepared with ssDNA encoders containing polyA. Reproduced with permission,[151] Copyright 2019, Springer Nature.

of biotin-PEG-OH and HS-PEG-COOH. The monomeric aptamer-AuNPs and avidin-AuNPs were then assembled into AuNP dimers based on avidin–biotin interaction. Once the secreted MMP3 bound with the aptamer, the interparticle distance decreased, leading to a pronounced spectral redshift observed in dark-field microscopy. This aptamer-Au plasmon ruler can detect single secreted MMP3 in mammary epithelial cells with outstanding reversibility and high specificity.

Modified DNA with specific sequences can be utilized to obtain valence-controlled nanoparticles. For instance, a chimeric DNA containing two moieties, phosphorothioates (ps) and phosphodiester (po) backbone, has been utilized to prepare monovalent QDs (Fig. 9c).[147] Since metal ions of QDs (*e.g.* Cd^{2+} and Zn^{2+}) exhibit thousand-fold higher affinity for sulfur than that for oxygen, domains with the ps backbone direct the passivation of nanocrystals while domains with the po backbone mediate biorecognition.[148] The number of ps oligomers can be regulated to obtain QDs with a range of valences. Compared with all po DNA, a significant increase in target binding efficiency was observed for the ps–po oligonucleotide. He and colleagues further assembled multi-color ps–po DNA-QDs to construct a QD-based computing system. Seven fundamental logic gates (AND, OR, NOR, NAND, INH, XNOR, and XOR) were achieved using binary and ternary QD complexes based on DNA strand displacement reactions.[149] Beyond monovalent QDs prepared with ps–po DNA, multiple ps–po DNAs could be firstly assembled into programmable scaffolds and then employed to fabricate bivalent or multivalent QDs (Fig. 9d).[150] More recently, the Fan group constructed AuNPs with a controlled valence bond using ssDNA containing polyA as an encoder (Fig. 9e).[151,152] Atom-like nanoparticles with programmable *n*-valence were obtained by regulating the order, length and sequence of each encoder with alternating polyA/non-polyA domains. Subsequently, AuNPs with a precisely programmable bond length and bond energy were successfully fabricated using polyA-based encoders.[153] In summary, nanoparticles with defined DNA valency can be assembled into complex nanostructures or used to implement Boolean logic operations, which have enormous potential in smart sensing applications.[154]

In summary, the coverage of bioreceptors on nanoparticles could influence sensitivity, LOD and response time of biosensors, with related examples in Table 2. The optimal coverage of bioreceptors depends largely on the configuration of bioreceptors and the adopted sensing strategy in the given biosensor. As for monovalent nanoparticles, delicate design of DNA sequences or modified nucleotide bases, such as DNA sequences containing ps–po oligonucleotides or polyA, enables precise control over DNA valency on QDs or AuNPs. The obtained programmable atom-like nanoparticles have shown great potential in nanoarchitecture assembly, distance-based energy transfer and intelligent biosensing.[155] Compared with various preparing strategies of nanoparticles with well-defined DNA valency, controlling the valence of antibody still depends on stoichiometric conjugation followed by purification.[142,156,157] Recently, Choi and colleagues developed a one-pot strategy to conjugate tandem repeat protein chains on AuNPs, enabling controlled valency without purification.[158] The specific designed proteins contain multiple and regularly spaced hexa-histidine tags, which can bind multivalently onto nanoparticles. However, controlling the number of antibodies per nanoparticle directly without purification and protein engineering remains challenging.

3.3. Composition of mixed ligands

3.3.1. Antifouling molecules. Introducing two or more types of molecules onto nanoparticles provides a broader range of potential properties for nano–bio conjugates.[159] As discussed in Section 3.1, backfilling agents are employed to preserve the proper conformation of DNA on AuNPs. In addition to backfilling agents, antifouling molecules are frequently incorporated into the recognition layer to reduce nonspecific adsorption of interfering species, thus improving both the sensing sensitivity and selectivity, which is particularly necessary for complex

Table 2 Enhanced sensing performance of nanoparticle-based biosensors by tailoring coverage of bioreceptors

Surface-bioreceptor	Tailoring approach	Analyte	Signal strategy	Enhanced sensing performance	Ref.
MNPs–antibody	Ratio of antibody/NPs	cTnI	Scattering Abs.	Sensitivity: 5-fold increase for high antibody coverage Response time: 2-fold faster for high antibody coverage	130
AuNPs–aptamer	Ratio of aptamer/diluent DNA	Interferon-gamma	FL	Sensitivity: 2 times increase for high aptamer coverage (256 *vs.* 9.6 aptamers/per AuNP) Response time: 4 times decrease (36 min *vs.* 137 min)	131
AuNPs–antibody	Ionic strength of the ligand	α-fetoprotein	OD	Lower LOD in the pg mL^{-1} range and good stability 100-fold enhancement in sensitivity	132
AuNPs–DNA	Ionic strength	DNA	FL	LOD: 200 pM, 1 pM, and 10 fM for AuNPs–DNA conjugates with 100, 56, and 25 strands per NP	133
AuNPs–DNA	Dithiothreitol amount	DNA	Abs.	LOD: 100 nM, 250 nM and 50 nM for AuNPs–DNA conjugates with 54, 43 and 30 strands per NP Response time: 17 and 6 min for AuNPs–DNA conjugates with 53 and 29 strands per NP, respectively	113
AuNPs–DNA	EG amount	DNA	Redness Value, OD	Increase in sensitivity for low DNA coverage LOD: 17.5 nM and 10 nM for AuNPs–DNA conjugates with 654 and 1042 strands per NP, respectively	135
AuNPs–aptamer	HPLC separation	MMP3	Plasmonic λ	Detect single MMP3 based on a plasmonic ruler	146
QDs–DNA	po–ps DNA	DNA	FL	Intelligent molecular diagnostics	149
AuNPs–DNA	PolyA	DNA	FL	Intelligent sensing	151

biological fluids.[160,161] Antifouling agents typically include PEG and its derivatives, zwitterionic ligands (carboxybetaine, sulfobetaine and phosphorylcholine) and peptides (glutamic or aspartic acid (E/D) and lysine (K)), as well as hydrophobic fluorinated coating.[162–167] When designing antifouling nano–bio interfaces, both the functionality of bioreceptors and properties of antifouling chemicals should be taken into account. Taking PEG as an example, a dense PEG layer with brush conformation is vital to reducing nonspecific adsorption. At low packing density, the distance between adjacent PEG exceeds their Flory radius, resulting in a mushroom-like conformation within a thin layer. While the packing density is elevated, the intermolecular spacing of PEG is smaller than the Flory radius, leading to the formation of a thick PEG layer with brush conformation. Apart from the packing density, the length of antifouling molecules also matters. The Chan group investigated the antifouling performance of PEG with different chain lengths. The PEG length should be shorter than that of the bioreceptor linker to ensure optimal target efficiency.[168] The Luo group has designed a series of antifouling peptides and implemented them in AuNP-based electrochemical biosensors. The designed peptides were initially monofunctional, serving only as antifouling agents for AuNPs modified with a mixed layer of both peptides and bioreceptors.[169,170] The introduction of these antifouling peptides enabled the electrode to exhibit strong resistance to interferences and maintained long-term antifouling performance—up to nearly 20 days in 20% serum. Beyond monofunctional design, his group further developed multifunctional isopeptides integrating an antifouling segment (cyclotide cyclo-C(EK)$_4$) with a carbohydrate-mimetic recognition motif for annexin A1 detection (Fig. 10a).[171] This multifunctional isopeptide immobilized onto AuNPs was deposited on a poly 3,4-ethylenedioxythiophene (PEDOT)/glassy carbon electrode. This nano–bio interface possessed excellent antifouling ability and resistance to proteinase hydrolysis stability, making it well suitable for clinical blood samples. More recently, the Luo group proposed a novel platinum–selenium (Pt–Se) interface as an alternative to the conventional Au–S interface to anchor multifunctional peptides for murine double minute 2 (MDM2) detection (Fig. 10b).[172] The corresponding calibration curves of

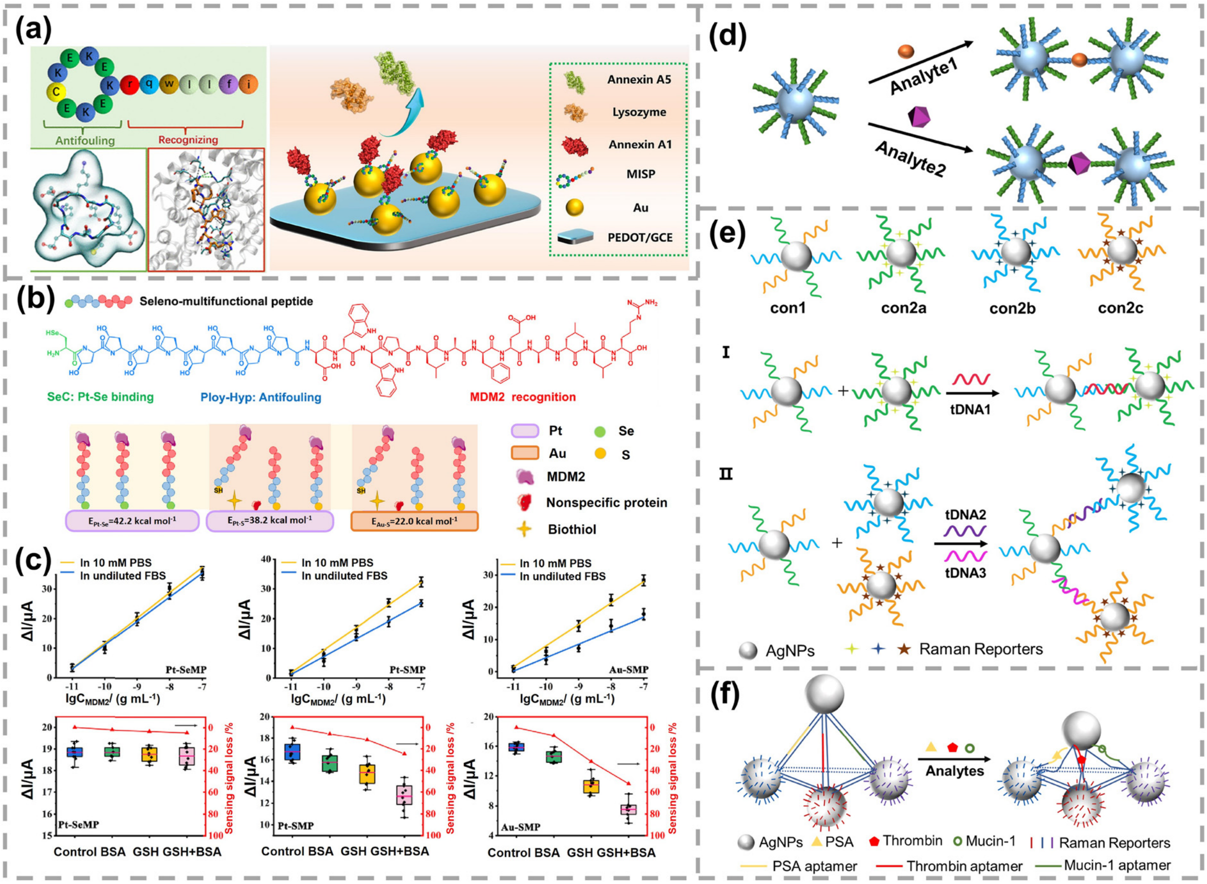

Fig. 10 (a) Schematic diagram of a multifunctional isopeptide based electrochemical biosensor for annexin A1 detection. MISP represents the multifunctional isopeptide. Reproduced with permission,[171] Copyright 2023, American Chemical Society. (b) Chemical structure of the designed multifunctional peptide for MDM2 detection. (c) Schematic representation of Pt–Se, Au–S, and Pt–S interfaces and their sensing performances. Reproduced with permission,[172] Copyright 2024, American Chemical Society. (d) Utilization of mixed ligands for detecting multiple analytes based on nanoparticle aggregation. Reproduced with permission,[159] Copyright 2020, American Chemical Society. (e) The principle of a SERS-based sandwich assay for one (i) and two (ii) target DNA detection. Reproduced with permission,[173] Copyright 2011, The Royal Society of Chemistry. (f) SERS encoded Ag-pyramidal detection of multiple biomarkers. Reproduced with permission,[174] Copyright 2015, Wiley-VCH.

Pt–Se, Pt–S and Au–S interfaces for MDM2 detection are presented in Fig. 10c. Regarding the Pt–Se interface, the linear range and LOD almost unchanged from PBS to undiluted fetal bovine serum (FBS). As for the Au–S and Pt–S interfaces, the substantial decrease in the signal intensity of undiluted FBS indicates lower detection sensitivity. The sensing responses to 1.0 ng mL^{-1} MDM2 in the control and in the presence of bovine serum albumin (BSA), glutathione (GSH) and the mixture of BSA and GSH were also investigated. The Pt–Se interfaces possess stronger binding energy and improved resistance to both biothiols and nonspecific protein. Additionally, the reproducibility of this built electrochemical sensor was assessed with multiple tests using a single biosensor or independently prepared biosensors. The relative standard deviation of eleven scans from one biosensor was only 0.15% and the relative standard deviation of eleven different biosensors was 3.47%, demonstrating that Pt–Se interfaces exhibited reliable performance across inter-batch and intra-batch measurements. Compared with analogous Au–S and Pt–S interfaces, Pt–Se interfaces demonstrated superior sensitivity, satisfactory reproducibility and improved antifouling performance in real serum.

3.3.2. Mixed bioreceptor layer for multiplex detection. Nanoparticles functionalized with multiple bioreceptors enable multiplexed detection. More than one type of bioreceptor---each specific to a distinct target—could be conjugated onto nanoparticles and form a mixed-ligand layer. Such multifunctional nanoparticles are suitable for rapid screening a range of targets but without capability to distinguish each analyte, shown in Fig. 10d.[159] To achieve the multiple detection of each analyte, SERS is an ideal solution because of its fingerprint-like spectral signatures provided by a Raman reporter. The Song group prepared mixed DNA functionalized silver nanoparticles (AgNPs) for SERS-based multiplex DNA detection (Fig. 10e).[173] Three probe DNAs were modified on AgNPs with equal molar ratios (con1). Three detection DNAs and three Raman reporters (4-aminothiophenol (4-ATP), 6-mercaptonicotinic acid and 2-mercaptopyrimidine) were grafted on AgNPs, named con2a, con 2b, and con 2c, respectively. Target DNAs (tDNA1, tDNA2 and tDNA3) were hybridized with probes and detection DNAs, resulting in the aggregation of AgNPs and the enhanced Raman signals. Hence, by selectively switching on characteristic Raman peaks, a barcode-like diagram was generated to visualize spectral differences of distinct one-, two-, and three-target DNA detection. Moreover, multiplex detection can be achieved by assembling nanoparticles functionalized with different bioreceptors. For instance, Xu *et al.* assembled four AgNPs into pyramids with dsDNA as a scaffold to detect multiple biomarkers at the attomolar level.[174] In Fig. 10f, aptamers for prostate specific antigen (PSA), thrombin and mucin-1 were inserted in each side of the DNA pyramid. Three AgNPs at the bottom of pyramid were modified with different Raman reporters, including 4-ATP, 4-nitrothiophenol, and 4-methoxybenzyl mercaptan, respectively. Multiple biomarkers can be detected based on unique Raman spectral signatures. Compared with uncontrolled aggregates in solutions, formation of pyramids consisting of four AgNPs provides a more controlled architecture, improving both sensitivity and reproducibility of detection.

3.3.3. Cooperative effect of multiple functional components. The attachment of multiple functional components onto nanoparticles can generate cooperative effects that significantly enhance the sensitivity of nanoparticle-based biosensors. As for bio-barcode assay developed by Hill and Mirkin, AuNPs are functionalized with a mixed layer of antibodies and DNA strands, where the antibodies act as recognition elements and hundreds of ssDNA work as barcodes (Fig. 11a).[175] MNPs are modified with a secondary antibody to capture antigens. Upon target binding, AuNPs and MNPs form an antibody–antigen–antibody sandwich complex, which was subsequently isolated

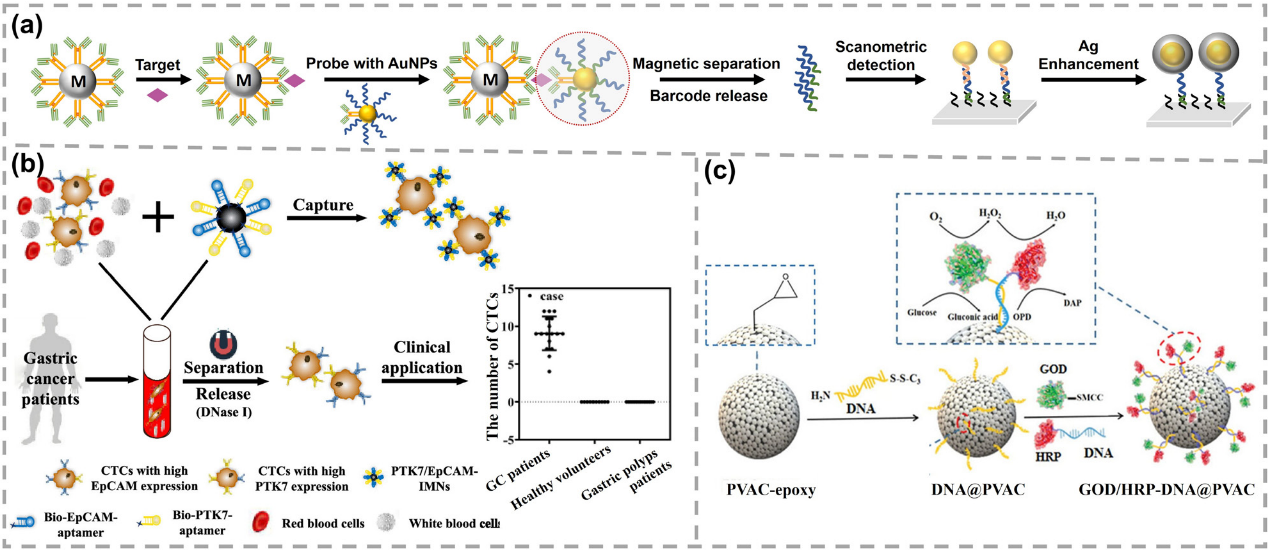

Fig. 11 (a) Schematic representation of antigen detection using the bio-barcode assay. Reproduced with permission,[175] Copyright 2006, Springer Nature. (b) Preparation of dual aptamer-modified Fe_3O_4 MNPs and clinical applications. Reproduced with permission,[178] Copyright 2022, American Chemical Society. (c) Schematic diagram of GOD/HRP-DNA@MMS. Reproduced with permission,[180] Copyright 2023, Wiley-VCH.

under a magnetic field. Afterwards, the barcode DNA strands were then released by treatment with dithiothreitol and identified on a microassay chip through scanometric detection. A similar DNA-based biosensor was built by replacing the recognition antibodies on AuNPs with DNA strands. In both designs, the bioreceptor and barcode DNA operated in concert to achieve extraordinary detection sensitivity, comparable to that of polymerase chain reaction. Meanwhile, an aptamer-based dual recognition strategy, using dual aptamers or the combination of aptamers with other recognition elements, is also widely applied in nanoparticle-based biosensors to address the growing demands of precision diagnosis and medicine.[176,177] For instance, Li *et al.* conjugated both the epithelial cell adhesion molecule (EpCAM) and protein tyrosine kinase 7 (PTK7) aptamers onto Fe_3O_4 NPs for precise capture of circulating tumor cells (CTCs) in gastric cancer (Fig. 11b).[178] This nano–bio conjugate effectively captured heterogeneous CTCs, including both $EpCAM^+$ and $PTK7^+$ subtypes. Such an approach overcomes the inherent limitations of single-marker strategies, which fail to recognize EpCAM-negative CTCs. The dual-aptamer strategy exhibited satisfactory CTC capture efficiency and enabled effective downstream analysis for gastric cancer patients. Clinical validation with 72 patient samples revealed strong correlations between CTC numbers and chemotherapy cycles, as well as CTC numbers and the different stages of gastric cancer.

Nanoparticles can serve as versatile platforms for the co-immobilization or encapsulation of multiple enzymes, enabling their cooperative operation in cascade reactions. Yang's group developed polyphenol-encapsulated enzyme–DNA conjugates on $SiO_2@Fe_3O_4$ magnetic microspheres (MMSs) with different enzymes confined within separate compartments.[179] Two model enzymes, glucose oxidase (GOx) and HRP, were precisely immobilized on opposing hemispheres of MMS. This system exhibited a Michaelis constant (K_m) of 1.19 mM, which was lower than those of randomly immobilized (1.47 mM) and free enzymes (3.45 mM), indicating the enhanced substrate affinity. Moreover, its catalytic efficiency (k_{cat}/K_m) was 5.32×10^{-8} s^{-1} mM^{-1}, significantly higher than that of randomly immobilized enzymes ($4.01\ s^{-1}\ mM^{-1}$) and free enzymes ($0.41\ s^{-1}\ mM^{-1}$), highlighting the enhanced performance afforded by spatial organization. In a more refined design, GOx and HRP were co-immobilized on epoxy modified polyvinyl acetate (PVAC) MMSs utilizing Y-shaped DNA scaffolds assembled from two partially complementary ssDNA (Fig. 11c).[180] The cascade activity was strongly dependent on the inter-enzyme distance, which could be precisely adjusted by varying the length of the DNA strand. Maximum activity ($0.97\ U\ \mu g^{-1}$) was achieved at an optimal spacing of 13.6 nm, 3.5-fold enhancement compared with that of free enzymes. The maximum reaction rate of GOD/HRP-DNA@MMS ($0.97\ U\ \mu g^{-1}$) exceeded that of free enzymes ($0.28\ U\ \mu g^{-1}$), while its K_m ($9.04\ mg\ mL^{-1}$) was lower than that of the free system ($14.71\ mg\ mL^{-1}$), reflecting higher apparent cascade activity. The turnover number (k_{cat}) of $385.6\ min^{-1}$ further demonstrated the exceptional catalytic efficiency of this spatially organized enzyme system. Beyond post-synthetic immobilization, multi-enzyme systems have also been co-encapsulated within MOFs for intracellular lactate detection, achieving a 650-fold signal-to-noise ratio higher than that of conventional approaches.[181] Moreover, multi-shelled MOFs provide a hierarchical scaffold for the spatial organization of enzymes at the nanoscale, leading to substantial enhancements in catalytic efficiency. For example, a GOx-HRP cascade encapsulated in multi-shelled ZIF-8 showed a 5.8- to 13.5-fold increase in catalytic efficiency compared to free enzymes in solution.[182]

Collectively, the composition of mixed ligands on nanoparticles affects the specificity, sensitivity, stability, and multiplexing capacity of biosensors (Table 3). The integration of antifouling agents into nano–bio interfaces can significantly enhance the specificity, sensitivity and operational stability of biosensors. More importantly, the antifouling molecules enable the nanoparticle-based biosensor to operate reliably in complex samples with matrix effects, such as human serum and whole blood, with satisfactory accuracy. Furthermore, nanoparticles co-functionalized with multiple bioreceptors and Raman reporters can serve as ideal platforms for multiplexed detection.

Table 3 Enhanced sensing performance of nanoparticle-based biosensors by tailoring the composition of mixed ligands

Surface-bioreceptor	Tailoring approach	Analyte	Signal strategy	Enhanced sensing performance	Ref
AuNPs–aptamer	Antifouling peptide	Cancer antigen125	Current	Antifouling performance can last 1–2 days; applicable to clinical serum samples	169
AuNPs–peptide	Multifunctional peptide	Annexin A1	Current	LOD: $0.43\ pg\ mL^{-1}$ in 50% human blood; applicable to clinical blood samples	171
PtNPs–peptide	Multifunctional peptide	MDM2	Current	Linear range and LOD unchanged from PBS to undiluted serum Satisfactory specificity and reproducibility	172
AgNPs–aptamer	Multiple aptamer	PSA, Mucin-1, Thrombin	SERS	Multiplex detection and rapid response	174
AuNPs–antibody	Antibody and DNA	Protein	Optical	Sensitivity comparable with PCR	175
Fe_3O_4 NPs–aptamer	Dual aptamer	CTCs	FL	Capture heterogeneous CTCs, including $EpCAM^+$ and $PTK7^+$ subtypes Clinical validation with 72 patient samples	178
MNPs–enzyme	GOx and HRP	Cascade activity	Abs.	3.5-fold enhanced activity compared with those of free enzymes Reaction rate: $0.97\ U\ \mu g^{-1}$ for GOD/HRP-DNA@MMS and $0.28\ U\ \mu g^{-1}$ for free enzymes K_m value: $9.04\ mg\ mL^{-1}$ for GOD/HRP-DNA@MMS and $14.71\ mg\ mL^{-1}$ for free enzymes	180

By developing additional Raman reporters with distinct characteristic peaks, the number of detectable analytes can be expanded from a few to several tens. Lastly, mixed bioreceptor layers, such as combinations of antibodies and DNA and dual-aptamer or multi-enzyme systems, can act cooperatively to enhance the sensitivity and precision of detection.

3.4. Spatial distribution of bioreceptors

3.4.1. Regioselective biomodification based on surface accessibility. The spatial distribution of bioreceptors on nanoparticles plays an important role in determining the overall sensing performances of biosensors. Anisotropic nanoparticles can be exploited to prepare site-selective bifunctional nanoparticles as those nanoparticles terminate in distinct crystal facets with varying binding energies or distinct functional regions. Taking AuNRs as an example, cetyltriethylammonium bromide (CTAB) preferentially binds the {100} facet on the side of AuNRs, while the thiolated molecule conversely binds the {111} facet on the end of AuNRs.[183,184] Noticeably, the edges and tips of anisotropic nanoparticles, known as hot spots, usually serve as signal amplifiers to improve analytical sensitivity.[185] The Gooding group systematically compared the plasmonic hot-spots formed by gold nanobipyramids and AuNRs and their SERS performances.[186] The hot spots located at tips of individual particles or in nanometer-scale gaps between end-to-end assembled particles were investigated. It was demonstrated that both individual and assembled gold nanobipyramids exhibited significantly higher enhancement factors than their nanorod counterparts. Particularly, the well-defined hot spot formed between assembled nanobipyramids yielded an SERS enhancement factor on the order of 10^7, which was two orders of magnitude higher than those of individual nanobipyramids and roughly an order of magnitude greater than assembled nanorods, approaching the sensitivity required for single-molecule detection. Subsequently, they rationally designed regioselectively functionalized AuNRs as an SERS probe (Fig. 12a).[187] Antibodies and protein resistant layers ((1-mercaptoundec-11-yl) dodeca(ethylene glycol) (OEG_{12}) and monocarbox(1-mercaptoundec-11-yl) penta-(ethylene glycol) (OEG_5)) were modified on the side of AuNRs, while a Raman reporter, 4-mercaptobenzoic acid, was attached to the tip of AuNRs. This sophisticated surface design ensures comprehensive performance in terms of biorecognition activity, antifouling capability and colloidal stability of AuNRs, allowing single molecule detection of *Salmonella* bacteria in complex food matrices prepared by chicken meat, baby spinach and lettuce. Additionally, regioselectively functionalized anisotropic Au nanoparticles can also serve as building blocks for nanoparticle assemblies. By controlling the addition order of DNAs with a predetermined ratio, two distinct DNA strands could be selectively attached onto either the ends or the sides of AuNRs.[188] Three types of AuNP-AuNR assemblies, denoted as end, side, and satellite assemblies, were constructed with 4-ATP as a Raman reporter based on this regioselective modification strategy (Fig. 12b).[184] The SERS intensities of these three assemblies all increased significantly compared with non-assembled AuNPs (Fig. 12c). *In vivo* data indicated that those assembled AuNPs could be utilized as label-free intracellular probes to acquire real-time information of local metabolic processes with high sensitivity, especially for low molecular weight metabolites such as lipids in HeLa cells. The precise spatial control of bioreceptor

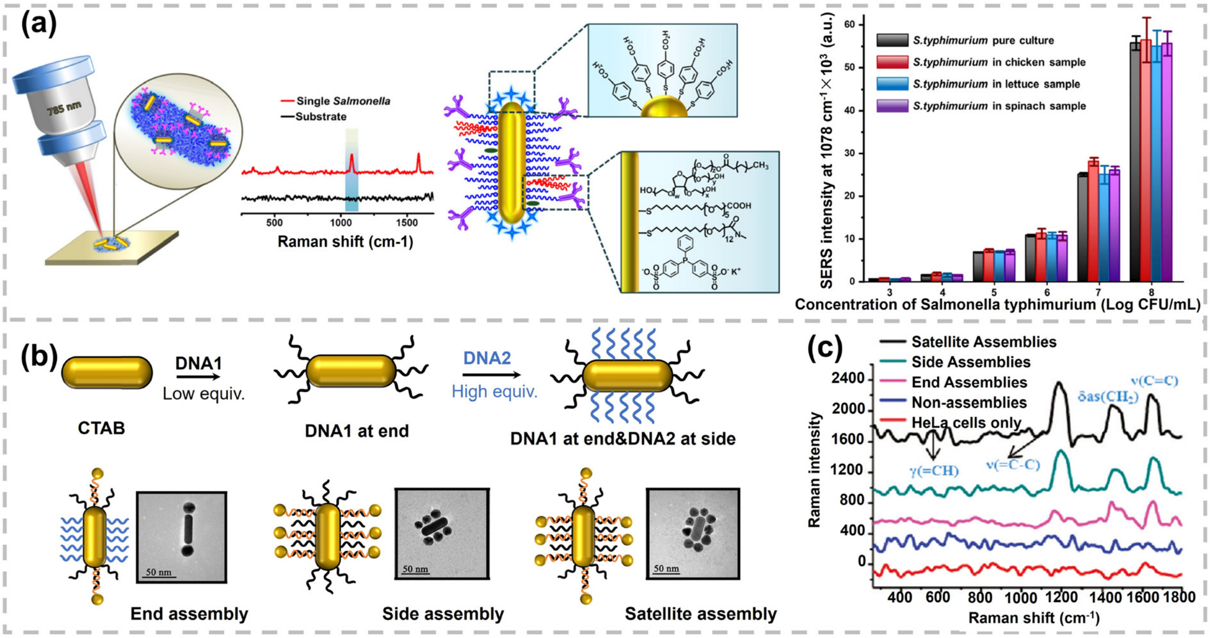

Fig. 12 (a) Schematic illustration of fabricating an AuNR-antibody based SERS label and its performance in food matrices. Reproduced with permission,[187] Copyright 2021, American Chemical Society. (b) Schematic representation of regioselective modification of AuNRs and three types of AuNP–AuNR assemblies. (c) Raman spectra of HeLa cells with three types of assemblies. Non-assemblies represent the mixture of AuNPs and AuNRs modified without complementary DNA. Reproduced with permission,[184] Copyright 2012, American Chemical Society.

placement on nanoparticles enables the rational design and synthesis of complex nanoarchitectures for subcellular sensing and imaging applications.[189]

The anisotropy of Janus NPs can also be utilized to modify two distinct bioreceptors to achieve multiplex detection. The Yuan group fabricated Janus SiO_2 NPs for the simultaneous and sensitive fluorescence detection of dual miRNAs in cancer cells (Fig. 13a).[190] One hemisphere of Janus NPs is functionalized with amine groups while the other hemisphere is decorated with AuNPs. Carboxyl-labeled H2 DNA strands are immobilized on the amine-functionalized hemisphere through amide bonds, whereas sulfhydryl-labeled H1 DNA strands selectively anchor onto the AuNP-functionalized hemisphere *via* the Au–S bond. Target miRNAs, miRNA-21 and miRNA-155, act as catalysts to initiate catalytic hairpin assembly reactions. Even trace amounts of target miRNA can result in numerous dsDNA walker complexes. These DNA walkers subsequently traverse along the 3D DNA tracks on their respective hemispheres of Janus NPs, driven by strand displacement amplification. During this process, the fluorophores (FAM and Cy5) are spatially separated from their quenchers (AuNPs or black hole quencher), leading to a significant fluorescence recovery. The spatial segregation of the two DNA probes on Janus SiO_2 NPs effectively prevents single molecule Förster resonance energy transfer (FRET) and minimizes signal crosstalk between distinct fluorophores, a common issue in homogeneous nanoparticle-based biosensors. The integration

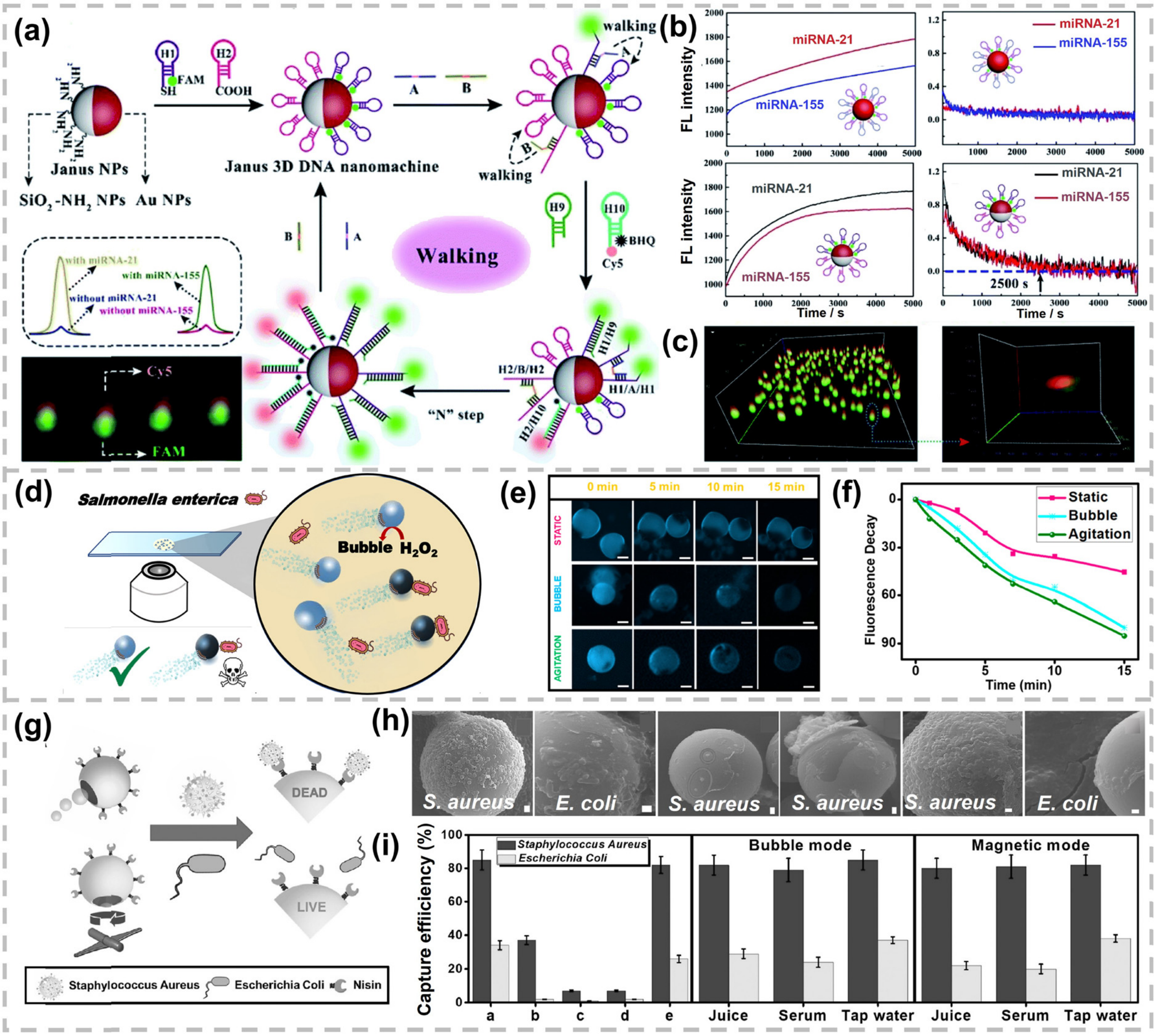

Fig. 13 (a) Schematic illustration of a Janus DNA nanomachine for simultaneous detection of miRNA-21 and miRNA-155. (b) Reaction rate of homogeneous and Janus DNA nanostructure in the presence of target miRNA. (c) 3D and individual enlarged 3D images of dual-color fluorescent Janus NPs. Reproduced with permission,[190] Copyright 2020, The Royal Society of Chemistry. (d) Schematic representation of enterobacterial contamination detection using a self-propelled Janus microsensor. (e) Time-lapse fluorescence images and (f) Fluorescence decay curves of Janus micromotors. Reproduced with permission,[192] Copyright 2018, American Chemical Society. (g) Scheme of catalytic and magnetic driven GO/PtNPs/Fe_2O_3 Janus micromotors modified with Nisin for *S. aureus*. (h) SEM images of modified moving catalytic micromotors in *S. aureus.* and *E. coli* cultures, static modified micromotors, unmodified moving micromotors, modified magnetic moving micromotors (from left to right) in *S. aureus* and *E. coli* cultures. (i) Selectivity and capture efficiency of Nisin modified micromotors in bubble and magnetic modes. Reproduced with permission,[194] Copyright 2021, Wiley-VCH.

of catalytic hairpin assembly reaction and the 3D DNA walker provides dual amplification, enabling ultra-sensitive detection with LODs as low as 0.35 pM for miRNA-21 and 0.48 pM for miRNA-155. Compared with homogeneous SiO_2 NPs, Janus SiO_2 NPs exhibited higher walking efficiency and accelerated reaction kinetics due to the reduced steric hindrance and ordered probe arrangement. Notably, the fluorescence signal of homogeneous SiO_2 NPs failed to reach equilibrium even after 5000 s while the Janus SiO_2 NPs attained a stable plateau within only 2500 s (Fig. 13b). Additionally, the Janus architecture allows for the precise visualization of both miRNAs in the same subcellular location within living cells, providing more accurate and reliable co-localization information than the conventional fluorescence *in situ* hybridization and single-probe approaches (Fig. 13c).

The spatial distribution of bioreceptors can also accelerate response time and reduce sample volume in combination with self-propelled nanoparticles. Alberto Escarpa's group has engineered a series of self-propelled Janus nanoparticles as mobile sensors with satisfactory sensing metrics in terms of extremely low sample volumes and ultra-fast response time.[191] The micromotors are partially functionalized with catalytic layers to produce bubbles and propulsion forces, while the remaining surface is functionalized with bioreceptors to enable selective detection. For instance, the group pioneered a polycaprolactone micromotor encapsulated with PtNPs for bubble propulsion and 3-aminophenylboronic acid functionalized QDs for selectively binding to the lipopolysaccharide core of *Salmonella enterica* (Fig. 13d).[192] The interaction between the lipopolysaccharide core and QDs induced rapid fluorescence quenching. The LOD of this micromotor-based assay is as low as 0.07 ng mL^{-1}, far below the level considered toxic to humans (275 μg mL^{-1}). Additionally, this micromotor can successfully detect *Salmonella* toxin in food within 15 min, compared with approximately 24 h required by the existing gold-standard Limulus amoebocyte lysate test (Fig. 13e and f). Subsequently, the same group further developed a smartphone-based portable device in combination with Janus micromotors for glutathione detection.[193] The detection can be completed in less than 30 s, requiring only dropping human serum or plasma, along with the micromotors and fuel solution, onto a glass slide. The average cost per analysis is estimated to be 0.05€, considering the cost of fuel, micromotors and surfactants. Furthermore, GO/PtNPs/Fe_2O_3 wrapped Janus micromotors of dual-mode propulsion, including catalytic self-propulsion and fuel-free magnetic actuation, have been constructed (Fig. 13g).[194] The surface of GO was modified with lanbiotic Nisin for specific binding to Lipid II in the cell walls of Gram-positive bacteria and biofilms. This Janus micromotor exhibited ~85% capture efficiency for *Staphylococcus aureus* (*S. aureus*), compared with only 20–28% capture efficiency for *Escherichia coli* (*E. coli*) (Fig. 13h and 13i). Over 90% inactivation of *S. aureus* and approximately 80% removal and inhibition of *S. aureus* biofilms were achieved under dual propulsion modes. Additionally, the GO/PtNPs/Fe_2O_3 Janus micromotors remained effective in complex media, such as juice, serum, tap water, and even whole blood.

3.4.2. Regioselective modification based on DNA frameworks.

Despite regioselectivity achieved in these above nano–bio interfaces, precise control of all interfacial parameters, including conformation, coverage, components and spatial distribution, remains elusive. DNA frameworks, including two-dimensional structures (square, triangle and cross) and 3D objects (cubes, tetrahedra, hemispheres, toroids and ellipsoids), can act as programmable nanoparticles in biosensors.[195–197] DNA frameworks offer an unique advantage to control the position and valency of diverse sensing elements with nanometer-scale resolution.[198–200] Hu and coworkers constructed a valency-controlled DNA framework with tunable biosensing performances.[201] Two hairpin DNAs, H1 and H2, were modified on DNA frameworks with controlled valency for hairpin assembly reaction based on toehold-mediated strand displacement. miRNA-21 could catalyze the hybridization between H1 and H2 and subsequently was released to trigger additional H1–H2 hybridization cycles. The DNA framework probe adopts a quenched hairpin structure with both FAM (fluorophore) and DABCYL (quencher) modified on the stem of H2. When H2 was hybridized with H1, the DNA framework probe was lit up, enabling the amplified detection of miRNA-21. The valency of H2 per DNA framework is 1 with a tunable valency of H1 from 1 to 7 in Fig. 14a. The time required to reach the same fluorescence response decreased with increasing number of H1 (Fig. 14b). Correspondingly, the LODs gradually increased from 1 nM to 8 nM with the decreasing number of H1 (Fig. 14c). Moreover, the dynamic ranges of DNA frameworks shifted to a lower concentration with increasing H1 (Fig. 14d). The performance of heterogeneous DNA frameworks could be precisely modulated by tuning the different valencies of DNA ligands, providing the tunable biosensing ability according to a specific situation.

Mao and colleagues have developed DNA origami with multivalent aptamers to boost the binding affinity for tumor cells (Fig. 14e).[202] The effect of aptamer valency and interspacing of multiple aptamers on cellular binding affinity was investigated, including the EpCAM aptamer, epidermal growth factor receptor (EGFR) aptamer and HER2 aptamer. By precisely adjusting the valency and spatial arrangement of multiple aptamers, a specific topology to match spatial distribution of target membrane protein clusters on cancer cells was constructed, termed as $O(\text{I})_3O(\text{II})_3O(\text{III})_3$. The binding sites O(I), O(II), and O(III) on DNA origami refer to inner loop regions with radii of 19 nm, 35 nm, and 62 nm, respectively (Fig. 14f). Specifically, the DNA nanostructure $O(\text{I})_3O(\text{II})_3O(\text{III})_3$ was functionalized with three EpCAM aptamers at a 19 nm radius region, two EGFR aptamers and one HER2 aptamer at a 35 nm radius and three EpCAM aptamers on a 62 nm radius region. For comparison, $O(\text{III})_3$, $O(\text{I})_3$, and $O(\text{I})_3O(\text{III})_3$ were all modified by EpCAM aptamers. The K_d values of designed DNA nanostructures against the Michigan Cancer Foundation-7 cell were 263.9 pM for $O(\text{I})_3O(\text{II})_3O(\text{III})_3$, 613.7 pM for $O(\text{III})_3$, 2089.5 pM for $O(\text{I})_3$, and 4889 pM for $O(\text{I})_3O(\text{III})_3$, respectively. $O(\text{I})_3O(\text{II})_3O(\text{III})_3$ possessed 3000-fold higher binding affinity towards the Michigan Cancer Foundation-7 cell than that of the DNA nanostructures with a monovalent aptamer. Hu *et al.* designed a series of adjustable multivalent aptamer-based DNA frameworks with tube or patch-like structure to precisely regulate their interactions with the receptor of tumor cells.

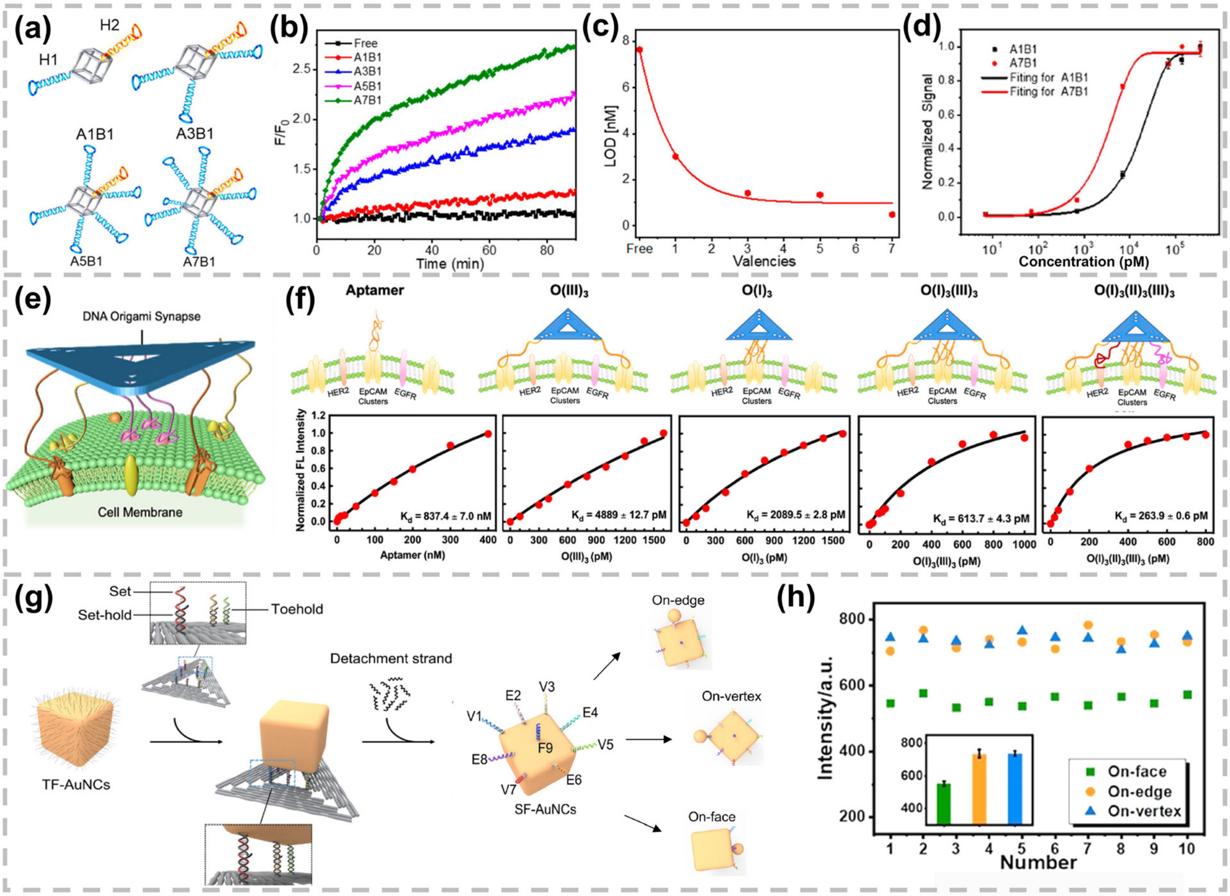

Fig. 14 (a) Construction of DNA framework probes with an equal amount of H2 and tunable numbers of H1. (b) Time-dependent fluorescence intensity, (c) LOD, and (d) dynamic range of DNA framework probes with controlled valency. Reproduced with permission,[201] Copyright 2019, American Chemical Society. (e) Scheme of DNA frameworks with precise recognition and high-affinity binding for target cells. (f) Determination of K_d of different DNA frameworks. Reproduced with permission,[202] Copyright 2023, American Chemical Society. (g) Preparation of SF-AuNCs with the precisely controlled number and position of DNA and SF-AuNC-AuNP nanoassemblies with different gap morphologies. (h) Comparison of ten sets of Raman intensities taken from three types of SF-AuNC–AuNP nanoassemblies. Reproduced with permission,[206] Copyright 2021 Wiley-VCH.

These frameworks enabled multi-heteroreceptor-mediated recognition through precise control of aptamer type, valency, and geometric arrangement. This strategy not only favored the specific binding of nanostructures to tumor cells but also promoted clathrin-dependent endocytosis and intracellular uptake. Notably, tube-like structures with different diheteroaptamer pairs exhibited more than 5-fold higher uptake across various tumor cell types, demonstrating their strong potential for targeted drug delivery. In contrast, patch-like structures with triheteroaptamers were able to selectively direct specific macrophage towards tumor cells, leading to effective immune clearance.[203]

Advances in DNA nanotechnology enable precisely patterning DNA onto nanoparticles regarding coverage, components and spatial position. For instance, Sleiman *et al.* transferred DNA strand motifs from a parent 3D DNA template onto AuNPs, which provided arbitrary control over sequence, DNA number and their relative placement and directionality.[204] Instead placing AuNPs onto DNA templates, Xie and coworkers encapsulated AuNPs into a DNA icosahedron cage and then transferred the molecular recognition elements from DNA nanocages to the inner AuNP surface.[205] Various combinations of overhangs extended from the DNA icosahedron cage can be retained onto AuNPs *via* Au–S bonds. The DNA nanocage allows DNA to be transferred into a larger area on AuNPs compared with placing AuNPs onto DNA templates. Recently, the asymmetric pattern on DNA origami templates has been accurately transferred onto the surface of thiolated DNA functionalized gold nanocubes (TF-AuNCs) (Fig. 14g).[206] The prepared specific functionalized gold nanocubes (SF-AuNCs) were named V1 to F9, with 9 DNA strands at their vertices, edges and faces. When small AuNPs with densely packed complementary DNA were hybridized with the DNA strands on the vertices, edges and face of SF-AuNCs, a series of high-order and discrete nanostructures formed. Single molecule Raman spectra of three representative types of SF–AuNCs–AuNP nanoassemblies with different gap morphologies were studied. Raman signals of on-vertex and on-edge SF–AuNC–AuNP nanoassemblies were significantly stronger than that of on-face SF–AuNC–AuNP nanoassemblies, while the former two exhibited comparable intensities (Fig. 14h). Due to the high SERS enhancement factor, these plasmonic AuNC–AuNP

Table 4 Enhanced sensing performance of nanoparticle-based biosensors by tailoring spatial distribution of bioreceptors

Surface-bioreceptor	Tailoring approach	Analyte	Signal strategy	Enhanced sensing performance	Ref.
AuNRs–antibody	Shape	*Salmonella* bacteria	SERS	Single molecule detection of *Salmonella* bacteria in complex food matrices	187
AuNRs–DNA	Shape	Lipid	SERS	Enhanced Raman signal and works as a Raman probe in live cells	184
SiO_2 NPs–DNA	Janus NPs	miRNA-21, miRNA-155	FL	Multiplex detection and fast response time Precise visualization of two miRNAs and reliable co-localization	190
QDs-saminophenylboronic acid	Janus NPs	*Salmonella enterica*	FL	Low LOD and fast response within 15 min	192
GO/PtNPs/Fe_2O_3-Nisin	Janus NPs	*S. aureus*	FL	Good specificity and effective in complex media	194
DNA framework-DNA	DNA framework	MicroRNA21	FL	8 times increase in sensitivity with increasing number of H1	201
DNA framework-aptamer	DNA framework	Cancer cells	FL	3000-fold higher binding affinity	202
SF-AuNCs	DNA framework	—	SERS	Enhanced Raman signal and ideal platform for ultra-sensitive sensing	206

nanoassemblies provide an ideal platform for ultra-sensitive sensing and single-molecule research.

In summary, the approaches of preparing site-specific biofunctionalized nanoparticles primarily rely on controllable surface accessibility or DNA frameworks listed. DNA strands can be site-selectively modified on the surface of anisotropic nanoparticles and further assembled into well-defined architectures, mainly improving the sensitivity of SERS-based biosensing. Janus NPs with two different types of bioreceptors on opposite hemispheres can achieve multiplexed detection, thereby facilitating precision medicine. Beyond multiple detection, self-propelled Janus NPs integrating both bioreceptor and catalytic regions can significantly accelerate response time and minimize sample volume. Additionally, DNA frameworks allow precise control over the number, the type and the spatial distribution of DNA strands, either within the framework or by transferring predefined DNA patterns onto nanoparticle surfaces. This powerful capability provides substantial opportunities for biosensors with tunable analytical performances. Although regioselective modification of bioreceptors on nanoparticles has opened new avenues for improving various sensing merits, current research in this field has mainly focused on developing stable and easily implementable synthetic strategies, while their applications in quantitative biosensors remain at an early stage. In contrast to DNA, precise control over antibody functionalization on nanoparticles is more challenging due to the larger molecular size, structural diversity and unpredictable physicochemical properties of antibodies.[158] Moreover, the antibody bioactivity is more susceptible to perturbation induced by nanoparticle surfaces. Therefore, there is a longer journey to realizing precise and reliable control of antibodies on nanoparticles (Table 4).

4. Characterization of the nano–bio interface

To further elucidate the effect of nano–bio interfacial factors on sensing performances, surface analysis techniques are required to precisely probe the orientation, coverage, spatial distribution of bioreceptors as well as the composition on nanoparticles. However, such characterization is still challenging and limited due to the nanoscale size, surface curvature, and inherent heterogeneity of nano–bio interfaces. This section summarizes available approaches for characterizing the nano–bio interfacial parameters discussed above, encompassing both widely accessible conventional techniques and advanced analytical approaches at the single particle level.

4.1. Characterizing the orientation of bioreceptors

The orientation of the immobilized antibody is often indirectly estimated from antigen binding efficiency *via* immunoassay. However, conclusions inferred from binding efficiency are easily affected by other factors, such as stability of antibody–nanoparticle conjugates, antibody coverage and immunoassay conditions, which may obscure the true orientation of antibodies. To directly probe the orientation of antibodies, time-of-flight secondary ion mass spectrometry (TOF-SIMS) combined with principal component analysis has been employed. TOF-SIMS analyses the mass of secondary ions sputtered from a surface under primary-ion bombardment (Fig. 15a).[207,208] TOF-SIMS serves a powerful surface characterization tool for both nanoparticles and biomolecules with a lateral resolution down to 30 nm. The principle of using TOF-SIMS to characterize antibody orientation relies on the fact that amino acid-related secondary-ion fragments reflect the outermost exposed region of antibodies. As the Fc and Fab domains possess different amino-acid compositions, multivariate principal component analysis of these fragments enables the identification of preferentially exposed domains and thereby the orientation of antibodies (Fig. 15b). Gajos *et al.* investigated how the antibody coverage governs the molecular orientation and immunological recognition on silicon substrates.[209,210] Physical adsorption and two covalent coupling strategies—NHS-silane and amino-silane followed by glutaraldehyde activation–were compared. They demonstrated that the orientation of antibodies was affected by both surface coverage and immobilization approaches. NHS-silane promoted mixed orientations of head-on and tail-on due to intermolecular interactions, whereas glutaraldehyde activation favoured a dominant head-on orientation (Fig. 15c). More

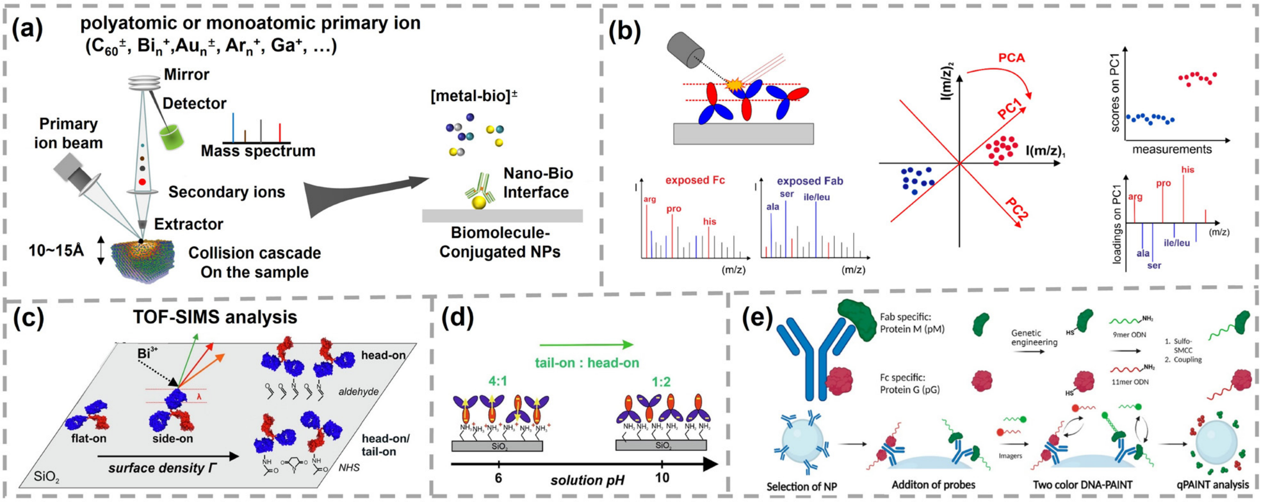

Fig. 15 (a) Schematic diagram of TOF-SIMS for probing nano–bio interfaces. Reproduced with permission,[208] Copyright 2014, Wiley-VCH. (b) The principle of characterizing antibody orientation by TOF-SIMS. The exposed Fc and Fab domains in the outermost region exhibit distinct amino acid compositions. Reproduced with permission from ref. 210, under the CC BY 4.0 license. (c) TOF-SIMS analysis of the orientation of IgG immobilized by APTES/glugtaraldehyde and NHS-silane. Reproduced with permission,[209] Copyright 2020, Elsevier. (d) Schematic representation of the vertical arrangement of the antibody immobilized by amino-silane at different pH values. Reproduced with permission,[211] Copyright 2024, Elsevier. (e) Mapping the antibodies on the surface of nanoparticles using DNA-PAINT. Reproduced with permission,[213] Copyright 2023, American Chemical Society.

recently, they further observed that the orientations of both physical adsorbed and covalent bound antibodies were pH-dependent (Fig. 15d).[211] The proportion of antibodies adopting tail-on and head-on orientations decreased with increasing pH. The actual fraction of the exposed Fc domain was approximately 0.1 for pH $<$ 7 to about 0.35 for pH $>$ 10. Overall, these studies provide a direct and quantitative framework to probe the antibody orientation that is affected by the immobilization protocol and antibody surface coverage. Such quantitative information on antibody orientation is valuable for the rational design of high-sensitivity biosensors. However, the above studies determined the antibody orientation at the silicon substrate rather than nanoparticles. Future investigations using TOF-SIMS to characterize the antibody orientation on nanoparticles are expected. Super-resolution fluorescence microscopy techniques can map the epitopes of antibodies on nanoparticles at a single particle level. DNA-point accumulation for imaging in nanoscale topography (PAINT), based on the short transient interaction of a labeled DNA probe (imager) to a complementary DNA target, has become a quantitative method to probe the orientation of antibodies on a single particle.[212] Albertazzi and co-workers have quantified the orientation of the antibodies based on dual-color DNA-PAINT using a Fab-specific protein M coupled probe and Fc-specific protein G (Fig. 15e).[213] The numbers of Fab and Fc binding sites per nanoparticle were quantified simultaneously, providing a powerful strategy for designing nanoparticles with controlled Fab and Fc exposure.

Approaches for monitoring the conformation of DNA generally rely on distance-dependent optical techniques, including single molecule FRET, SERS, and surface plasmon resonance. Single molecule FRET is a powerful technique for probing the conformation dynamics and interactions of biomolecules.[214] In the context of nano–bio interfaces, Hildebrandt and coworkers employed time-resolved FRET to systematically investigate the conformation of DNA attached onto dihydrolipoic acid (DHLA)-PEG coated QDs (Fig. 16a).[215] A terbium complex, serving as a donor, was conjugated to DNA hybridized at different positions along a 31-nucleotide DNA strand, which was linked to the QD acceptor *via* a peptide-His tag. Terbium-QD distances can be adjusted from 7 nm to 14 nm by varying the hybridization sites. It was found that ssDNA exhibited a flexible orientation near QDs with a compact structure of 0.15 nm per base, while dsDNA adopted a radial orientation with full extension of 0.31 nm per base pair. Subsequently, his group extended the terbium-QDs FRET platform to artificial bidomain proteins. The artificial bidomain proteins were labeled with a terbium complex on its C-terminus and a QD acceptor on its N-terminus.[216] Specific binding of one or two protein targets to the artificial bidomain protein induced a conformational opening of the bidomain scaffold, accompanied by a corresponding fluorescence change. The Ju group has employed SERS to probe DNA conformation on multibranched gold nanostars to determine DNA orientation (Fig. 16b).[217] Cy5 labelled DNA strands were assembled on gold nanostars *via* polyA, whose length controlled whether the DNA strands adopted a "lie-down" or "stand-up" conformation. As SERS enhancement is extremely sensitive to the distance between the Raman reporter and the gold surface, especially at electromagnetic "hot spots" located at the tips of nanostars, conformational changes in DNA translate directly into fluctuation in SERS intensity. Specifically, increasing the polyA length or inducing DNA hybridization extends the DNA away from the surface of gold nanostars, resulting in a reduced SERS signal. This study demonstrates that SERS enables *in situ* and quantitative monitoring of DNA conformation on nanoparticles. Similarly, surface plasmon resonance can also be utilized to probe the DNA conformation based on the distance-dependent plasmonic

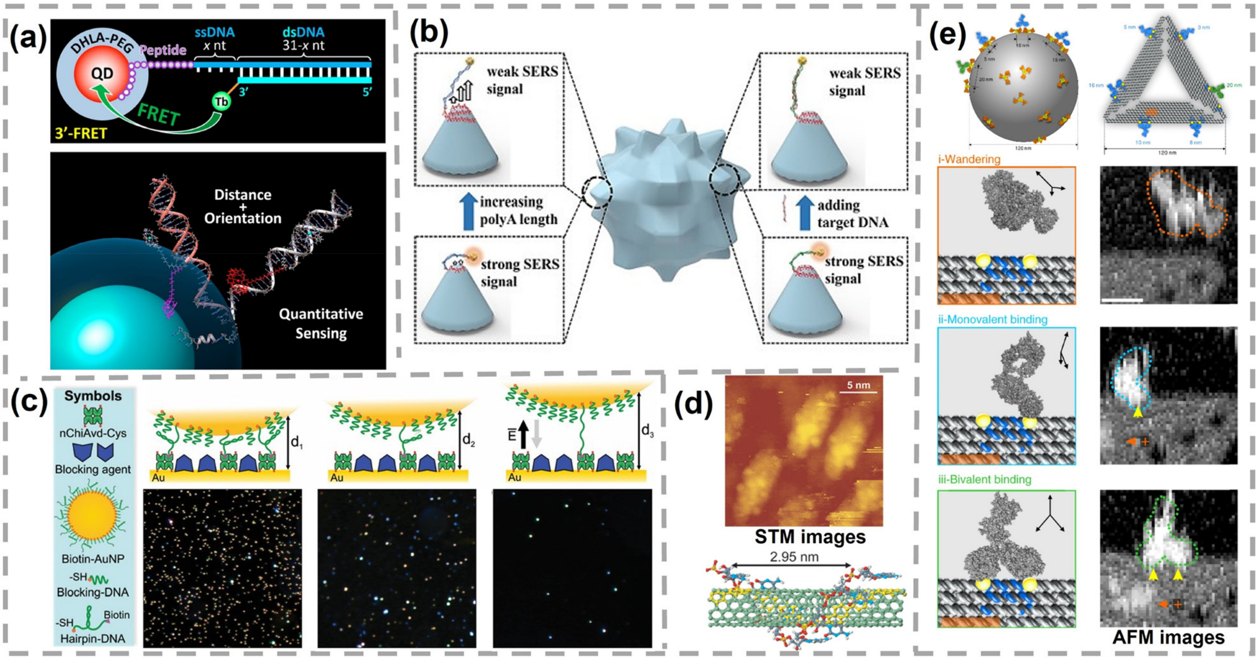

Fig. 16 (a) Schematic diagram of a terbium-QD based FRET nanoruler to investigate the conformation of ssDNA and dsDNA. Reproduced with permission,[215] Copyright 2018, American Chemical Society. (b) Schematic illustration of SERS to monitor DNA conformation on gold nanostars. Reproduced with permission,[217] Copyright 2017, Wiley-VCH. (c) Schematic representation of an AuNP–DNA nanoactuator on gold film and its application in assembly characterization based on surface plasmon resonance and dark-field scattering microscopy. Reproduced with permission,[218] Copyright 2018, The Royal Society of Chemistry. (d) STM topographic image of CNT–DNA hybrids on a Si substrate. Reproduced with permission,[220] Copyright 2009, American Chemical Society. (e) Schematic diagram of viral particles and virus-mimicking DNA origami epitopes for IgG binding. The bottom are high-speed AFM images of a three-stage binding process. Reproduced with permission,[224] Copyright 2020, Springer Nature.

coupling between AuNPs and a neutral cysteine-tagged chimeric avidin (nChiAvd-Cys) modified planar gold surface (Fig. 16c).[218] Dark-field scattering microscopy provides a direct and label-free optical readout of DNA conformational switching. The spectral shift of individual AuNPs correlates with the conformation of the hairpin DNA linker. By varying the applied electric field, the hairpin DNA can switch reversibly between folded and unfolded states, producing quantifiable shifts in the scattering responses. Owing to its single particle sensitivity and straightforward optical transduction, this surface plasmon resonance-based strategy is readily extended to monitor conformational changes of other biomolecules.

Other techniques based on scanning probe microscopes, such as scanning tunneling microscopy (STM) and atomic force microscopy (AFM), have been used to explore the orientation or conformation of biomolecules at the sensing interface. STM enables the direct visualization of individual biomolecules with near-molecular resolution. For instance, the IgG antibody labeled with 5 nm AuNPs, as well as antibody–antigen complexes, has been imaged on atomically smooth pyrolytic graphite by STM.[219] Yarotski and coworkers utilized STM to characterize the carbon nanotube (CNT)–DNA interface on a p-doped Si substrate and revealed both the spatial arrangement and interaction mechanism of DNA on CNTs (Fig. 16d).[220] DNA-coated CNT segments appear as protruding islands, and the periodic height modulations in topography directly revealed the DNA wrapping geometry with a coiling period of 3.3 nm and a wrapping angle of 63° relative to the CNT axis. Additional width and height modulations along the DNA strand were also observed with characteristic lengths of 1.9 and 2.5 nm. This stable wrapping configuration was attributed to the optimal π-stacking, arising when DNA bases align with the helical orbital and charge-density pattern of CNTs. Compared with STM, AFM is not restricted to conductive samples and therefore more widely used for imaging biomolecules.[221,222] The development of high-speed AFM has significantly improved the temporal resolution into the millisecond and even microsecond regime, making it suitable for observing dynamic processes.[223] Fan's group investigated the transient binding conformations of IgG by high-speed AFM (Fig. 16e).[224] DNA origami epitopes decorated with precisely spaced digoxin "spikes" were designed to capture IgG. Single-event transitions of IgG from wandering, monovalent binding, bivalent binding and wagging motions of Fc domains during the binding process were directly visualized by high-speed AFM. By varying the digoxin spacing from 3 to 16 nm, it was found that IgG molecules adopted conformations from highly compact to fully extended. Despite these advances, probing the orientation of bioreceptors on nanoparticles utilizing STM and AFM remains challenging. Both STM and AFM typically require atomically smooth surfaces as the tip convolution effect becomes significantly exacerbated on the highly curved surfaces of nanoparticles.[225] In addition, the intrinsic heterogeneity of nano–bio interfaces complicates the discrimination between signal variations arising from particle heterogeneity and those induced by tip artifacts or environmental fluctuations. Therefore, most existing studies of sensing nano–bio interfaces by STM and AFM have focused on macroscopic and planar substrates rather than nanoparticles. Moreover, as STM relies on tunneling current, the presence of insulating bioreceptor layers on nanoparticles leads to fuzzy images and reduced image resolution. Finally, STM requires specialized operators in sample preparation, imaging parameter optimization, and data interpretation, which further limits its wide range of applications in nano–bio interfacial characterization.[226]

4.2. Characterizing the coverage of bioreceptors

Methods of quantifying the bioreceptor coverage on nanoparticles at the ensemble level include radio-labeled assay, UV-vis and fluorescence spectroscopy, mass spectrometry, surface plasmon resonance and quartz crystal microbalance.[227–232] The nano–bio conjugates typically require preparatory treatments prior to the measurements. For instance, to quantify the amount of protein on nanoparticles, the nano–bio conjugates are subjected to acidic treatment that simultaneously hydrolyses the grafted protein and degrades nanoparticles. Subsequently, a spectrophotometric assay is performed to determine the concentration of primary amines in the resultant solution.[233] Regarding bioconjugates of AuNPs, DNA strands or antibodies were commonly released from nanoparticles by ligand exchange or decomposing the nanoparticle core.[229,234,235]

Besides quantification at the ensemble level, determining the number of bioreceptors at the single particle level is highly desired. TOF-SIMS can be operated in an event-by-event detection mode to quantify DNA loading on single gold nanostars in a label-free manner (Fig. 17a).[236] Individual nanostars were analyzed using massive Au_{400}^{4+} cluster projectiles, where each impact probed a nanometric emission volume with a lateral diameter of 10–15 nm and a depth of 5–10 nm. DNA loading was extracted from ion-coincidence analysis between gold cluster ions (*e.g.*, Au_7^-) and DNA-specific phosphate and nucleobase-related ions. As co-emitted ions originate from the same nanovolume, their coincidence provides direct evidence of DNA present within the probed surface region. The coincidental yield, defined as the fraction of impacts on a nanoparticle that produces DNA-related ions, is utilized as a quantitative metric of DNA loading per particle. By normalizing the coincidental yields to reference particles of 50 nm gold nanospheres, DNA loading can be quantitatively compared across nanostars with different morphologies. This event-resolved TOF-SIMS enables direct determination of DNA loading on individual AuNPs, revealing how nanoscale curvature and geometry influence the loading density of bioreceptors. DNA-PAINT can also be adopted to quantify the coverage of bioreceptors at the single particle

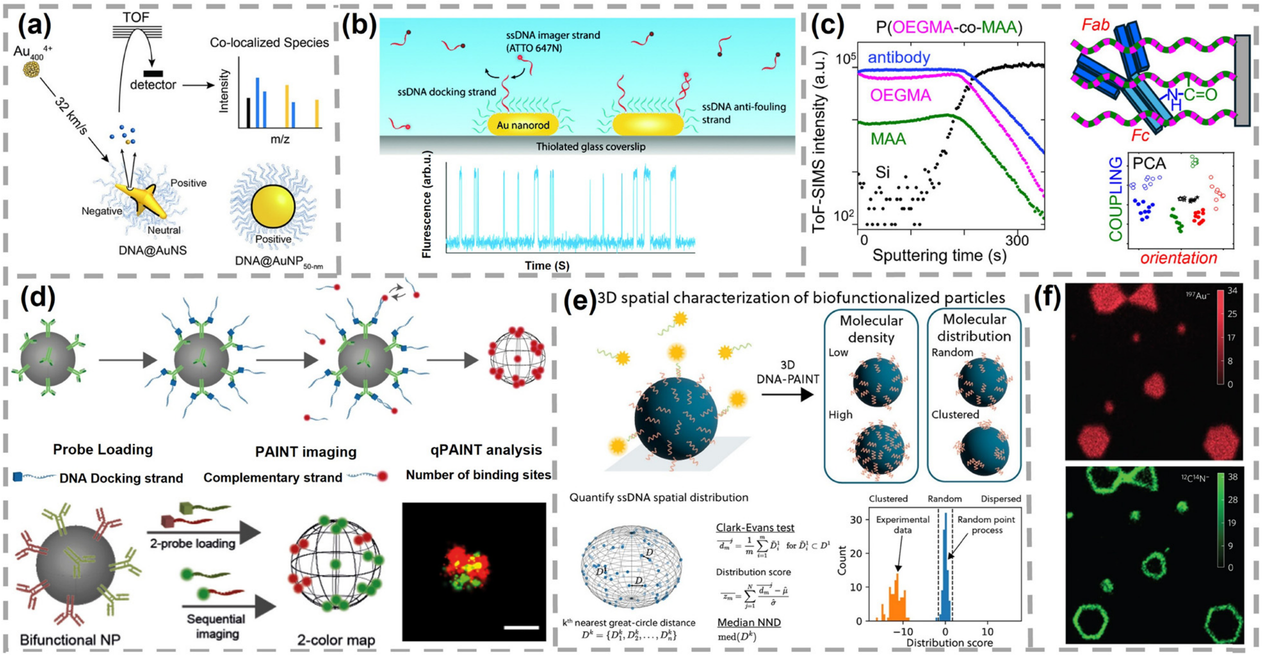

Fig. 17 (a) Schematic diagram of TOF-SIMS to quantify the number of DNA on nanostars. Reproduced with permission,[236] Copyright 2019, American Chemical Society. (b) Schematic illustration of functionalized nanoparticles for quantitative single-molecule counting based on DNA hybridization kinetics. The temporal analysis of the bursts reveals the number of functional groups on each individual particle. Reproduced with permission,[237] Copyright 2020, The Royal Society of Chemistry. (c) Schematic representation of TOF-SIMS to investigate the composition distribution of copolymers and antibodies. Reproduced with permission,[250] Copyright 2025, American Chemical Society. (d) DNA-PAINT based methodology for mapping active sites of anti-digoxigenin and anti-biotin antibodies on functional nanomaterials. Reproduced with permission,[238] Copyright 2018, American Chemical Society. (e) 3D spatial characterization of biofunctionalized DNA on nanoparticles and calculated distribution score of DNA. Reproduced with permission,[251] Copyright 2025, American Chemical Society. (f) NanoSIMS images of Au nanostructures with elemental distributions of $^{197}Au^-$ and $^{12}C^{14}N^-$. Reproduced with permission,[252] Copyright 2016, Springer Nature.

level. The Zijlstra group determined the number of DNA on individual AuNRs (a diameter of 22 nm and a length of 75 nm) in high-throughput *via* quantitative PAINT (Fig. 17b). AuNRs immobilized on a coverslip are functionalized with thiolated ssDNA docking strands. A fluorescent imager strand is introduced and imaged by total internal reflection fluorescent microscopy. Each transient binding event generates a burst, which is converted into a distribution of dark times between successive binding events. The dark-time histogram is fitted with a single-exponential to obtain the mean dark time, which scales inversely with the number of docking strands. Thus, with controlled imager concentration and known kinetic rates, the number of docking strands is obtained across large particle populations. A significant particle-to-particle difference in DNA coverage was observed among hundreds of AuNRs, ranging from 100 DNA per AuNR to nearly 600 DNA per AuNR.[237] The Albertazzi group quantified both antibodies and streptavidin per NP *via* multiplexed DNA-PAINT.[238] Similarly, significant heterogeneity of the available functional sites was found at both inter- and intraparticle levels.

4.3. Characterizing the composition of mixed ligands

Spectroscopy-based approaches are widely adopted to identify the composition of functional layers on nanoparticles, including nuclear magnetic resonance (NMR), Fourier-transform infrared spectroscopy (FTIR), mass spectrometry, and fluorescence microscopy with fluorescence labeling.[239–241] Although NMR is readily utilized to probe small molecules on nanoparticles, characterizing macromolecular bioreceptors such as antibodies or DNA by NMR remains challenging. The large molecular size of these bioreceptors and their slow rotational tumbling lead to severe line broadening and signal attenuation, which in turn reduce the signal-to-noise ratio and spectral resolution.[242] Meanwhile, the peak overlap, complex data analysis, and critical requirements in sample purity and homogeneity further limit the applicability of NMR in characterizing nano–bio interfaces.[243] In contrast, FTIR enables rapid assessment of the chemical composition of biofunctionalized layers on nanoparticles by probing the vibration and rotation mode of bioreceptors.[244,245] Key spectral windows include the protein and peptide region (amide I/II, 1800–1500 cm^{-1}), the carbohydrate region (C–O–C/C–O vibrations, 1200–900 cm^{-1}) and the nucleic-acid region (phosphate groups, 600–1200 cm^{-1}).[246–248]

Mass spectrometry provides complementary and compositional information by measuring the mass-to-charge ratio of characteristic ions, thereby resolving the composition of bioreceptor layers. For instance, Chen and colleagues employed TOF-SIMS operated in event-by-event detection mode to determine the binding sites of nanoparticle–antibody conjugates and their surface binding density on cells.[249] The binding sites between AuNPs and antibodies were inferred from coincidence mass spectra triggered by Au^- and AuCN^-. The simultaneous emission of cysteine ions indicated that AuNPs were bound by sulfur-terminal cysteine residues. Surface binding densities are then quantified using fractional coverage, defined as the ratio of effective projectile impacts on a given species to the total number of impacts. Coincidence of $\text{Au}^-/\text{AuCN}^-$ ions was used to quantify the surface coverage of AuNP–antibody conjugates, whereas the coincidence of palmitate and oleate ions quantified the coverage of phospholipid layers of cell membranes. The lipid membrane and AuNP–antibody conjugates were found to cover 23% and 21% of the cell surface, respectively. More recently, TOF-SIMS has been applied as a surface and depth sensitive tool to characterize the interfacial composition of mixed antibody and antifouling polymers as well as antibody orientation on a silicon substrate (Fig. 17c).[250] The characteristic secondary ions from 2-(2-methoxyethoxy) ethyl methacrylate (OEGMA) and methacrylic acid (MAA) confirm the composition of copolymers, and amino-acid fragments verify the existence of antibodies at the outermost interface. TOF-SIMS depth profiling further reveals a uniform copolymer composition through the polymer brush thickness. Furthermore, multivariate principal component analysis is applied to quantify the density and the orientation of interfacial antibodies.

4.4. Characterizing the spatial distribution of bioreceptors

DNA-PAINT and SIMS-based approaches have been established to probe the spatial distribution of bioreceptors on nanoparticles. DNA-PAINT can resolve the nanoscale distribution of functionally active sites of anti-digoxigenin and anti-biotin antibodies on nanoparticles. Each antibody was selectively targeted by its cognate antigen conjugated to a distinct DNA docking strand. Sequential introduction of complementary fluorescent imager strands enables super-resolution localization of each antibody population in separate imaging rounds using the same fluorophore. Merging the localization datasets produces a dual-color nanoscale map that directly reveals intraparticle heterogeneity of the two receptor populations (Fig. 17d).[238] More recently, the Prins group developed a quantitative workflow to determine the surface density and spatial organization of bioreceptors on planar substrates using single molecule DNA-PAINT.[251] The spatial distribution of surface-tethered DNA is obtained by extracting single molecule localizations from transient binding of dye-labeled imager strands to complementary ssDNA. Within each small region of interest, the time-accumulated ''localization clouds'' are clustered to estimate the center coordinates of individual immobilized ssDNA, yielding a point pattern of molecular positions. These coordinates are evaluated using the nearest-neighbor test against the complete spatial randomness hypothesis. The standardized mean nearest-neighbor distance classifies the distribution as significantly clustered, random, or significantly dispersed. They further extended this framework to 3D DNA-PAINT for the full curved surface of particles, followed by clustering to assign localizations to individual particle and compensation for under-sampling to quantify both interparticle and intraparticle heterogeneity (Fig. 17e).[252] In addition, the heterogeneity of DNA immobilized by two approaches, streptavidin–biotin coupling and PLL-*g*-PEG-N_3/PLL-*g*-PEG coating followed by click coupling, is analysed. Stronger interparticle variability existed for PLL-*g*-PEG-based click chemistry, possibly due to the heterogeneous polymer coating and the dynamic nature of PLL-*g*-PEG adsorption. For intraparticle heterogeneity, both chemistries yielded clustered ssDNA distributions, with slightly stronger clustering for the PLL-*g*-PEG click system, consistent with clustered reactive sites for multivalent streptavidin binding sites and multiple azides per azide-PLL-*g*-PEG chain.

In parallel, interfacial heterogeneity of different bioreceptors can be assessed by event-by-event nanoprojectile SIMS, generating independent mass spectrum per impact within nanoscale volume.[253] By screening millions of events for coincidence emission of tag-specific ions from antibodies with different labels, whether species are truly co-localized within the same nanometric volume or random aggregation can be quantified. A co-localization factor derived from the yield ratio is used to estimate the nanoscale inhomogeneity degree of antibodies on silicon wafer. Tags with different hydrophobicities can affect their attachment on the surface, while chemically similar tags produced near-random attachment. Additionally, nanoscale SIMS (NanoSIMS) offers direct chemical imaging of interfaces with lateral resolution down to 50 nm, which can directly image characteristic native ions or labels as stable isotopes halogens, metal and rare-earth elements.[254] Zhai *et al.* adopted NanoSIMS to probe the spatial distribution of polyvinylpyrrolidone on individual Au nanoprisms.[255] $^{12}\mathrm{C}^{14}\mathrm{N}^{-}$ signals attributed to the adsorbed polyvinylpyrrolidone were localized at the perimeters of nanoprisms rather than on their top [111] facets (Fig. 17f).

5. AI-driven nano–bio interfacial design

AI, particularly machine learning and deep learning, has demonstrated considerable potential in both the realm of nanomaterial and biomolecule-related tasks, such as controllable synthesis and assembly, and the prediction of physicochemical and binding properties.[256–260] However, within the biosensing field, AI remains concentrated on the downstream data analysis.[261–264] The integration of AI into the upstream nano–bio interface design and sensing performance prediction is still in its infancy. In this section, we first provide an overview of the typical workflow and key challenges associated with AI-driven nano–bio interfacial design in biosensors. Essential computational concepts, such as descriptors, featurization, model selection and validation, are included to bridge the knowledge gap for researchers in the biosensing field. The second section focuses on CNT–DNA interfaces as a model system to illustrate how AI can improve the sensing performances of CNT–DNA biosensors.

5.1. Workflow of AI-driven nano–bio interfacial design

The performance of nanoparticle-based biosensor depends not only on the nano–bio interaction but also on the specific bioreceptor–analyte interaction and the effective mitigation of nonspecific binding. Beyond understanding individual interactions, learning how they collectively interconnect and ultimately dictate key sensing metrics remains a considerably challenging task for AI models. In this context, the general workflow and associated challenges for AI-empowered nano–bio interface design in biosensing are summarized based on insights from protein corona studies and other nano–bio interaction systems (Fig. 18). The proposed framework begins with clarifying the analyte requirements and application scenarios, including the

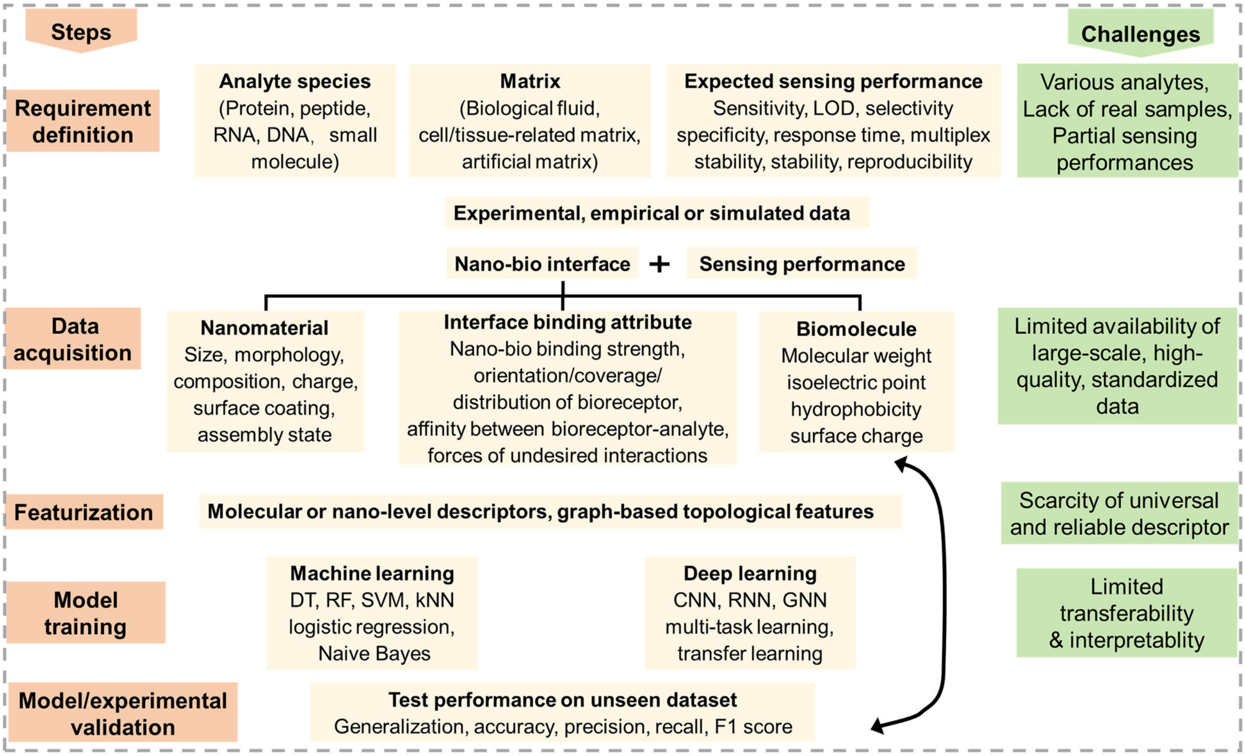

Fig. 18 General workflow and associated challenges for AI-empowered nano–bio interfacial design in biosensors.

various analyte species (*e.g.*, protein, peptide, RNA, DNA, or small molecule), the matrix (such as biological fluids, cell/tissue-related matrices, or artificial matrices) and the expected sensing performance criteria. This initial step establishes a well-defined objective that guides subsequent data acquisition and model development.

As a comprehensive dataset is indispensable for effective AI-assisted modeling, the next step is data acquisition. Experimental, empirical or simulation-derived data are acquired to describe the structural parameters and physiochemical properties of nanomaterials and biomolecules, binding attributes of nano–bio interfaces, and key indicators of sensing performances. Important parameters for nanomaterials include size, shape, composition, morphology, chirality, surface charge, surface modification, and assembly state. Molecular weight, isoelectric point, hydrophilic–hydrophobic property, and surface charge are involved in terms of bioreceptors.[265] The nano–bio interfacial binding attributes encompass binding strength of bioreceptors (covalent or noncovalent bonds), bioreceptor–analyte affinity, orientation, coverage and spatial distribution of bioreceptors, and the driving forces underlying the undesired interactions. The output variables correspond to single, or multiple biosensing performance metrics as described above. A major challenge in this step is the scarcity of large-scale and high-quality, standardized datasets that jointly capture nano–bio interaction features and biosensing performances. Experimental values frequently vary across laboratories and protocols, compromising reliability and comparability in the absence of universally accepted references. The difficulty here also includes the lack of complex samples, in which matrix effects are more pronounced. Data obtained from complex biological samples are crucial for translating laboratory-based strategies into practical methods for detecting analytes in human fluids or cell/tissue-related matrices. Furthermore, while most biosensor studies emphasize the sensing performance of sensitivity and LOD, performance metrics related to stability and reproducibility remain relatively underexplored, further constraining the robust development of AI-driven models.

Subsequently, experimental or computational data are transformed into feature sets compatible with AI models, which requires deliberate encoding of nanomaterial properties. Compared with small organic molecules, generating meaningful descriptors for nanomaterials is challenging due to their structural complexity and morphological diversity. To address this issue, descriptors from experimental properties, quantum chemical calculations, periodic table properties and full nanostructure representations have been developed to capture the structural and physicochemical characteristics and to encode complex nanostructures.[266] Common predictors encompass experimental parameters such as zeta potential, particle size, surface area, curvature, shape, and surface charge.[267] Simulation-derived descriptors extracted from atomistic MD simulations, including ligand dynamics, solvation, hydrogen bonding, interaction energies, electrostatic potentials, are utilized for quantitative nanostructure–activity relationship models.[268] Response-based descriptors, introduced by Zhong's group, exploit the fluorescence change of fluorescamine-labelled protein in the presence and absence of nanomaterials.[269] When used as input to the machine learning models, these descriptors have demonstrated enhanced predictive performance compared with independent properties of nanomaterials or proteins. Apart from molecular or nano-level descriptors, the Zhu group pioneered the concept of virtual molecular projections to digitally represent complex nanostructures.[270] Nanoparticles are simulated in three dimensions and converted into multidimensional arrays encoding atom types and spatial coordinates. When fed directly into convolutional neural network (CNN) models, these virtual projections enable accurate prediction of cellular uptake, lipophilicity, and zeta potential of nanoparticles. The same team further established PubVINAS, a publicly accessible online nanomaterial database integrating 705 annotated nanostructures across 11 material types.[271] Despite these advances, the availability of robust, meaningful and universal nanodescriptors remains limited due to the inherent heterogeneity and incomplete characterization of nanomaterials. Moreover, the physicochemical characteristics of nanomaterials are highly sensitive to media—agglomerating, dissolving, and dynamically adsorbing or desorbing surrounding molecules—further complicating the development of efficient and generalizable descriptors.[272] Therefore, incorporating both nanomaterial heterogeneity and environmental variables into descriptor design is essential for establishing reliable structure–function correlations.

Next, appropriate AI models are selected, trained, and iteratively refined according to specific biosensing tasks. Machine learning and deep learning are the two most prevalent AI models employed in materials science and biomedicine. Machine learning leverages statistical algorithms to learn patterns from data and generate predictions without being explicitly programmed, including decision trees (DTs), random forest (RF), support vector machine (SVM), k-nearest neighbour (kNN), logistic regression and Naive Bayes.[272,273] In contrast, deep learning, as a subfield of machine learning, employs multi-layer artificial neural networks to automatically learn hierarchical data representations.[272] Representative deep learning architectures include CNNs, recurrent neural networks (RNNs), graph neural networks (GNNs), as well as multi-task and transfer-learning frameworks. Deep learning typically requires larger datasets and often suffers from limited interpretability. Nevertheless, it is particularly effective in cases where the governing variables and underlying mechanisms are complex, highly interdependent, and not fully understood in advance. For deep and thorough insights into AI models, refer to previous works.[274–276] As datasets describing nano–bio interfaces remain limited at the current stage, machine learning models are still adopted in most cases. However, deep learning offers distinct advantages for capturing the intricate and nonlinear relationships between nano–bio interfacial structures and biosensing performances, which is expected to play an increasingly important role in the future. The final step is experimental validation and closed-loop feedback.[277] Experimental results are reintegrated into the training dataset, enabling retraining and performance refinement in subsequent cycles. The model performances are evaluated on unseen data, focusing on generalization and key metrics such as accuracy, precision, recall, and F1 score.

5.2. AI-driven interfacial design of CNT–DNA biosensors

CNT–DNA hybrids are powerful near-infrared nanosensors that exhibit robust optical signal modulation upon analyte binding.[278] Several machine learning models have been developed to elucidate CNT–DNA interactions and their fluorescence modulation mechanism, offering a promising route to enhance sensing performance and facilitate rational biosensor design.[279] From the perspective of DNA sequence design, Kelich *et al.* applied machine learning to discover CNT–DNA biosensors for serotonin detection (Fig. 19a).[280] CNN classifiers and SVM regressors were trained to map sequence-derived features from 96 CNT–DNA conjugates with experimentally measured fluorescence responses at 1195 nm (Fig. 19b). The predictions were experimentally validated, and the validation results were used to retrain the models that identified DNA sequences with markedly enhanced sensitivity and selectivity (Fig. 19c). This study established a practical ''experiment–machine learning–re-experiment'' closed-loop framework, particularly suitable for the small-sample regime typical of nano–bio interface studies. Later, the same group further predicted the optical response of CNT–DNA for serotonin as a function of DNA sequence by exploiting the whole fluorescence spectra.[281] Regression models trained with SVM successfully distinguished high and low response DNA sequences. Incorporating multiple spectral wavelengths into model increased the prediction robustness and facilitated the discovery of novel CNT–DNA sensors. Besides DNA sequence optimization, Kim *et al.* utilized the spectral fingerprinting of quantum-defect-modified CNTs for the detection of ovarian cancer.[282] Organic colour centres (OCCs)—atomic-level quantum defects—are covalently functionalized onto nanotubes, creating well-defined and chemically tunable emissive states. Three OCC terminating groups and four ssDNA sequences were selected to construct a nanosensor array (Fig. 19d). Spectra from functionalized nanotubes were collected for patient and control sera, shown in Fig. 19e. A panel of supervised machine learning algorithms were evaluated, including logistic regression, artificial neural networks, DTs, RF and SVM. SVM approaches achieved the highest F-score among the tested algorithms. This sensing platform identified high-grade serous ovarian cancer with high positive and negative predictive values, achieving 87% sensitivity at 98% specificity.

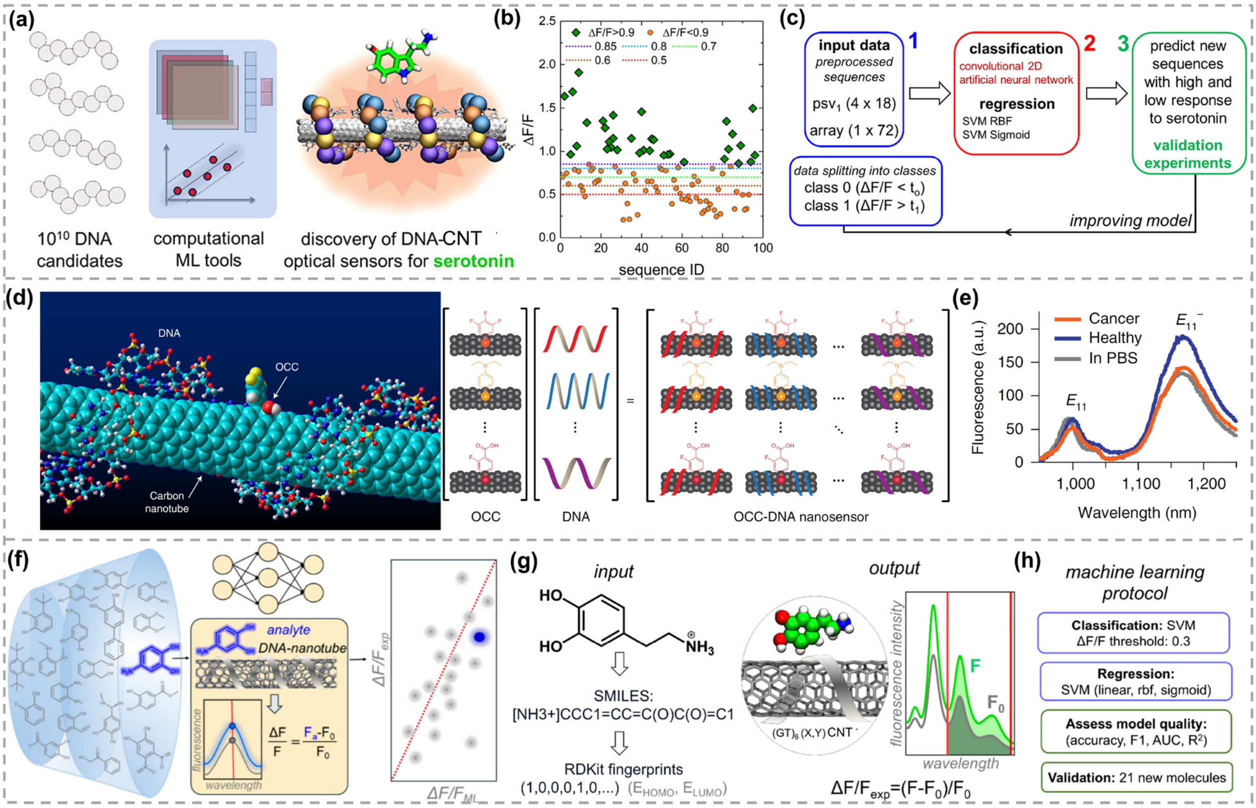

Fig. 19 (a) Discovery of DNA-CNT optical sensors for serotonin detection. (b) Optical responses of 96 unique CNT-DNA conjugates to serotonin. (c) Main computational approach. Reproduced with permission,[280] Copyright 2022, American Chemical Society. (d) OCC-DNA nanosensor array with different OCC terminating groups and four ssDNA sequences. (e) Representative fluorescence spectra of one OCC-DNA nanosensor. Reproduced with permission,[282] Copyright 2022, Springer Nature. (f) Machine learning models to predict analyte-induced fluorescence changes in CNT-DNA nanosensors for dopamine. (g) Transformation of analytes into molecular fingerprints with RDKit for the predictive modeling of optical responses. (h) Support vector classifiers and regression models validated against the original dataset and an independent 21-molecule blind set. Reproduced with permission,[284] Copyright 2026, American Chemical Society.

In parallel, Beyene and co-workers systematically investigated the molecular determinant of catecholamine-like analytes for CNT–DNA based fluorescent sensors.[283] The large optical responses strongly correlated with the electronic properties of bound ligands, such as electron density on the aryl motif, rather than the binding affinity alone. This insight highlights the importance of incorporating physicochemical descriptors of analytes and the local corona environment into machine learning models, moving beyond DNA sequence-based features toward physically informed representations. More recently, their group developed a machine learning model to predict the analyte-induced fluorescence response of a fixed CNT–$(GT)_6$ dopamine nanosensor (Fig. 19f).[284] Using a dataset of 63 small training molecules, each analyte was encoded using standard RDKit fingerprints with optional frontier molecular orbital energy descriptors. Principal component analysis of these molecular encodings was employed to map the chemical space and identify structural motifs associated with strong or weak fluorescence responses (Fig. 19g). Support vector regression and support vector classification were then utilized to predict continuous $\Delta F/F$ values and to discriminate strong or weak responses, respectively (Fig. 19h). Following cross-validation, the models were evaluated against an independent blind set of 21 molecules to assess their generalizability. While the classification model achieved robust discrimination (F1 $\approx$ 0.8), the regression performance was relatively modest (mean $R^2 \approx 0.2$–0.4). Collectively, this work demonstrates that analyte-centric molecular descriptors alone can capture meaningful structure-response relationships for a fixed CNT-DNA sensor. On the readout side, machine leaning can decode "hidden" information from full emission spectra of CNTs.[285] By treating entire spectra as high-dimensional inputs, machine learning models resolve subtle peak shifts, intensity ratios, and line-shape changes and effectively turn the emission profile into a rich fingerprint of nano–bio interfacial state, enabling sensitive and multiplexed detection of analytes. In summary, the above studies outline a general paradigm for AI-driven CNT–DNA biosensor design, especially, how to choose small but high-quality datasets to train machine leaning models. Extending this framework to broader nano–bio interfaces promises to accelerate the discovery of sensitive, selective, fast response, and interpretable biosensors beyond CNT–DNA systems.

6. Summary and outlook

Macroscopic sensing performances (sensitivity, LOD, specificity, selectivity, response time, multiplex, reproducibility and stability) of biosensors are ultimately connected to molecular scale interfacial parameters at nano–bio interfaces. Unraveling the relationship between macroscopic sensing performance and the molecular scale interfacial parameters is crucial for the rational design of biosensors. In this context, this review discussed why nano–bio interfaces are central to the bioreceptor–analyte interaction. The basic design rules for nano–bio interfaces facilitating the bioreceptor–analyte interaction are analyzed. Four key interfacial parameters, orientation, coverage, composition and spatial distribution of bioreceptor on nanoparticles, are elaborated to enhance the sensing performance of biosensors. Approaches to tailor these four interfacial parameters were summarized. In parallel, representative examples are presented to illustrate how rationally engineered nano–bio interfaces lead to the improved sensing performance.

Although much progress has been made in tailoring nano–bio interfaces, challenges still exist in the interfacial design to boost the analytical performance in nanoparticle-based biosensors. Compared with interfacial properties of bioreceptors on macro-substrates like electrodes, glass coverslip and metal film, the approaches to control the interfacial parameters on nanoparticles require further exploration. For instance, the conformation of DNA or protein on a planar substrate can be regulated by an external electric field, while relevant studies on the nanoparticle surface were rare.[218,286] Additionally, DNA nanostructures, nanoparticles and macromolecules all can serve as templates to control bioreceptor spacing on macro-substrates.[287] In contrast, due to the small size and high curvature of nanoparticles, the approach to control the inter-bioreceptor distance on nanoparticles is currently limited to transferring predefined patterns from DNA nanostructures. Except for finite nano–bio interface tailoring approaches, approaches to characterize the interfacial parameters of bioreceptors on particles are also limited, particularly at the single particle level.[288] Conventional characterization techniques, including UV-vis and fluorescence spectroscopy, FTIR, dynamic light scattering, mass spectrometry and SERS, are performed at the ensemble level, which conceals the heterogeneity of nano–bio interfaces.[239,289–291] TOF-SIMS, a highly sensitive surface analytical technique, is a powerful tool for interfacial characterization, enabling the assessment of conformation, surface coverage, spatial distribution of bioreceptor as well as chemical composition. The emerging single molecule techniques, such as DNA-PAINT, single molecule FRET, SERS and plasmonic scattering imaging, enable direct display of bioreceptors at a single particle.[237,238,292–294] Huge potential exists in investigating how the analytical performances of single particles are related to their interfacial parameters.[295] For instance, how can the spatial distribution of bioreceptors on nanoparticles be quantitatively and precisely characterized? Given the same average bioreceptor density on a nanoparticle, a uniform or heterogenous spatial distribution of bioreceptor, which one can result in superior sensing outcome? Addressing these questions is crucial not only for the rational design of nano–bio interfaces but also for the stability and reproducibility of nanoparticle-based biosensors. Therefore, developing novel and facile approaches to tailor and characterize the nano–bio interfaces is required.

Another challenge is elucidating how various interfacial parameters correlate with multiple sensing metrics, a task requiring multivariate regression analysis. Additionally, experimental investigations of nano–bio interfaces, in certain cases, are difficult to implement as a multitude of interrelated variables must be simultaneously considered. For instance, variations in bioreceptor coverage on nanoparticles may be accompanied by

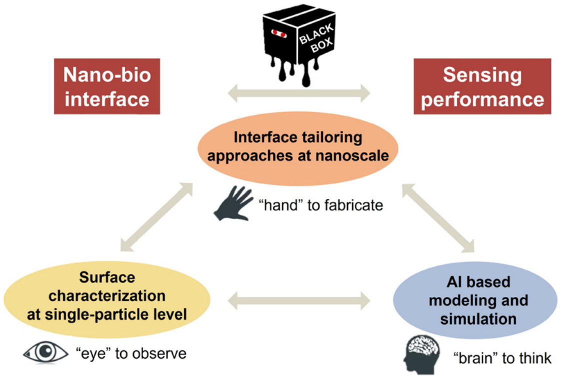

Fig. 20 Key aspects of nano–bio interfacial design for high-performance nanoparticle-based biosensors.

concomitant changes in conformation and spatial distribution of bioreceptors. In this regard, AI-based modeling and simulation approaches are tremendously valuable, as they enable systematic exploration of numerous parameter permutations. Xu and coworkers developed a model of predicting DNA arrangement on AuNPs to achieve the optimal detecting activity of human telomerase.[296] Key parameters, including the size of nanoparticles, spacing of probe DNA and distance between two catalytic pockets of telomerase, were incorporated in this model. The optimal DNA density obtained from the experiment matched well with the value from the model. The LOD of AuNPs–DNA conjugates with optimal DNA density was at least 1 order of magnitude lower than that of densely packed AuNPs, demonstrating the effectiveness of this model in guiding interfacial probe arrangement. Similarly, Sun and coworkers used atomistic MD simulation to optimize receptor structure and favourable binding-site on AuNPs.[297] The binding between receptors and guests requires deep penetration of guests into the monolayer of receptors. Receptor design guided by the simulation exhibited 10-fold improvement in analyte affinity and a 100-fold decrease in LOD. With rapid advances in AI-based modeling and simulation, these approaches are expected to be extended to a broader range of nanoparticles and bioreceptors, playing an increasingly significant role in the design and optimization of nanoparticle-based biosensors.

In summary, this review dismantles the traditional ''black box'' of nanoparticle-based biosensors by systematically elucidating the intrinsic relationships between nano–bio interfaces and sensing performances (Fig. 20). The proposed closed-loop framework integrates three aspects: (1) nano–bio interface tailoring approaches, serving as the hand for fabrication; (2) nano–bio interface characterization at the single particle level, acting as the eye for direct observation; and (3) AI-driven modelling and simulation, working as the brain for rational analysis. We hope that this review can contribute to a deeper understanding of the pivotal role of the nano–bio interface in determining biosensing performances. Ongoing advances in customizing and characterizing the nano–bio interfaces, particularly at the single particle level, along with AI modelling and simulations, are poised to unlock profound insights into nano–bio interfaces and drive the development of next-generation nanoparticle-based biosensors with outstanding performance.

Conflicts of interest

There are no conflicts to declare.

Data availability

No primary data were used in the writing of this review paper and all data and information were sourced from the published literature.

Acknowledgements

We acknowledge funding from the Australian Research Council Discovery Grant (DP250101047) and Industry Laureate Fellowship Programs (IL24010091) National Health and Medical Research Council Investigator Grant (GNT1196648), China Postdoctoral Science Foundation (2023M743164) and Youth Science Foundation of Henan Province (252300423738). We also thank Professor Chao Lu for his kind support.

Notes and references

1 Y. Wu, D. Bennett, R. D. Tilley and J. J. Gooding, *Adv. Mater.*, 2019, **32**, 1904339.
2 H. Geng, S. Vilms Pedersen, Y. Ma, T. Haghighi, H. Dai, P. D. Howes and M. M. Stevens, *Acc. Chem. Res.*, 2022, **55**, 593–604.
3 Z. Gao, Y. Song, T. Y. Hsiao, J. He, C. Wang, J. Shen, A. MacLachlan, S. Dai, B. H. Singer, K. Kurabayashi and P. Chen, *ACS Nano*, 2021, **15**, 18023–18036.
4 Z. Li, M. Guo and W. Zhong, *Precis. Chem.*, 2025, **3**, 297–318.
5 L. Gloag, M. Mehdipour, D. Chen, R. D. Tilley and J. J. Gooding, *Adv. Mater.*, 2019, **31**, 1904385.
6 D. Chen, Y. Wu, S. Hoque, R. D. Tilley and J. J. Gooding, *Chem. Sci.*, 2021, **12**, 5196–5201.
7 Z. Farka, T. Juřík, D. Kovář, L. Trnková and P. Skládal, *Chem. Rev.*, 2017, **117**, 9973–10042.
8 J. Zhang, L. Mou and X. Jiang, *Chem. Sci.*, 2020, **11**, 923–936.
9 J. J. Gooding and S. Ciampi, *Chem. Soc. Rev.*, 2011, **40**, 2704–2718.
10 F. Yang, X. Zuo, C. Fan and X. Zhang, *Natl. Sci. Rev.*, 2018, **5**, 740–755.
11 R. Pardehkhorram and A. Andrieu-Brunsen, *Chem. Commun.*, 2022, **58**, 5188–5204.
12 M. Singh, N. Kaur and E. Comini, *J. Mater. Chem. C*, 2020, **8**, 3938–3955.
13 K. Bhattacharjee and B. L. V. Prasad, *Chem. Soc. Rev.*, 2023, **52**, 2573–2595.

14 L. Taiariol, C. Chaix, C. Farre and E. Moreau, *Chem. Rev.*, 2022, **122**, 340–384.

15 K. E. Sapsford, W. R. Algar, L. Berti, K. B. Gemmill, B. J. Casey, E. Oh, M. H. Stewart and I. L. Medintz, *Chem. Rev.*, 2013, **113**, 1904–2074.

16 P. Li, G.-H. Lee, S. Y. Kim, S. Y. Kwon, H.-R. Kim and S. Park, *ACS Nano*, 2021, **15**, 1960–2004.

17 H. Zhou, J. Liu, J.-J. Xu, S.-S. Zhang and H.-Y. Chen, *Chem. Soc. Rev.*, 2018, **47**, 1996–2019.

18 Y. Cao, L. Zhou, Z. Fang, Z. Zou, J. Zhao, X. Zuo and G. Li, *Chem. Commun.*, 2023, **59**, 3383–3398.

19 C. J. Yang, S. Jockusch, M. Vicens, N. J. Turro and W. Tan, *Proc. Natl. Acad. Sci. U. S. A.*, 2005, **102**, 17278.

20 S. O. Kelley, C. A. Mirkin, D. R. Walt, R. F. Ismagilov, M. Toner and E. H. Sargent, *Nat. Nanotechnol.*, 2014, **9**, 969–980.

21 K. B. Cederquist and C. D. Keating, *Langmuir*, 2010, **26**, 18273–18280.

22 C. Chen, W. Wang, J. Ge and X. S. Zhao, *Nucleic Acids Res.*, 2009, **37**, 3756–3765.

23 A. K. R. Lytton-Jean and C. A. Mirkin, *J. Am. Chem. Soc.*, 2005, **127**, 12754–12755.

24 L. K. Fong, Z. Wang, G. C. Schatz, E. Luijten and C. A. Mirkin, *J. Am. Chem. Soc.*, 2018, **140**, 6226–6230.

25 E. Treasurer and R. Levicky, *J. Phys. Chem. B*, 2021, **125**, 2976–2986.

26 A. Sedighi, P. C. H. Li, I. C. Pekcevik and B. D. Gates, *ACS Nano*, 2014, **8**, 6765–6777.

27 Q. Gu, E. A. Josephs and T. Ye, *Aggregate*, 2022, e186.

28 Q. Gu, H. H. Cao, Y. Zhang, H. Wang, Z. J. Petrek, F. Shi, E. A. Josephs and T. Ye, *ACS Sens.*, 2021, **6**, 371–379.

29 S. Dey, R. Rivas-Barbosa, F. Sciortino, E. Zaccarelli and P. Zijlstra, *Nanoscale*, 2024, **16**, 4872–4879.

30 Z. Xia, E. Villarreal, H. Wang and B. L. T. Lau, *Colloids Surf., B*, 2020, **190**, 110960.

31 S. R. Saptarshi, A. Duschl and A. L. Lopata, *J. Nanobiotechnol.*, 2013, **11**, 26.

32 K. B. Cederquist and C. D. Keating, *ACS Nano*, 2009, **3**, 256–260.

33 H. D. Hill, J. E. Millstone, M. J. Banholzer and C. A. Mirkin, *ACS Nano*, 2009, **3**, 418–424.

34 R. Münter, C. Stavnsbjerg, E. Christensen, M. E. Thomsen, A. Stensballe, A. E. Hansen, L. Parhamifar, K. Kristensen, J. B. Simonsen, J. B. Larsen and T. L. Andresen, *Small*, 2022, **18**, 2106529.

35 S. Tenzer, D. Docter, J. Kuharev, A. Musyanovych, V. Fetz, R. Hecht, F. Schlenk, D. Fischer, K. Kiouptsi, C. Reinhardt, K. Landfester, H. Schild, M. Maskos, S. K. Knauer and R. H. Stauber, *Nat. Nanotechnol.*, 2013, **8**, 772–781.

36 M. Mahmoudi, M. P. Landry, A. Moore and R. Coreas, *Nat. Rev. Mater.*, 2023, **8**, 422–438.

37 J. H. Monserud and D. K. Schwartz, *ACS Nano*, 2014, **8**, 4488–4499.

38 M. Oishi and K. Saito, *ACS Nano*, 2020, **14**, 3477–3489.

39 J. Yang, X. Li, B. Jiang, R. Yuan and Y. Xiang, *Anal. Chem.*, 2020, **92**, 7893–7899.

40 B. C. Lagerholm and N. L. Thompson, *Biophys. J.*, 1998, **74**, 1215–1228.

41 J. C. Traeger, Z. Lamberty and D. K. Schwartz, *ACS Nano*, 2019, **13**, 7850–7859.

42 S. Hwu, Y. Blickenstorfer, S. J. Ihle, M. Garzuel, C. Forró, L. Schmidheini, L. Demkó and J. Vörös, *J. Phys. Chem. C*, 2020, **124**, 1566–1574.

43 C. Qiao, J. Wu, Z. Huang, X. Cao, J. Liu, B. Xiong, Y. He and E. S. Yeung, *Anal. Chem.*, 2017, **89**, 5592–5597.

44 Y. Chen, S. Sun, X. Liu, H. Li, S. Huan, B. Xiong and X.-B. Zhang, *Anal. Chem.*, 2024, **96**, 9551–9560.

45 S. J. Hurst, H. D. Hill and C. A. Mirkin, *J. Am. Chem. Soc.*, 2008, **130**, 12192–12200.

46 A. K. Pearce, T. R. Wilks, M. C. Arno and R. K. O'Reilly, *Nat. Rev. Chem.*, 2021, **5**, 21–45.

47 J. M. Rabanel, V. Adibnia, S. F. Tehrani, S. Sanche, P. Hildgen, X. Banquy and C. Ramassamy, *Nanoscale*, 2019, **11**, 383–406.

48 P. De Luna, S. S. Mahshid, J. Das, B. Luan, E. H. Sargent, S. O. Kelley and R. Zhou, *Nano Lett.*, 2017, **17**, 1289–1295.

49 Z. Shen, P. L. Xavier, R. Bean, J. Bielecki, M. Bergemann, B. J. Daurer, T. Ekeberg, A. D. Estillore, H. Fangohr, K. Giewekemeyer, M. Karnevskiy, R. A. Kirian, H. Kirkwood, Y. Kim, J. C. P. Koliyadu, H. Lange, R. Letrun, J. Lübke, A. Mall, T. Michelat, A. J. Morgan, N. Roth, A. K. Samanta, T. Sato, M. Sikorski, F. Schulz, P. Vagovic, T. Wollweber, L. Worbs, F. Maia, D. A. Horke, J. Küpper, A. P. Mancuso, H. N. Chapman, K. Ayyer and N. D. Loh, *ACS Nano*, 2024, **18**, 15576–15589.

50 M. Horáček, R. E. Armstrong and P. Zijlstra, *Langmuir*, 2018, **34**, 131–138.

51 M. R. W. Scheepers, I. L. J. Van and M. W. J. Prins, *Langmuir*, 2019, **35**, 14272–14281.

52 C. M. Platnich, F. J. Rizzuto, G. Cosa and H. F. Sleiman, *Chem. Soc. Rev.*, 2020, **49**, 4220–4233.

53 C. C. Harper, J. S. Jordan, S. Papanu and E. R. Williams, *ACS Nano*, 2024, **18**, 17806–17814.

54 J. E. Park, Y. Jung, M. Kim and J. M. Nam, *ACS Cent. Sci.*, 2018, **4**, 1303–1314.

55 R. M. Lubken, A. M. de Jong and M. W. J. Prins, *ACS Nano*, 2021, **15**, 1331–1341.

56 A. Makaraviciute and A. Ramanaviciene, *Biosens. Bioelectron.*, 2013, **50**, 460–471.

57 F. M. Kelley, A. Ani, E. G. Pinlac, B. Linders, B. Favetta, M. Barai, Y. Ma, A. Singh, G. L. Dignon, Y. Gu and B. S. Schuster, *Nat. Commun.*, 2025, **16**, 3521.

58 M. Tonigold, J. Simon, D. Estupiñán, M. Kokkinopoulou, J. Reinholz, U. Kintzel, A. Kaltbeitzel, P. Renz, M. P. Domogalla, K. Steinbrink, I. Lieberwirth, D. Crespy, K. Landfester and V. Mailänder, *Nat. Nanotechnol.*, 2018, **13**, 862–869.

59 Y. Tang, X. Zhao, Z. Nie, B. He and D. Deng, *ACS Appl. Bio Mater.*, 2025, **8**, 6252–6260.

60 B.-K. Jin, S. Odongo, M. Radwanska and S. Magez, *Int. J. Mol. Sci.*, 2023, **24**, 5994.

61 V. Mora-Sanz, L. Saa, N. Briz, M. Möller and V. Pavlov, *ACS Appl. Mater. Interfaces*, 2020, **12**, 28993–28999.

62 Q. Yu, Q. Wang, B. Li, Q. Lin and Y. Duan, *Crit. Rev. Anal. Chem.*, 2015, **45**, 62–75.

63 A. J. Sivaram, A. Wardiana, C. B. Howard, S. M. Mahler and K. J. Thurecht, *Adv. Healthcare Mater.*, 2018, **7**, 1700607.

64 Z. Pei, H. Anderson, A. Myrskog, G. Dunér, B. Ingemarsson and T. Aastrup, *Anal. Biochem.*, 2010, **398**, 161–168.

65 D. Lou, L. Ji, L. Fan, Y. Ji, N. Gu and Y. Zhang, *Langmuir*, 2019, **35**, 4860–4867.

66 C. Parolo, A. de la Escosura-Muñiz, E. Polo, V. Grazú, J. M. de la Fuente and A. Merkoçi, *ACS Appl. Mater. Interfaces*, 2013, **5**, 10753–10759.

67 G. Ruiz, K. Tripathi, S. Okyem and J. D. Driskell, *Bioconjugate Chem.*, 2019, **30**, 1182–1191.

68 O. S. Wolfbeis, *Chem. Soc. Rev.*, 2015, **44**, 4743–4768.

69 L. Zhang, Y. Mazouzi, M. Salmain, B. Liedberg and S. Boujday, *Biosens. Bioelectron.*, 2020, **165**, 112370.

70 M. Park, *BioChip J.*, 2019, **13**, 82–94.

71 A. A. Karyakin, G. V. Presnova, M. Y. Rubtsova and A. M. Egorov, *Anal. Chem.*, 2000, **72**, 3805–3811.

72 H. Sharma and R. Mutharasan, *Anal. Chem.*, 2013, **85**, 2472–2477.

73 S. Wu, H. Liu, X. M. Liang, X. Wu, B. Wang and Q. Zhang, *Anal. Chem.*, 2014, **86**, 4271–4277.

74 T. Nan, S. Wu, H. Zhao, W. Tan, Z. Li, Q. Zhang and B. Wang, *Anal. Chem.*, 2012, **84**, 4327–4333.

75 J. Sun, L. Li, R. Sun, H. Yin and J. Liu, *Anal. Chem.*, 2025, **97**, 16515–16524.

76 S. Gao, J. M. Guisán and J. Rocha-Martin, *Anal. Chim. Acta*, 2022, **1189**, 338907.

77 S. K. Vashist, E. Lam, S. Hrapovic, K. B. Male and J. H. T. Luong, *Chem. Rev.*, 2014, **114**, 11083–11130.

78 L. Hu, Z. Chen, T. Li, X. Ye, Q. Luo and W. Lai, *Food Chem.*, 2023, **429**, 136816.

79 L. Cohen and D. R. Walt, *Bioconjugate Chem.*, 2018, **29**, 3452–3458.

80 I.-H. Cho, E.-H. Paek, H. Lee, J. Y. Kang, T. S. Kim and S.-H. Paek, *Anal. Biochem.*, 2007, **365**, 14–23.

81 E. von Witting, S. Hober and S. Kanje, *Bioconjugate Chem.*, 2021, **32**, 1515–1524.

82 J. M. Bolivar and B. Nidetzky, *Biochim. Biophys. Acta, Proteins Proteomics*, 2020, **1868**, 140333.

83 W. Ma, A. Saccardo, D. Roccatano, D. Aboagye-Mensah, M. Alkaseem, M. Jewkes, F. Di Nezza, M. Baron, M. Soloviev and E. Ferrari, *Nat. Commun.*, 2018, **9**, 1489.

84 A. H. Keeble, A. Banerjee, M. P. Ferla, S. C. Reddington, I. Anuar and M. Howarth, *Angew. Chem., Int. Ed.*, 2017, **56**, 16521–16525.

85 K. Guo, S. Wustoni, A. Koklu, E. Díaz-Galicia, M. Moser, A. Hama, A. A. Alqahtani, A. N. Ahmad, F. S. Alhamlan, M. Shuaib, A. Pain, I. McCulloch, S. T. Arold, R. Grünberg and S. Inal, *Nat. Biomed. Eng.*, 2021, **5**, 666–677.

86 G. P. Anderson, J. L. Liu, L. C. Shriver-Lake, D. Zabetakis, V. A. Sugiharto, H.-W. Chen, C.-R. Lee, G. N. Defang, S.-J. L. Wu, N. Venkateswaran and E. R. Goldman, *Anal. Chem.*, 2019, **91**, 9424–9429.

87 S. Kim, Y. Ahn, Y. Bae, S. Woo, J. Park, I. K. Han, H. Kim, S. Eom, S. Kang, W. Jung and J. Park, *Biosens. Bioelectron.*, 2022, **213**, 114441.

88 C. Albert, L. Bracaglia, A. Koide, J. DiRito, T. Lysyy, L. Harkins, C. Edwards, O. Richfield, J. Grundler and K. Zhou, *Nat. Commun.*, 2022, **13**, 5998.

89 N. G. Welch, J. A. Scoble, B. W. Muir and P. J. Pigram, *Biointerphases*, 2017, **12**, 02D301.

90 S. Y. Gan, G. J. Tye, A. L. Chew, W. K. Ng and N. S. Lai, *Biosens. Bioelectron.: X*, 2023, **14**, 100379.

91 S. Huang, W. Wang, J. Li, T. Zhang, Y. Liang, Q. Wang and Z. Jiang, *Chem. Eng. J.*, 2021, **419**, 129613.

92 X. Chen, Y. Huang, S. Yang, S. Wang, L. Chen, X. Yu, N. Gan and S. Huang, *Biosens. Bioelectron.*, 2024, **266**, 116738.

93 K. Alt, F. Carraro, E. Jap, M. Linares-Moreau, R. Riccò, M. Righetto, M. Bogar, H. Amenitsch, R. A. Hashad, C. Doonan, C. E. Hagemeyer and P. Falcaro, *Adv. Mater.*, 2022, **34**, 2106607.

94 Q. Zhang, J. Liang, A. Bongers, J. J. Richardson, K. Liang and Z. Gu, *Adv. Sci.*, 2023, **10**, 2206546.

95 G. Tian, Z. Zhou, M. Li, X. Li, T. Xu and X. Zhang, *Anal. Chem.*, 2023, **95**, 13250–13257.

96 Q.-Q. Zhuang, H.-H. Deng, S.-B. He, H.-P. Peng, Z. Lin, X.-H. Xia and W. Chen, *ACS Appl. Mater. Interfaces*, 2019, **11**, 31729–31734.

97 G. Hong, C. Su, Z. Huang, Q. Zhuang, C. Wei, H. Deng, W. Chen and H. Peng, *Anal. Chem.*, 2021, **93**, 13022–13028.

98 X. Chen, C. Su, Y. Yang, Z. Weng, Q. Zhuang, G. Hong, H. Peng and W. Chen, *Anal. Chem.*, 2025, **97**, 872–879.

99 H. Pei, X. Zuo, D. Pan, J. Shi, Q. Huang and C. Fan, *NPG Asia Mater.*, 2013, **5**, e51–e51.

100 B. Liu, Z. Huang and J. Liu, *Angew. Chem., Int. Ed.*, 2018, **57**, 9439–9442.

101 Q. He, Q. Wu, X. Feng, Z. Liao, W. Peng, Y. Liu, D. Peng, Z. Liu and M. Mo, *Int. J. Biol. Macromol.*, 2020, **151**, 757–780.

102 S. Stangherlin and J. Liu, *J. Mater. Chem. B*, 2023, **11**, 6994–7003.

103 X. Zhang, M. R. Servos and J. Liu, *Langmuir*, 2012, **28**, 3896–3902.

104 B. Liu and J. Liu, *Matter*, 2019, **1**, 825–847.

105 J. I. Cutler, E. Auyeung and C. A. Mirkin, *J. Am. Chem. Soc.*, 2012, **134**, 1376–1391.

106 H. Kimura-Suda, D. Y. Petrovykh, M. J. Tarlov and L. J. Whitman, *J. Am. Chem. Soc.*, 2003, **125**, 9014–9015.

107 H. Pei, F. Li, Y. Wan, M. Wei, H. Liu, Y. Su, N. Chen, Q. Huang and C. Fan, *J. Am. Chem. Soc.*, 2012, **134**, 11876–11879.

108 D. Zhu, P. Song, J. Shen, S. Su, J. Chao, A. Aldalbahi, Z. Zhou, S. Song, C. Fan, X. Zuo, Y. Tian, L. Wang and H. Pei, *Anal. Chem.*, 2016, **88**, 4949–4954.

109 C.-Y. Lee, P. Gong, G. M. Harbers, D. W. Grainger, D. G. Castner and L. J. Gamble, *Anal. Chem.*, 2006, **78**, 3316–3325.

110 S. Choi and Y. S. Nam, *Biosens. Bioelectron.*, 2022, **210**, 114288.
111 A. Dillen, C. Scarpellini, W. Daenen, S. Driesen, P. Zijlstra and J. Lammertyn, *ACS Sens.*, 2023, **8**, 811–821.
112 R. Levicky, T. M. Herne, M. J. Tarlov and S. K. Satija, *J. Am. Chem. Soc.*, 1998, **120**, 9787–9792.
113 P. Liang, J. Canoura, H. Yu, O. Alkhamis and Y. Xiao, *ACS Appl. Mater. Interfaces*, 2018, **10**, 4233–4242.
114 B. Liu, P. Wu, Z. Huang, L. Ma and J. Liu, *J. Am. Chem. Soc.*, 2018, **140**, 4499–4502.
115 T. L. Halo, K. M. McMahon, N. L. Angeloni, Y. Xu, W. Wang, A. B. Chinen, D. Malin, E. Strekalova, V. L. Cryns, C. Cheng, C. A. Mirkin and C. S. Thaxton, *Proc. Natl. Acad. Sci. U. S. A.*, 2014, **111**, 17104–17109.
116 B. Liu, T. Wu, Z. Huang, Y. Liu and J. Liu, *Angew. Chem., Int. Ed.*, 2019, **58**, 2109–2113.
117 B. Liu and J. Liu, *Langmuir*, 2019, **35**, 6476–6482.
118 Z. Li, Y. Lv, X. Duan, B. Liu and Y. Zhao, *Angew. Chem., Int. Ed.*, 2023, **62**, e202312975.
119 S. Shi, J. Chen, X. Wang, M. Xiao, A. R. Chandrasekaran, L. Li, C. Yi and H. Pei, *Adv. Funct. Mater.*, 2022, **32**, 2201069.
120 J. Su, W. Liu, S. Chen, W. Deng, Y. Dou, Z. Zhao, J. Li, Z. Li, H. Yin, X. Ding and S. Song, *ACS Sens.*, 2020, **5**, 3979–3987.
121 F. Li, X. Mao, F. Li, M. Li, J. Shen, Z. Ge, C. Fan and X. Zuo, *J. Am. Chem. Soc.*, 2020, **142**, 9975–9981.
122 M. Li, L. Song, M. Liu, R. Guo, M. Lin and X. Zuo, *ACS Nano*, 2025, **19**, 23142–23150.
123 R. T. Busch, F. Karim, J. Weis, Y. Sun, C. Zhao and E. S. Vasquez, *ACS Omega*, 2019, **4**, 15269–15279.
124 D. A. Cowan and R. Fernandez-Lafuente, *Enzyme Microb. Technol.*, 2011, **49**, 326–346.
125 P. Ghisellini, M. Caiazzo, A. Alessandrini, R. Eggenhöffner, M. Vassalli and P. Facci, *Sci. Rep.*, 2016, **6**, 37779.
126 H. J. Kim, D. Park, Y. Park, D.-H. Kim and J. Kim, *Nano Lett.*, 2022, **22**, 6537–6544.
127 E. A. Josephs and T. Ye, *Nano Lett.*, 2012, **12**, 5255–5261.
128 K. Abstiens, M. Gregoritza and A. M. Goepferich, *ACS Appl. Mater. Interfaces*, 2019, **11**, 1311–1320.
129 Y. Cao, J. Wu, X. Zheng, Y. Lu, J. A. Piper, Y. Lu and N. H. Packer, *Anal. Chim. Acta*, 2022, **1209**, 339863.
130 B. Saha, T. H. Evers and M. W. J. Prins, *Anal. Chem.*, 2014, **86**, 8158–8166.
131 X. Chen, F. Lisi, P. Bakthavathsalam, G. Longatte, S. Hoque, R. D. Tilley and J. J. Gooding, *ACS Sens.*, 2021, **6**, 538–545.
132 J. Zhang, F. Chai, J. A. Li, S. Wang, S. Zhang, F. Li, A. Liang, A. Luo, D. Wang and X. Jiang, *Sci. Adv.*, 2024, **10**, eadn5698.
133 X. Qu, D. Zhu, G. Yao, S. Su, J. Chao, H. Liu, X. Zuo, L. Wang, J. Shi, L. Wang, W. Huang, H. Pei and C. Fan, *Angew. Chem., Int. Ed.*, 2017, **56**, 1855–1858.
134 J. Li, B. Zhu, X. Yao, Y. Zhang, Z. Zhu, S. Tu, S. Jia, R. Liu, H. Kang and C. J. Yang, *ACS Appl. Mater. Interfaces*, 2014, **6**, 16800–16807.
135 G. Hirao, N. Fukuzumi, A. Ogawa, T. Asahi, M. Mizuo and T. Zako, *RSC Adv.*, 2023, **13**, 30690–30695.
136 Y. Tanaka, G. Hirao, N. Fukuzumi, T. Asahi, M. Maeda, A. Ogawa and T. Zako, *Langmuir*, 2025, **41**, 4560–4568.
137 N. Fukuzumi, G. Hirao, A. Ogawa, T. Asahi, M. Maeda and T. Zako, *Sci. Rep.*, 2025, **15**, 8222.
138 G. Wang, Z. Li and N. Ma, *ACS Chem. Bio.*, 2018, **13**, 1705–1713.
139 M. P. Busson, B. Rolly, B. Stout, N. Bonod, E. Larquet, A. Polman and S. Bidault, *Nano Lett.*, 2011, **11**, 5060–5065.
140 M.-X. Li, C.-H. Xu, N. Zhang, G.-S. Qian, W. Zhao, J.-J. Xu and H.-Y. Chen, *ACS Nano*, 2018, **12**, 3341–3350.
141 H. Xing, Y. Bai, Y. Bai, L. H. Tan, J. Tao, B. Pedretti, G. A. Vincil, Y. Lu and S. C. Zimmerman, *J. Am. Chem. Soc.*, 2017, **139**, 3623–3626.
142 M. Colombo, L. Fiandra, G. Alessio, S. Mazzucchelli, M. Nebuloni, C. De Palma, K. Kantner, B. Pelaz, R. Rotem and F. Corsi, *Nat. Commun.*, 2016, **7**, 1–14.
143 H. Wang, Y. Li, M. Liu, M. Gong and Z. Deng, *Small*, 2015, **11**, 2247–2251.
144 N. T. Emerson and H. Yang, *J. Am. Chem. Soc.*, 2022, **144**, 12915–12923.
145 D. Zanchet, C. M. Micheel, W. J. Parak, D. Gerion and A. P. Alivisatos, *Nano Lett.*, 2001, **1**, 32–35.
146 S. E. Lee, Q. Chen, R. Bhat, S. Petkiewicz, J. M. Smith, V. E. Ferry, A. L. Correia, A. P. Alivisatos and M. J. Bissell, *Nano Lett.*, 2015, **15**, 4564–4570.
147 G. Tikhomirov, S. Hoogland, P. E. Lee, A. Fischer, E. H. Sargent and S. O. Kelley, *Nat. Nanotechnol.*, 2011, **6**, 485–490.
148 N. Ma, E. H. Sargent and S. O. Kelley, *Nat. Nanotechnol.*, 2009, **4**, 121–125.
149 X. He, Z. Li, M. Chen and N. Ma, *Angew. Chem., Int. Ed.*, 2014, **53**, 14447–14450.
150 J. Shen, Q. Tang, L. Li, J. Li, X. Zuo, X. Qu, H. Pei, L. Wang and C. Fan, *Angew. Chem., Int. Ed.*, 2017, **56**, 16077–16081.
151 G. Yao, J. Li, Q. Li, X. Chen, X. Liu, F. Wang, Z. Qu, Z. Ge, R. P. Narayanan, D. Williams, H. Pei, X. Zuo, L. Wang, H. Yan, B. L. Feringa and C. Fan, *Nat. Mater.*, 2020, **19**, 781–788.
152 G. Yao, H. Pei, J. Li, Y. Zhao, D. Zhu, Y. Zhang, Y. Lin, Q. Huang and C. Fan, *NPG Asia Mater.*, 2015, **7**, e159.
153 X. Chen, X. Liu, G. Yao, Q. Li, R. Liu, H. Wu, Y. Lv, C. Fan, L. Wang and J. Li, *NPG Asia Mater.*, 2020, **12**, 49.
154 D. Fan, J. Wang, E. Wang and S. Dong, *Adv. Sci.*, 2020, **7**, 2001766.
155 L. Yu and H. Yan, *Nat. Biomed. Eng.*, 2023, **7**, 1535–1536.
156 K. B. Johnsen, M. Bak, F. Melander, M. S. Thomsen, A. Burkhart, P. J. Kempen, T. L. Andresen and T. Moos, *J. Controlled Release*, 2019, **295**, 237–249.
157 D. J. Nieves, N. S. Azmi, R. Xu, R. Lévy, E. A. Yates and D. G. Fernig, *Chem. Commun.*, 2014, **50**, 13157–13160.
158 H. Choi and Y. Jung, *Chem. Sci.*, 2022, **13**, 7552–7559.
159 O. Zeiri, *ACS Sens.*, 2020, **5**, 3806–3820.
160 N. Dridi, Z. Jin, W. Perng and H. Mattoussi, *ACS Nano*, 2024, **18**, 8649–8662.
161 M. Zheng and X. Huang, *J. Am. Chem. Soc.*, 2004, **126**, 12047–12054.

162 J. Baggerman, M. M. J. Smulders and H. Zuilhof, *Langmuir*, 2019, **35**, 1072–1084.

163 S. Lowe, N. M. O'Brien-Simpson and L. A. Connal, *Polym. Chem.*, 2015, **6**, 198–212.

164 C. Jiang, G. Wang, R. Hein, N. Liu, X. Luo and J. J. Davis, *Chem. Rev.*, 2020, **120**, 3852–3889.

165 A. K. Nowinski, F. Sun, A. D. White, A. J. Keefe and S. Jiang, *J. Am. Chem. Soc.*, 2012, **134**, 6000–6005.

166 C. Sanchez-Cano and M. Carril, *Int. J. Mol. Sci.*, 2020, **21**, 1007.

167 C. Guo, H. Ding, M. Xie, H. Zhang, X. Hong, L. Sun and F. Ding, *Colloids Surf., A*, 2021, **615**, 126155.

168 Q. Dai, C. Walkey and W. C. Chan, *Angew. Chem., Int. Ed.*, 2014, **53**, 5093–5096.

169 M. Chen, R. Han, W. Wang, Y. Li and X. Luo, *Anal. Chem.*, 2021, **93**, 13555–13563.

170 S. Zhao, X. Qiao, M. Chen, Y. Li, X. Wang, Z. Xu, Y. Wu and X. Luo, *ACS Sens.*, 2022, **7**, 1740–1746.

171 R. Han, Y. Li, W. Hou, C. Ding and X. Luo, *Anal. Chem.*, 2023, **95**, 9025–9033.

172 R. Han, Y. Li, W. Wang, C. Ding, J. J. Davis and X. Luo, *Anal. Chem.*, 2024, **96**, 15511–15517.

173 Z. Zhang, Y. Wen, Y. Ma, J. Luo, L. Jiang and Y. Song, *Chem. Commun.*, 2011, **47**, 7407–7409.

174 L. Xu, W. Yan, W. Ma, H. Kuang, X. Wu, L. Liu, Y. Zhao, L. Wang and C. Xu, *Adv. Mater.*, 2015, **27**, 1706–1711.

175 H. D. Hill and C. A. Mirkin, *Nat. Protoc.*, 2006, **1**, 324–336.

176 Y. Wang, X. Liu, L. Wu, L. Ding, C. Y. Effah, Y. Wu, Y. Xiong and L. He, *Biosens. Bioelectron.*, 2022, **195**, 113661.

177 Q. Zhang, R. Ma, Y. Zhang, J. Zhao, Y. Wang and Z. Xu, *ACS Sens.*, 2023, **8**, 875–883.

178 C. Li, S. Yang, R. Li, S. Gong, M. Huang, Y. Sun, G. Xiong, D. Wu, M. Ji, Y. Chen, C. Gao and Y. Yu, *ACS Appl. Mater. Interfaces*, 2022, **14**, 7646–7658.

179 H. Shen, X. Zheng, Z. Zhou, W. He, M. Li, P. Su, J. Song and Y. Yang, *J. Mater. Chem. B*, 2020, **8**, 8467–8475.

180 G.-B. Chu, W.-Y. Li, X.-X. Han, H.-H. Sun, Y. Han, G.-Y. Zhi and D.-H. Zhang, *Small*, 2023, **19**, 2301413.

181 Y. Zhang, L. Xu and J. Ge, *Nano Lett.*, 2022, **22**, 5029–5036.

182 T. Man, C. Xu, X.-Y. Liu, D. Li, C.-K. Tsung, H. Pei, Y. Wan and L. Li, *Nat. Commun.*, 2022, **13**, 305.

183 L. Wang, Y. Zhu, L. Xu, W. Chen, H. Kuang, L. Liu, A. Agarwal, C. Xu and N. A. Kotov, *Angew. Chem., Int. Ed.*, 2010, **49**, 5472–5475.

184 L. Xu, H. Kuang, C. Xu, W. Ma, L. Wang and N. A. Kotov, *J. Am. Chem. Soc.*, 2012, **134**, 1699–1709.

185 S.-Y. Ding, J. Yi, J.-F. Li, B. Ren, D.-Y. Wu, R. Panneerselvam and Z.-Q. Tian, *Nat. Rev. Mater.*, 2016, **1**, 16021.

186 R. Pardehkhorram, S. Bonaccorsi, H. Zhu, V. R. Gonçales, Y. Wu, J. Liu, N. A. Lee, R. D. Tilley and J. J. Gooding, *Chem. Commun.*, 2019, **55**, 7707–7710.

187 R. Pardehkhorram, F. A. Alshawawreh, V. R. Gonçales, N. A. Lee, R. D. Tilley and J. J. Gooding, *Anal. Chem.*, 2021, **93**, 12954–12965.

188 G. Wang, Y. Akiyama, N. Kanayama, T. Takarada and M. Maeda, *Small*, 2017, **13**, 1702137.

189 E. E. Coughlin, J. Hu, A. Lee and T. W. Odom, *J. Am. Chem. Soc.*, 2021, **143**, 3671–3676.

190 Z. Yang, X. Peng, P. Yang, Y. Zhuo, Y.-Q. Chai, W. Liang and R. Yuan, *Chem. Sci.*, 2020, **11**, 8482–8488.

191 A. Escarpa and B. Jurado-Sánchez, *Anal. Chem.*, 2025, **97**, 12913–12924.

192 M. Pacheco, B. Jurado-Sánchez and A. Escarpa, *Anal. Chem.*, 2018, **90**, 2912–2917.

193 K. Yuan, C. Cuntín-Abal, B. Jurado-Sánchez and A. Escarpa, *Anal. Chem.*, 2021, **93**, 16385–16392.

194 K. Yuan, B. Jurado-Sánchez and A. Escarpa, *Angew. Chem., Int. Ed.*, 2021, **60**, 4915–4924.

195 X. Liu, F. Zhang, X. Jing, M. Pan, P. Liu, W. Li, B. Zhu, J. Li, H. Chen, L. Wang, J. Lin, Y. Liu, D. Zhao, H. Yan and C. Fan, *Nature*, 2018, **559**, 593–598.

196 S. Wang, Z. Zhou, N. Ma, S. Yang, K. Li, C. Teng, Y. Ke and Y. Tian, *Sensors*, 2020, **20**, 6899.

197 S. Fu, T. Zhang, H. Jiang, Y. Xu, J. Chen, L. Zhang and X. Su, *TrAC, Trends Anal. Chem.*, 2021, **140**, 116267.

198 Q. Liu, Z. Ge, X. Mao, G. Zhou, X. Zuo, J. Shen, J. Shi, J. Li, L. Wang, X. Chen and C. Fan, *Angew. Chem., Int. Ed.*, 2018, **57**, 7131–7135.

199 C. Chen, X. Wei, M. F. Parsons, J. Guo, J. L. Banal, Y. Zhao, M. N. Scott, G. S. Schlau-Cohen, R. Hernandez and M. Bathe, *Nat. Commun.*, 2022, **13**, 4935.

200 N. Chauhan, Y. Xiong, S. Ren, A. Dwivedy, N. Magazine, L. Zhou, X. Jin, T. Zhang, B. T. Cunningham, S. Yao, W. Huang and X. Wang, *J. Am. Chem. Soc.*, 2023, **145**, 20214–20228.

201 X. Hu, G. Ke, L. Liu, X. Fu, G. Kong, M. Xiong, M. Chen and X.-B. Zhang, *Anal. Chem.*, 2019, **91**, 11374–11379.

202 M. Mao, Z. Lin, L. Chen, Z. Zou, J. Zhang, Q. Dou, J. Wu, J. Chen, M. Wu, L. Niu, C. Fan and Y. Zhang, *J. Am. Chem. Soc.*, 2023, **145**, 5447–5455.

203 X. Hu, H. Chi, X. Fu, J. Chen, L. Dong, S. Jiang, Y. Li, J. Chen, M. Cheng, Q. Min, Y. Tian and P. Zhang, *J. Am. Chem. Soc.*, 2024, **146**, 2514–2523.

204 T. G. W. Edwardson, K. L. Lau, D. Bousmail, C. J. Serpell and H. F. Sleiman, *Nat. Chem.*, 2016, **8**, 162–170.

205 N. Xie, S. Liu, H. Fang, Y. Yang, K. Quan, J. Li, X. Yang, K. Wang and J. Huang, *ACS Nano*, 2019, **13**, 4174–4182.

206 R. Niu, C. Song, F. Gao, W. Fang, X. Jiang, S. Ren, D. Zhu, S. Su, J. Chao, S. Chen, C. Fan and L. Wang, *Angew. Chem., Int. Ed.*, 2021, **60**, 11695–11701.

207 M. Senoner and W. E. S. Unger, *J. Anal. At. Spectrom.*, 2012, **27**, 1050–1068.

208 Y.-P. Kim, H. K. Shon, S. K. Shin and T. G. Lee, *Mass Spectrom. Rev.*, 2015, **34**, 237–247.

209 K. Gajos, K. Szafraniec, P. Petrou and A. Budkowski, *Appl. Surf. Sci.*, 2020, **518**, 146269.

210 K. Gajos, P. Petrou and A. Budkowski, *Molecules*, 2022, **27**, 3672.

211 K. Gajos, K. Sanocka, M. Wytrwał, P. Dąbczyński and A. Budkowski, *Appl. Surf. Sci.*, 2024, **656**, 159644.

212 R. Riera, E. Archontakis, G. Cremers, T. de Greef, P. Zijlstra and L. Albertazzi, *ACS Sens.*, 2023, **8**, 80–93.

213 M. M. E. Tholen, B. J. H. M. Rosier, R. T. Vermathen, C. A. N. Sewnath, C. Storm, L. Woythe, C. Izquierdo-Lozano, R. Riera, M. van Egmond, M. Merkx and L. Albertazzi, *ACS Nano*, 2023, **17**, 11665–11678.

214 H. Son, J. Park, I. Hwang, Y. Jung, S. Bae and S. Lee, *Proc. Natl. Acad. Sci. U. S. A.*, 2021, **118**, e2113747118.

215 J. Guo, X. Qiu, C. Mingoes, J. R. Deschamps, K. Susumu, I. L. Medintz and N. Hildebrandt, *ACS Nano*, 2019, **13**, 505–514.

216 C. Léger, A. Yahia-Ammar, K. Susumu, I. L. Medintz, A. Urvoas, M. Valerio-Lepiniec, P. Minard and N. Hildebrandt, *ACS Nano*, 2020, **14**, 5956–5967.

217 J. Guo, Y. Chen, Y. Jiang and H. Ju, *Chem. – Eur. J.*, 2017, **23**, 9332–9337.

218 K. Tapio, D. Shao, S. Auer, J. Tuppurainen, M. Ahlskog, V. P. Hytönen and J. J. Toppari, *Nanoscale*, 2018, **10**, 19297–19309.

219 C. H. Olk, J. Heremans, P. S. Lee, D. Dziedzic and N. E. Sargent, *J. Vac. Sci. Technol., B*, 1991, **9**, 1268–1271.

220 D. A. Yarotski, S. V. Kilina, A. A. Talin, S. Tretiak, O. V. Prezhdo, A. V. Balatsky and A. J. Taylor, *Nano Lett.*, 2009, **9**, 12–17.

221 J. Hu, M. Gao, Z. Wang, Y. Chen, Z. Song and H. Xu, *Appl. Nanosci.*, 2021, **11**, 293–300.

222 O. Ouerghi, A. Touhami, A. Othmane, H. Ben Ouada, C. Martelet, C. Fretigny and N. Jaffrezic-Renault, *Sens. Actuators, B*, 2002, **84**, 167–175.

223 G. R. Heath and S. Scheuring, *Nat. Commun.*, 2018, **9**, 4983.

224 P. Zhang, X. Liu, P. Liu, F. Wang, H. Ariyama, T. Ando, J. Lin, L. Wang, J. Hu and B. Li, *Nat. Commun.*, 2020, **11**, 1–9.

225 H. S. N. Jayawardena, S. H. Liyanage, K. Rathnayake, U. Patel and M. Yan, *Anal. Chem.*, 2021, **93**, 1889–1911.

226 A. Rodríguez-Galván and F. F. Contreras-Torres, *Nanomaterials*, 2022, **12**, 3013.

227 H. Yu, X. Xu, P. Liang, K. Y. Loh, B. Guntupalli, D. Roncancio and Y. Xiao, *Bioconjugate Chem.*, 2017, **28**, 933–943.

228 B. Liu and J. Liu, *Anal. Methods*, 2017, **9**, 2633–2643.

229 S. J. Hurst, A. K. R. Lytton-Jean and C. A. Mirkin, *Anal. Chem.*, 2006, **78**, 8313–8318.

230 Y. Zu and Z. Gao, *Anal. Chem.*, 2009, **81**, 8523–8528.

231 D. Bouzas-Ramos, J. I. García-Alonso, J. M. Costa-Fernández and J. Ruiz Encinar, *Anal. Chem.*, 2019, **91**, 3567–3574.

232 Q. Wei, T. Becherer, S. Angioletti-Uberti, J. Dzubiella, C. Wischke, A. T. Neffe, A. Lendlein, M. Ballauff and R. Haag, *Angew. Chem., Int. Ed.*, 2014, **53**, 8004–8031.

233 R. Oliverio, B. Liberelle, F. Murschel, A. Garcia-Ac, X. Banquy and G. De Crescenzo, *ACS Appl. Nano Mater.*, 2020, **3**, 10497–10507.

234 B. L. Baldock and J. E. Hutchison, *Anal. Chem.*, 2016, **88**, 12072–12080.

235 R. Kozlowski, A. Ragupathi and R. B. Dyer, *Bioconjugate Chem.*, 2018, **29**, 2691–2700.

236 M. J. Eller, K. Chandra, E. E. Coughlin, T. W. Odom and E. A. Schweikert, *Anal. Chem.*, 2019, **91**, 5566–5572.

237 M. Horáček, D. J. Engels and P. Zijlstra, *Nanoscale*, 2020, **12**, 4128–4136.

238 P. Delcanale, B. Miret-Ontiveros, M. Arista-Romero, S. Pujals and L. Albertazzi, *ACS Nano*, 2018, **12**, 7629–7637.

239 Q. Ong, Z. Luo and F. Stellacci, *Acc. Chem. Res.*, 2017, **50**, 1911–1919.

240 Y. Randika Perera, R. A. Hill and N. C. Fitzkee, *Isr. J. Chem.*, 2019, **59**, 962–979.

241 Y. Wang, P. E. D. Soto Rodriguez, L. Woythe, S. Sánchez, J. Samitier, P. Zijlstra and L. Albertazzi, *ACS Appl. Mater. Interfaces*, 2022, **14**, 37345–37355.

242 L. Cerofolini, E. Ravera, C. Fischer, A. Trovato, F. Sacco, W. Palinsky, G. Angiuoni, M. Fragai and F. Baroni, *Anal. Chem.*, 2023, **95**, 9199–9206.

243 L. Poppe, J. B. Jordan, K. Lawson, M. Jerums, I. Apostol and P. D. Schnier, *Anal. Chem.*, 2013, **85**, 9623–9629.

244 M. Wang, C. Fu, X. Liu, Z. Lin, N. Yang and S. Yu, *Nanoscale*, 2015, **7**, 15191–15196.

245 M. Maddahfar, S. Wen, S. M. Hosseinpour Mashkani, L. Zhang, O. Shimoni, M. Stenzel, J. Zhou, B. Fazekas de St Groth and D. Jin, *Bioconjugate Chem.*, 2021, **32**, 1146–1155.

246 A. Derenne, K.-M. Derfoufi, B. Cowper, C. Delporte and E. Goormaghtigh, *Anal. Chim. Acta*, 2020, **1112**, 62–71.

247 U. Böcker, S. G. Wubshet, D. Lindberg and N. K. Afseth, *Analyst*, 2017, **142**, 2812–2818.

248 F. Faghihzadeh, N. M. Anaya, L. A. Schifman and V. Oyanedel-Craver, *Nanotechnol. Environ. Eng.*, 2016, **1**, 1.

249 L.-J. Chen, S. S. Shah, J. Silangcruz, M. J. Eller, S. V. Verkhoturov, A. Revzin and E. A. Schweikert, *Int. J. Mass Spectrom.*, 2011, **303**, 97–102.

250 K. Gajos, O. Lishchynskyi, P. Dąbczyński, S. Tymetska, Ł. Bodek, Y. Shymborska, N. Janiszewska, Y. Stetsyshyn and A. Budkowski, *ACS Appl. Mater. Interfaces*, 2026, **18**, 3122–3139.

251 W. S. Tan, A. M. de Jong and M. W. J. Prins, *Langmuir*, 2025, **41**, 22181–22192.

252 Y. Zhai, J. S. DuChene, Y.-C. Wang, J. Qiu, A. C. Johnston-Peck, B. You, W. Guo, B. DiCiaccio, K. Qian, E. W. Zhao, F. Ooi, D. Hu, D. Su, E. A. Stach, Z. Zhu and W. D. Wei, *Nat. Mater.*, 2016, **15**, 889–895.

253 W. S. Tan, A. M. de Jong and M. W. J. Prins, *ACS Appl. Mater. Interfaces*, 2024, **16**, 58191–58202.

254 D. S. Verkhoturov, M. J. Eller, Y. D. Han, B. Crulhas, S. V. Verkhoturov, A. Revzin and E. A. Schweikert, *Langmuir*, 2022, **38**, 5626–5632.

255 B. L. Gorman and M. L. Kraft, *Anal. Chem.*, 2020, **92**, 1645–1652.

256 Y. Jiang, D. Salley, A. Sharma, G. Keenan, M. Mullin and L. Cronin, *Sci. Adv.*, 2022, **8**, eabo2626.

257 C. Li, L. Ma, Z. Xue, X. Li, S. Zhu and T. Wang, *Adv. Sci.*, 2025, **12**, 2501000.

258 N. Shirokii, Y. Din, I. Petrov, Y. Seregin, S. Sirotenko, J. Razlivina, N. Serov and V. Vinogradov, *Small*, 2023, **19**, 2207106.

259 Z. Meng and K. Xia, *Sci. Adv.*, 2021, **7**, eabc5329.

260 N. Serov and V. Vinogradov, *Adv. Drug Delivery Rev.*, 2022, **184**, 114194.

261 F. Cui, Y. Yue, Y. Zhang, Z. Zhang and H. S. Zhou, *ACS Sens.*, 2020, **5**, 3346–3364.

262 M. Bhaiyya, D. Panigrahi, P. Rewatkar and H. Haick, *ACS Sens.*, 2024, **9**, 4495–4519.

263 S. Han, J. Yea, S. Song, S. Lee, J.-W. Choi, Y. K. Lee, J. Park and K.-I. Jang, *Device*, 2026, **4**, 101017.

264 T. Akkaş, M. Reshadsedghi, M. Şen, V. Kılıç and N. Horzum, *Adv. Mater.*, 2025, **37**, 2504796.

265 J. Huzar, R. Coreas, M. P. Landry and G. Tikhomirov, *ACS Nano*, 2025, **19**, 4333–4345.

266 K. T. Butler, D. W. Davies, H. Cartwright, O. Isayev and A. Walsh, *Nature*, 2018, **559**, 547–555.

267 E. Wyrzykowska, A. Mikolajczyk, I. Lynch, N. Jeliazkova, N. Kochev, H. Sarimveis, P. Doganis, P. Karatzas, A. Afantitis, G. Melagraki, A. Serra, D. Greco, J. Subbotina, V. Lobaskin, M. A. Bañares, E. Valsami-Jones, K. Jagiello and T. Puzyn, *Nat. Nanotechnol.*, 2022, **17**, 924–932.

268 A. K. Chew, J. A. Pedersen and R. C. Van Lehn, *ACS Nano*, 2022, **16**, 6282–6292.

269 Y. Duan, R. Coreas, Y. Liu, D. Bitounis, Z. Zhang, D. Parviz, M. Strano, P. Demokritou and W. Zhong, *NanoImpact*, 2020, **17**, 100207.

270 D. P. Russo, X. Yan, S. Shende, H. Huang, B. Yan and H. Zhu, *Anal. Chem.*, 2020, **92**, 13971–13979.

271 X. Yan, A. Sedykh, W. Wang, B. Yan and H. Zhu, *Nat. Commun.*, 2020, **11**, 2519.

272 X. Yan, T. Yue, D. A. Winkler, Y. Yin, H. Zhu, G. Jiang and B. Yan, *Chem. Rev.*, 2023, **123**, 8575–8637.

273 Y. Rong, A. V. Padron, K. J. Hagerty, N. Nelson, S. Chi, N. O. Keyhani, J. Katz, S. P. A. Datta, C. Gomes and E. S. McLamore, *Analyst*, 2018, **143**, 2066–2075.

274 H. Chen, H. Liu, L. Xing, D. Fan, N. Chen, P. Ma and X. Zhang, *ACS Sens.*, 2025, **10**, 2872–2882.

275 A. Bocan, R. Siavash Moakhar, C. del Real Mata, M. Petkun, T. De Iure-Grimmel, S. G. Yedire, H. Shieh, A. Khorrami Jahromi, S. S. Mahshid and S. Mahshid, *Adv. Mater.*, 2025, **37**, 2417520.

276 T. Wang, D. P. Russo, P. Demokritou, X. Jia, H. Huang, X. Yang and H. Zhu, *Nano Lett.*, 2024, **24**, 10228–10236.

277 F. Zivic, A. K. Malisic, N. Grujovic, B. Stojanovic and M. Ivanovic, *Mater. Today Commun.*, 2025, **48**, 113525.

278 J. Ackermann, J. T. Metternich, S. Herbertz and S. Kruss, *Angew. Chem. Int. Ed.*, 2022, **61**, e202112372.

279 Y. Yang, M. Zheng and A. Jagota, *npj Comput. Mater.*, 2019, **5**, 3.

280 P. Kelich, S. Jeong, N. Navarro, J. Adams, X. Sun, H. Zhao, M. P. Landry and L. Vuković, *ACS Nano*, 2022, **16**, 736–745.

281 P. Kelich, J. Adams, S. Jeong, N. Navarro, M. P. Landry and L. Vuković, *J. Chem. Inf. Model.*, 2024, **64**, 3992–4001.

282 M. Kim, C. Chen, P. Wang, J. J. Mulvey, Y. Yang, C. Wun, M. Antman-Passig, H.-B. Luo, S. Cho, K. Long-Roche, L. V. Ramanathan, A. Jagota, M. Zheng, Y. Wang and D. A. Heller, *Nat. Biomed. Eng.*, 2022, **6**, 267–275.

283 A. T. Krasley, S. Chakraborty, L. Vuković and A. G. Beyene, *ACS Nano*, 2025, **19**, 7804–7820.

284 S. Chakraborty, A. T. Krasley, C. H. Smith, A. G. Beyene and L. Vuković, *Nano Lett.*, 2026, **26**, 787–794.

285 C. Tian, S. Lee, S. Park, Y. Cho, C. Baek and S.-Y. Cho, *ACS Nano*, 2025, **19**, 23992–24004.

286 S. Ranallo, A. Amodio, A. Idili, A. Porchetta and F. Ricci, *Chem. Sci.*, 2016, **7**, 66–71.

287 D. Roy and J. W. Park, *J. Mater. Chem. B*, 2015, **3**, 5135–5149.

288 J. J. Gooding, *ACS Sens.*, 2023, **8**, 1–2.

289 K. E. Sapsford, K. M. Tyner, B. J. Dair, J. R. Deschamps and I. L. Medintz, *Anal. Chem.*, 2011, **83**, 4453–4488.

290 S. Buckhout-White, M. Ancona, E. Oh, J. R. Deschamps, M. H. Stewart, J. B. Blanco-Canosa, P. E. Dawson, E. R. Goldman and I. L. Medintz, *ACS Nano*, 2012, **6**, 1026–1043.

291 S. Mourdikoudis, R. M. Pallares and N. T. K. Thanh, *Nanoscale*, 2018, **10**, 12871–12934.

292 P. Zhang, G. Ma, W. Dong, Z. Wan, S. Wang and N. Tao, *Nat. Methods*, 2020, **17**, 1010–1017.

293 S. Naudi-Fabra, M. Tengo, M. R. Jensen, M. Blackledge and S. Milles, *J. Am. Chem. Soc.*, 2021, **143**, 20109–20121.

294 G.-N. W. Gomes, M. Krzeminski, A. Namini, E. W. Martin, T. Mittag, T. Head-Gordon, J. D. Forman-Kay and C. C. Gradinaru, *J. Am. Chem. Soc.*, 2020, **142**, 15697–15710.

295 S. Dhiman, T. Andrian, B. S. Gonzalez, M. M. E. Tholen, Y. Wang and L. Albertazzi, *Chem. Sci.*, 2022, **13**, 2152–2166.

296 X. Xu, L. Wang, Y. Huang, W. Gao, K. Li and W. Jiang, *Anal. Chem.*, 2016, **88**, 9885–9889.

297 X. Sun, L. Riccardi, F. De Biasi, F. Rastrelli, M. De Vivo and F. Mancin, *Angew. Chem., Int. Ed.*, 2019, **58**, 7702–7707.